A Coupled Map Lattice Mimicking Turbulent Puffs and Slugs

Diplomarbeit
vorgelegt von

Christian Marschler

aus

Hildesheim

angefertigt
am Max-Planck-Institut für Dynamik und Selbsorganisation
und der Georg-August-Universität zu Göttingen
2010

Essentially, all models are wrong, but some are useful.

George E. P. Box [48]

The internal motion of water assumes one or other of two broadly distinguishable forms - either the elements of the fluid follow one another along lines of motion which lead in the most direct manner to their destination, or they eddy about in sinuous paths the most indirect possible.

Osborne Reynolds [39]

Preface

Turbulence phenomena and non-linear dynamical systems are two important fields in physics and mathematics. Both have been studied intensely in the last and actual century. Each topic has a long history for itself. Although both fields are well-developed, the overlap between them is relatively small.

On the one hand, turbulence is typically studied in physics, while non-linear dynamical systems are a domain of mathematicians, on the other hand. The last two decades have shown, that it is very useful to study both topics. Turbulent behaviour can be respresented as a problem of non-linear dynamical systems. A huge amount of tools can therefore be used to analyse turbulent behaviour. Additionally, experiments on turbulent pipes can be used to visualise new aspects of dynamical systems. These results can be used by theoreticians to develop new theories in the dynamical systems framework.

This thesis will deal with the interactions between fluid dynamics and non-linear dynamical systems. Notions from fluid dynamics will be explained from a dynamical systems point of view. We will see, that very interesting results can be obtained, when taking a model into account, which is influenced by results from both 'worlds'. This thesis is an access into both fields and builds a bridge between fluid dynamics and non-linear dynamical systems theory.

The whole work would have not been possible without the support of several people. First of all, I would like to thank my supervisor at the Max-Planck-Institute for Dynamics and Self-Organisation, Prof. Dr. Jürgen Vollmer. Jürgen has always supported me with interesting discussions and useful advices. This thesis would have not been possible in this form without him.

Additionally, I would like to thank Prof. Dr. Kree for supervising my work officially at the University of Göttingen.

Special thanks go to my departement, the 'Dynamics of Complex Fluids' and our 'Principles of Self-Organisation' working group. In particular, I would like to thank Jürgen Vollmer, Jan-Hendrik Trösemeier and Artur Wachtel (t.b.c) for reading the final version of this thesis. Thank you for your advice!

Further, I would like to thank the group of Björn Hof for showing me their experiments and simulations on turbulent pipe flow. This gave me a very good insight in the experimental setups.

Last, but not least, I would like to thank all the people on diverse conferences for discussing my posters with me. They gave me many impulses about further aspects of my models. Special thanks go to A. Politi, A. Pikovsky, T. Tél and F. Ginelli.

Contents

Chapter 1

Introduction

Turbulence is encountered everywhere in every day life. Examples reach from vortices behind a starting aircraft, over the aerodynamics of cars to water pouring into a bathtub. A flowing fluid is described by the NAVIER-STOKES equations (1.1.6). In contrast to smooth and time-independent solutions of these equations, which are called laminar flow, turbulent flow refers to a time-dependent, non-ordered flow. Turbulent fluid is in a highly dissipative state. A reduction of turbulence in pipelines can therefore save much energy during oil or gas transport. For this reason, the investigation of turbulence phenomena is not only a challenge to fundamental research but also very important in many applications.

This thesis deals with the special case of turbulent pipe flow. For moderate flow speed it exhibits localised turbulent regions, i.e. 'puffs', that travel down the pipe with constant velocity and are believed to decay eventually. For higher flow rates, there is a transition to 'slugs', where the front of the turbulent region propagates faster than the back side, such that the size of the turbulent region is growing linearly in time.

We will focus on some key questions:

- Which mechanisms can lead to finite-size turbulent puffs ?
- What determines their lifetime?
- What can cause a transition from puffs to slugs?

1.1 Historical Review

Although there still is a sizable and very active research community working on the transition to turbulence in pipe flow, the problem how a pipe becomes turbulent is over a hundred years old. The first study goes back to OSBORNE REYNOLDS in 1883 (cf. figure 1.1 and [39]).

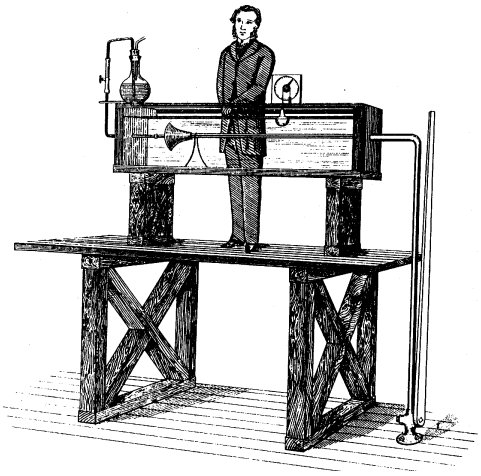

Figure 1.1: Reynolds' experiment in 1883. Reprinted from [1].

Reynolds injected a coloured thread into a pipe. The ink travels along a straight line for small flow velocities (cf. figure 1.2, a))

The thread becomes unsteady for higher velocities (cf. figure 1.2, b)) and eventually splits completely into eddies for even higher velocities (cf. figure 1.2, c) and d)). But this is not the most striking discovery. It is the result, that the flow only depends on *one* dimensionless parameter. This parameter depends on the average flow velocity U, the diameter of the pipe D and the kinematic viscosity ν of the fluid. The number is now called the Reynolds number Re to honor its discoverer. It is defined as

$$\mathrm{Re} = \frac{U \cdot D}{\nu} \tag{1.1.1}$$

Reynolds studied the question, if there is a critical value Re_c, above which the laminar state is unstable. This behaviour is well-known from RAYLEIGH-BÉNARD convection [38] or TAYLOR-COUETTE flow [43, 44], where the steady state becomes unstable above a critical Rayleigh $\mathcal{R}$ or Taylor number $\mathcal{T}$, respectively.

Reynolds observed, that flow of a 'normal' pipe becomes unstable above $\mathrm{Re} \approx 2000$. Turbulence is the only observable state then. But he also used much smoother pipes and less-perturbed initial conditions. In those experiments, the laminar flow could be preserved for $\mathrm{Re} \approx 13000$. Therefore, it is widely accepted now [30, 34], that laminar flow is linearly stable for all Re. There is no critical Reynolds number.

This has been observed for the first time by Reynolds. The transition mechanism to turbulence in pipe flow is still an open question, because linear stability theory fails to describe the transition. The importance of the Reynolds number is also obvious in the equations of motion.

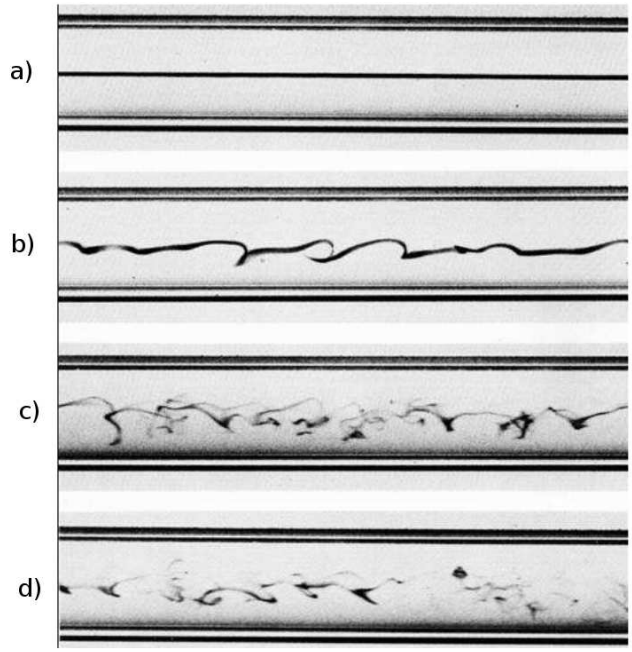

Figure 1.2: Top to Bottom: A laminar flow is stable for small Reynolds numbers. It begins to wiggle, if the Reynolds number is increased. For higher Reynolds numbers above a critical threshold, the flow becomes turbulent. Reproduced from [46].

Although, the flow fields can be very complicated for different geometries, the describing equations are well-known since the investigation of NAVIER and STOKES. By applying the momentum conservation for fluids, one finds the Navier-Stokes equations [1]

$$\rho(\partial_t \vec{u} + (\vec{u} \cdot \nabla)\, \vec{u}) = -\nabla p + \rho\nu\nabla^2 \vec{u} + \vec{f} \tag{1.1.2}$$

Here, ρ and ν are the density and kinematic viscosity of the fluid, respectively. $\vec{u}(\vec{r}, t)$ is the flow field at each space $\vec{r}$ and time t, p is the pressure and $\vec{f}$ is an external body force. This equation is a partial differential equation of second order. Additionally, it is non-linear, because of the convective term $(\vec{u} \cdot \nabla)\, \vec{u}$. This makes the solution of the equation extremely complicated. A closer look reveals, that these equations are three differential equations for the four unknowns $\vec{u}$ and p. In order to complete the system, a fourth equation, the continuity equation for the mass density, is needed,

$$\partial_t \rho + \nabla\, (\rho \vec{u}) = 0 \tag{1.1.3}$$

Assuming incompressibility, the density ρ does not depend on time or space. As a consequence, the continuity equation reduces to

$$\nabla \cdot \vec{u} = 0 \tag{1.1.4}$$

The Navier-Stokes equations can be formulated in a dimensionless way by applying the transformations

$$\vec{r}' = \frac{\vec{r}}{L}, \qquad t' = \frac{L}{U} t, \qquad \vec{u}' = \frac{\vec{u}}{U}, \qquad p' = \frac{L}{U^2} \frac{p}{\rho} \tag{1.1.5}$$

where L and U are a characteristic length scale and velocity of the system, respectively. This leads to the dimensionless Navier-Stokes equations

$$\partial_t \vec{u} + \vec{u} \cdot \nabla \vec{u} = -\nabla p + \mathrm{Re}^{-1} \nabla^2 \vec{u} \tag{1.1.6a}$$

$$\nabla \cdot \vec{u} = 0 \tag{1.1.6b}$$

The external force and the additional primes have been dropped for simplicity. The only free parameter of the dimensionless Navier-Stokes equatuion[1] is the Reynolds number Re.

We used the no-slip boundary condition

$$\vec{u}(r = R, t) = 0 \tag{1.1.7}$$

This states, that the fluid sticks to the pipe walls.

For pipe flow, the stationary solution can be calculated analytically. By using cylindrical coordinates (r, ϕ, z) with the z axis along the pipe, one obtains

$$\vec{u}(r, \phi, z) = -\frac{\partial_z p}{4} \mathrm{Re}(1 - r^2) \vec{e}_z \tag{1.1.8}$$

where $\partial_z p$ is the pressure gradient along the pipe, which is assumed to be constant.

1.2 Recent Progress

The motivation of our considerations are experimental studies on turbulent puffs in pipe flow by Hof et al. [16, 17]

The structures are called convective instabilities, since they are taken away from their point of origin by the flow without growing. The transition to turbulence can not be described by linear stability theory, since the laminar state is linearly stable for all Re. Therefore, one needs a finite perturbation to the laminar state to trigger a turbulent puff.

Hof et al. triggered a puff by injecting water into the laminar flow at some point of the pipe. Resulting puffs travel through the pipe and reach its end after some time, unless they decay on the way. The survival probabilities are shown in figure (1.3).

As expected, the survival probality is zero for very low Reynolds numbers (laminar limit, where the lifetime of puffs is small) and tends to one in the turbulent limit. Measurements has been done for several pipe lengths L. Longer pipes show a smaller survival probability: due to the constant velocity of a puff for fixed Re, it has had more time to decay in longer pipes and less puffs reach the end.

The next step is to determine the lifetime distribution of turbulent puffs. The Reynolds number is kept fixed and the survival probability of a puff is measured for several pipe lengths. The survival probability for a fixed length can then be related by the puff

[1] A general solution for the Navier-Stokes equations is not known up to now.Therefore, it is one of the most complicated problems in classical mechanics. The proof of existence and smoothness of solutions is a Clay Millenium prize problem [20].

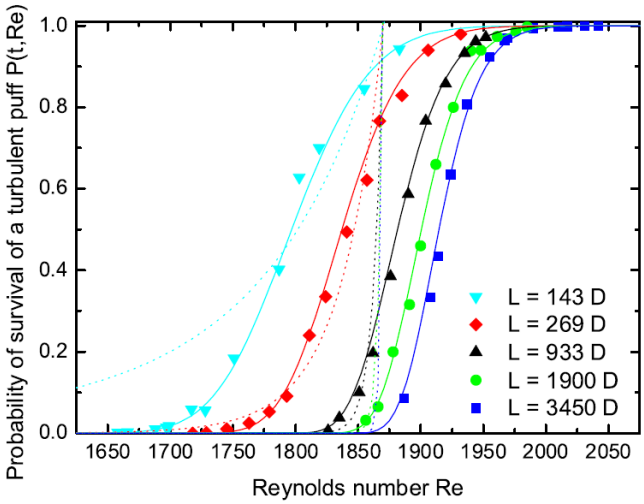

Figure 1.3: Experimental survival probabilities for different pipes and Reynolds numbers. L is the distance to the end of the pipe, measured in multiples of its diameter D. Reprinted from [16].

velocity to a survival probability for a fixed time. Measurements have been done for a range of Re and the average lifetime $\tau(\mathrm{Re})$ has been computed. Early work [50] for $1550 \leq \mathrm{Re} \leq 1850$ suggested a linear decrease of τ^{-1} with a transition to infinite lifetimes at $\mathrm{Re} \approx 1870$ (dashed line in figure 1.4, a)) In contrast, numerical and experimental studies [18] for a range $1750 \leq \mathrm{Re} \leq 1950$ obtained

$$\tau \sim \exp(c_1 \mathrm{Re}), \qquad c_1 \in \mathbb{R} \tag{1.2.1}$$

which is the solid black line in 1.4, a). This data suggested, that τ remains finite for all Re. The most recent high precision data [16] for $1550 \leq \mathrm{Re} \leq 2050$ resolve the difference of the previous studies and further underpin the view, that τ remains finite.

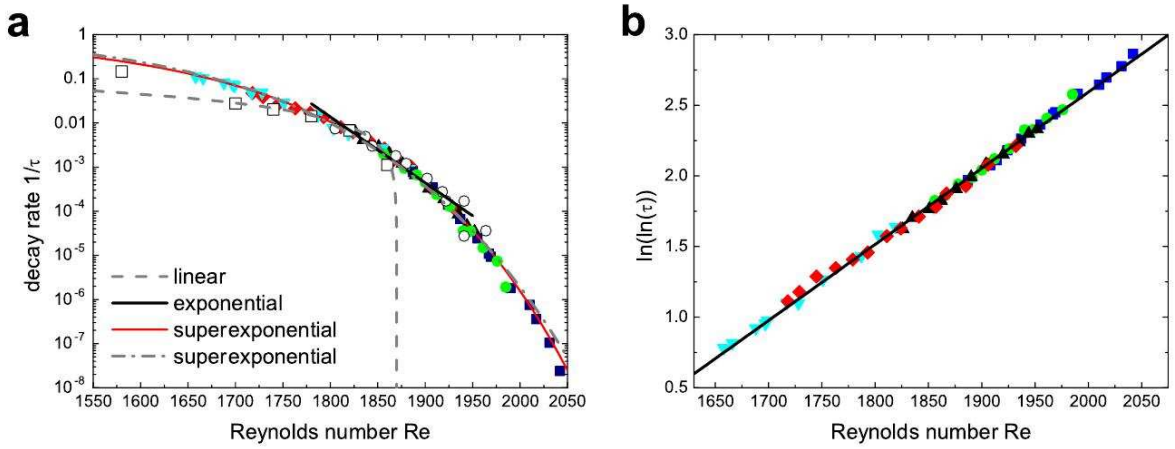

Figure 1.4: a) τ^{-1} as a function of Reynolds number. b) A log-log normal plot shows a superexponential scaling law. Reprint from [16].

However, they suggest a super-exponential increase of τ like

$$\tau \sim \exp(\exp(c_2 \mathrm{Re})), \qquad c_2 \in \mathbb{R} \tag{1.2.2}$$

This expected scaling law is supported by figure 1.4, b)

The data shown in figure 1.4 has setteled the dispute on qualitative features of τ. But the exact form is not quite clear. An alternative fit

$$\tau \sim \exp(c_3 \mathrm{Re}^n), \qquad c_3, n \in \mathbb{R} \tag{1.2.3}$$

can describe the data, too (cf. [16]). These scaling laws are called super-exponential. A transient which has such a lifetime scaling law is therefore called super-long transient, in contrast to long transients, which obey a power-law scaling.

However, there is no hope for more data. It is hard to improve the experimental results, because many problems have to be solved. The very rapid lifetime increase of a turbulent puff for $\mathrm{Re} > 2000$ is one problem. Therefore, one needs very long pipes to determine the lifetime distribution correctly. This is very hard to do, since the pipes would easily exceed the dimensions of the lab. Another problem is the experimental setup. The pipes has to be very smooth. Otherwise one would get wrong lifetimes due to the roughness of the pipe, which acts as an additional perturbation [11, 28]. In addition, there are several problems which has a minor effect, but are still essential, e.g. keeping a constant temperature along the whole pipe or a laminar injection at the beginning of the pipe.

A different method is a computer simulation. This has the advantage, that one can specify the state of the system very well. Without the inaccuracy of perturbations in real experiment, i.e. rough pipe walls, theoretical assumptions can be checked. Almost all simulations on pipe turbulence are based on the Navier-Stokes equations. This is a common point to start, since the Navier-Stokes equations are the equations of motion for fluid dynamics. The time-dependent Navier-Stokes equations can not be solved analytically, because they are non-linear partial differential equations(pde). Computer simulations are also very hard to carry out. One problem is to find a reasonable discretization of space and time. The simulation results are getting better for a finer discretization grid, but at the cost of a long simulation time. Several methods have been introduced to tackle this problem. One way is to do a mode expansion of the solutions [29,31]. For appropriate modes (Fourier and Chebyshev polynomials), one is able to carry out simulations rather fast and get noticable results, which can be compared to experimental data.

Another transition can be observed for even higher Reynolds numbers. Due to the super-long lifetime scaling law, the average lifetime increases very fast with Re. For quite high $\mathrm{Re} \approx 2500$, a new state, known as a turbulent slug, is observed. A slug is an absolute instability. In contrast to a puff, its front velocity is much larger than its back. Therefore, a slug grows while travelling through the pipe and eventually fills it completely. The lifetime of turbulent slugs is expected to be infinite. This assumption has not been checked. A direct measurement in experiments is not accesible, since the lifetime is quite too long, due to the super-exponential scaling law. Since the lifetime of slugs is expected to be infinite, the growth speed is a better quantity to determine a puff-to-slug transition. A critical Re_{cr} for the puff-slug transition can be found experimentally

and is currently under investigation. The correct value Re_{cr} for the slug transition is an open question. Therefore, further studies on the growth speed dependence on Re are needed.

Although, there has been many experiments and numerical simulations, the underlying mechanism for the transitions is not known. Therefore, a good theory is needed to guide experiments and simulations.

1.3 Scope of this work

Our aim is to understand the transition from laminar to turbulent flow in a general setting. We will use pipe flow as a stereotype for transition scenarios. But we will not use the Navier-Stokes equations to simulate pipe flow. Rather we go a different way and study low-dimensional models that share some aspects of pipe flow. Therefore, our results can not directly be applied to real systems. Instead, we can focus on the underlying principles leading to a transition from laminar to turbulent motion. This is useful, since even *possible* mechanisms are unclear. We provide candidates for scenarios to check.

The next chapter will briefly review the basic notions from dynamical systems theory needed for our investigations. Chapter 3 will deal with a 2d model system, which is used to describe the behaviour of super-long transients. We will especially emphasize the importance of the lifetime scaling law and compare it to theoretical predictions. The main part of this thesis is presented in chapter 4. A spatially extended model is investigated that mimics turbulent puff and slug behaviour. Therefore, we study a unidirectional coupled map lattice. In particular, we will deal with the distribution and scaling laws for the lifetime and velocity of puffs. The laminr-puff and puff-slug transition will be determined in the model framework. Additionally, the growth speed will be studied for the slug regime. The conclusion in chapter 5 will compare our results to real pipe flow and give an outlook for future work.

Chapter 2

Dynamical Systems Revisited

In order to get an overview about the tools we need for our further work, we will compile some concepts of dynamical systems in this section.

Definition 1. *A dynamical system is defined by an evolution equation*

$$\frac{\mathrm{d}}{\mathrm{d}t}\vec{x} = \vec{F}(\vec{x}) \quad , \tag{2.0.1}$$

where $\vec{x} \in \mathbb{R}^m$ is the state of the system and $\vec{F}$ is the evolution operator (i.e. 'velocity'), which uniquely determines the change of the state with time [33].

Dynamical systems are everywhere around us. The word 'dynamical' lets us think of systems that show some motion. The cause of the motion is given by a force, according to Newton. Examples are very numerous and reach from the movement of a pendulum to shooting a cannon ball. But we can also describe things with dynamical systems, which are not mechanical, like the voltage characteristic while charging a capacitor or the induction voltage of a coil. But the dynamical systems approach is not limited to such simple systems. Even more complex systems and tasks, like weather forecasting, population dynamics of bees, the spreading of epidemics or share prices in stock markets, can be described by dynamical systems. The most important dynamical system we are interested in, is the flow of water through a pipe, which can be described by the Navier-Stokes equations.

Mathematically, a dynamical system can be described by a set of first-order differential equations. The exact definitions will be given in the next section.

2.1 Definitions

Definition 1 looks quite restricted, because not all systems are of first order. The most prominent and probably most important example is Newton's law (here in one dimension for simplicity)

$$\ddot{x} = F(x, \dot{x}) \tag{2.1.1}$$

This is a differential equation of second-order and therefore does not obey the definition of a dynamical system. But we can transform this equation into a system of first-order differential equation by defining the velocity $v := \dot{x}$. This gives us the following system:

$$\dot{x} = v \tag{2.1.2a}$$
$$\dot{v} = F(x, v) \tag{2.1.2b}$$

which can be written in compact form as

$$\frac{\mathrm{d}}{\mathrm{d}t}\vec{u} = \vec{F}(\vec{u}) \qquad \text{where} \quad \vec{u} = (x, v)^T \tag{2.1.3}$$

We have now obtained an equation of the form (2.0.1). This procedure can be generalized to higher dimensions and to differential equations of n-th order. So, our definition of a dynamical system is quite general.

A very simple class of dynamical systems are those with a discrete time. This can be seen in populations, where we can measure the population of our beehive every year at the same date and time.

A possibility to obtain a time-discrete system is the technique of a POINCARÉ section [27]. This technique is very useful to study properties of time-continuous systems. We are only investigating models, which are already time-discrete, so we skip an introduction on the Poincaré section technique.[1]

In time-discrete systems, a state at time n uniquely determines the state at time $n+1$, generally. In this case, the evolution operator is also called the mapping $\vec{M}$ of the dynamical system, and we define

$$\vec{x}_{n+1} = \vec{M}(\vec{x}_n) \tag{2.1.4}$$

where the discrete time is denoted as $n \in \mathbb{N}_0$. An explicit time dependence of $\vec{M}$ is not taken into account in this thesis. Those systems are called *autonomous*. Once $\vec{M}$ is determined, the future of the system can be computed very easily. To get the state after m timesteps, we just need to apply $\vec{M}$ m times.

$$\vec{x}_{n+m} = \underbrace{\vec{M}(\vec{M}(\cdots\vec{M}}_{m \text{ times}}(\vec{x}_n))) \tag{2.1.5}$$

For one-dimensional systems, this iteration can be done by hand, even with very old calculators. To abbreviate this long expression, we define a short version of (2.1.5).

$$\vec{x}_{n+m} := \vec{M}^m(\vec{x}_n) \tag{2.1.6}$$

We have already mentioned above, that a state $\vec{x}_n$ uniquely determines the state $\vec{x}_{n+1}$. All these possible points build the phase space or state space of the system. A point in phase space uniquely determines the state of the system and therefore defines its future.

[1] Time-discrete systems are also very fast to simulate on a computer. Computers can only deal with a discrete time. Therefore, the time for a discretisation step is saved. This step introduces errors, because we can not let the length of the timestep to zero. Following timesteps on a computer differ at least in one bit.

The phase space can have a low dimension, like in the example of a mathematical pendulum, where we only need two coordinates, i.e. space and momentum, to define the state of the system. This leads to a two-dimensional phase space. But the phase space dimension can even be rather high, e.g. when dealing with thermodynamical systems with N particles, where the phase space dimension is $6N$.

We will now come to another important definition, which is used all the time, when working with dynamical system.

Definition 2. *The evolution of the dynamical system for a given initial condition is known as its trajectory or forward orbit T. For a discrete time evolution it is defined as*[2]

$$T := \{\vec{x}_i \mid \vec{x}_i = \vec{M}^i(\vec{x}_0),\ i \in \mathbb{N}_0\} \tag{2.1.7}$$

A trajectory determines the time evolution of an initial value, respecting the dynamics of the system. A trajectory can be a series of measurments in a time discrete case, e.g. the temperature on day i in Göttingen.

Trajectories can be measured even without the knowledge of $\vec{M}$. Therefore, the analysis of sets of trajectories is the basic step when studying dynamical systems. An interesting aspect is, that trajectories can not intersect in phase space. This is understood by keeping in mind, that a point in phase space *uniquely* determines the future of the system. If two trajectories have one point in common, their future evolution has to be identical. This fact is very useful, if one is interested in the structure of the phase space.

Another part of the phase space structure can be analyzed by the determination of invariant subsets. This is picked up in the next section.

2.2 Invariant Subsets

Beside the analysis of typical trajectories, one can investigate, if there are subsets of the phase space, which are not changing during the evolution of the system.

Definition 3. *A subset A of the phase space is called invariant, if the image of A under the mapping $\vec{M}$ is the same subset A:*

$$A = \vec{M}(A) \tag{2.2.1}$$

An example for an invariant subset is easily found. The logistic map is a frequently used example for several aspects of dynamical systems (cf. [6, 33]). It is defined by

$$f(x) = rx(1-x) \qquad r \in \mathbb{R} \tag{2.2.2}$$

A plot of the logistic map for $r = 4$ is given in figure 2.1. For $r = 4$, the interval $I = [0, 1]$ is an invariant subset for the dynamics, since we have $f(I) = I$.

There are a bunch of special invariant subsets. The most simple ones are the fixed points.

[2] If $\vec{M}$ is invertible, the complete orbit is also defined for the past, i.e. $i \in \mathbb{Z}$ [6].

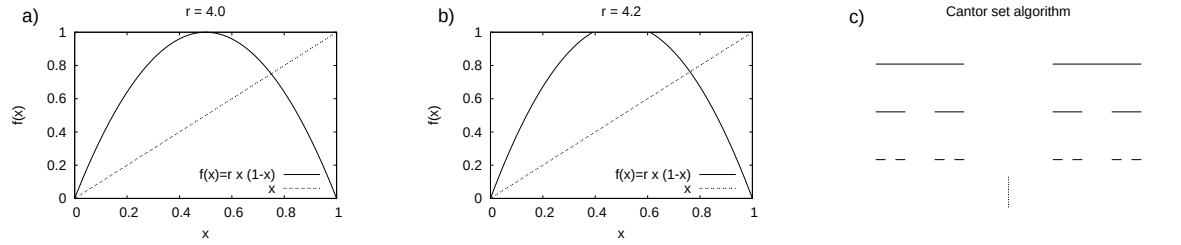

Figure 2.1: a) The logistic map for $r = 4$. $I = [0, 1]$ is an invariant set. b) I is no longer invariant for $r > 4$, since $f(x) > 1$ for $x \in \left[\frac{1}{2} - \delta, \frac{1}{2}\delta\right]$ with $\delta = \sqrt{\frac{r-4}{4r}}$. c) Algorithm to construct the middle third Cantor set.

Definition 4. *A point $\vec{x}^f$ of the phase space, which is invariant under the time evolution of the system, is called a fixed point. It obeys the equation*

$$\vec{x}^f = \vec{M}(\vec{x}^f) \tag{2.2.3}$$

Equation (2.2.3) is therefore called the fixed point equation [33]. Fixed points play an important role in each dynamical system. They are the most simple invariant subsets one can think of and are easily calculated in most cases. Often, it is possible to make interesting statements of the dynamics only by the knowledge of the fixed points.

The next higher level invariant subset is a periodic orbit [33].

Definition 5. *A point $\vec{x}^*$ in phase space lies on a periodic orbit of period $p \in \mathbb{N}$, if*

$$\vec{x}^* = \vec{M}^p(\vec{x}^*) \tag{2.2.4}$$

The trajectory

$$T = \{\vec{x}^*, \vec{M}(\vec{x}^*), \ldots, \vec{M}^p(\vec{x}^*)\} \tag{2.2.5}$$

is called a periodic orbit of period p.

The mapping $\vec{M}^p$ is also known as the p-times iterated map. After p iterations, the periodic orbit has reached the starting point again. Therefore, a periodic orbit is a closed trajectory. The condition (2.2.4) applies to each point on the periodic orbit, such that periodicity is a property of the complete periodic orbit. One can find periodic orbits by searching for fixed points of the p-times iterated map $\vec{M}^p$.

Both fixed points and periodic orbits are invariant subsets of dimension zero, since both sets contain only isolated points. This is different for sets like I in the example of the logistic map above. The interval is an invariant subset of dimension one.

There are more types of invariant subsets. Some of them may even have fractal, i.e. non-integer, dimension. In order to characterise these sets, we first need to introduce a definition for the dimension of a set.

This excursion will introduce the box-counting dimension, also known as the capacity. We will first think of objects, whose dimension we already know. From that point, we can generalize the notion of a dimension.

Let ϵ be a reference length scale. We form boxes of side length ϵ out of it. For a line with length L, we need

$$N_L(\epsilon) = \frac{L}{\epsilon} \tag{2.2.6}$$

boxes (i.e. line segments) to cover the line. The number of boxes $N(\epsilon)$ we need to cover the set is obviously depending on the reference length ϵ. For smaller ϵ we need more boxes. In analogy to that, we need

$$N_A(\epsilon) = \frac{A}{\epsilon^2} \tag{2.2.7}$$

boxes to cover an area of size A with boxes of size ϵ^2. The scaling of N with ϵ is determined by the dimension of the set. Equations (2.2.6) and (2.2.7) can also be written as

$$\ln N_L = \ln L + 1 \cdot \ln\left(\frac{1}{\epsilon}\right) \tag{2.2.8a}$$

$$\ln N_A = \ln A + 2 \cdot \ln\left(\frac{1}{\epsilon}\right) \tag{2.2.8b}$$

For sufficiently small ϵ, the constant offset in those relations may be neglected such that the following definition is useful.

Definition 6. *The box-counting dimension is defined as (cf. [33])*

$$D := \lim_{\epsilon \to 0} \frac{\ln N(\epsilon)}{\ln(1/\epsilon)} \tag{2.2.9}$$

By construction, this definition yields the correct results for the dimension of objects we already know.

On the other hand, a remarkable dimension is found for the Cantor set. We will describe the construction of the Cantor set in brief. A visualisation of this algorithm is given in figure 2.1, panel c. Imagine an interval of length one, i.e. the interval I from our previous example. Delete the middle third from this interval in order to get two stripes of length 1/3. From these stripes, delete the middle third again to get four stripes of length 1/9 and so on. If we do this procedure ad infinitum, we get the Cantor set. We now want to know the dimension if this set. In order to obtain it, we will use the box-counting algorithm. We choose a length scale $\epsilon = \left(\frac{1}{3}\right)^n$, where n defines the iteration step in the Cantor procedure. In order to cover the set, we need $N(\epsilon) = 2^n$ boxes. We now apply the dimension definition to calculate the dimension of the Cantor set.

$$D = \lim_{\epsilon \to 0} \frac{\ln N(\epsilon)}{\ln 1/\epsilon} = \lim_{n \to \infty} \frac{\ln(2^n)}{\ln(3^n)} = \frac{\ln(2)}{\ln(3)} \approx 0.631 \tag{2.2.10}$$

Since the Cantor set has a non-integer dimension it is called fractal (cf. [6]). Fractal structures typically arise in objects with a self-similar structure. Prominent examples are the MANDELBROT set [25] and the KOCH snowflake [26].

We can now come back to our investigation of invariant subsets. Imagine again the logistic map (2.2.2). But now choose $r > 4$, so that I is no longer an invariant subset

(cf. figure 2.1, panel b). In each iteration, there is taken away some mass from I. The amount is related to the width of the hole

$$2\delta = \sqrt{\frac{r-4}{r}} \tag{2.2.11}$$

The points that stay forever in I form a Cantor set I_f. It is noticable, that I_f is not an empty set! Like in the case of the middle third Cantor set, I_f has a fractal dimension between zero and one, depending on the value of r. Since I_f is not empty and points in I_f never leave I_f, it is an invariant subset of the dynamics. Those invariant subsets with fractal dimension are called strange in the terminology of dynamical systems, because of there fractal dimension.

We have now classified all important invariant subsets. But the relevance of an invariant subset depends on another property, too. This is the stabilty against infinitesimal perturbations which will be investigated in the next section.

2.3 Stable/Unstable Directions in Phase Space

The stability of an invariant subset is a very important property. The stability decides, whether a trajectory stays in the vicinity of the invariant subset or if it leaves it. In experiments one typically observes stable invariant subsets, because infinitesimal perturbations drive the trajectory away from the unstable subset [3]. Errors in the experimental setup or the finite length of numbers in a computer simulation are enough to let the trajectory move away from the unstable subset. The exact defintion for one-dimensional systems will be given in the next section. After that, we will generalize the notion to higher dimensions.

2.3.1 One Dimension

First, we will investigate the stability of a fixed point, since fixed points are the most simple invariant subsets. Further we will limit our considerations to one dimensional mappings

$$x_{n+1} = f(x_n) \qquad x_i \in \mathbb{R} \quad \forall\, i \in \mathbb{N} \tag{2.3.1}$$

This procedure is useful to get an intuitive understanding of the notion of stability. The definitions can be generalized to higher dimension very easily in the following section. We can think of f as a simple mapping, e.g. the logistic map in (2.2.2). Note, that the stability can be defined in a general way for arbitrary trajectories. But we will restrain our considerations to the analysis of the stability of invariant subsets, since this is the case we will use most of the time.

Definition 7. *A fixed point x^f is stable, if for every neighbourhood U of x^f there is a neighbourhood $V \subset U$ of x^f such that every trajectory starting in V remains in U for all times. This is also called Lyapunov stability [19].*

[3] Exceptions are flows with self-reproducing agents like in catalytic reactions or algae.

This rather mathematical definition is very intuitive, but hard to apply to model systems. Therefore, we also introduce the notion of linear stability, which can be applied easily.

We assume, that the fixed point x^f is perturbed by an infinitesimal amount δ_n

$$x_n^s = x^f + \delta_n \qquad \delta_n \ll 1 \tag{2.3.2}$$

where δ_n is the perturbation at time n[4]. Now we assume that the time evolution of x_n^s can be calculated for small δ_n with a Taylor expansion of order one around x^f

$$\begin{aligned} x_{n+1}^s &= f(x_n^s) = f(x^f) + f'(x^f)\delta_n + O(\delta_n^2) && (2.3.3)\\ &= x^f + f'(x^f)\delta_n + O(\delta_n^2) && (2.3.4)\end{aligned}$$

By applying the definition of the perturbation, we get the linear evolution of the perturbation as

$$\delta_{n+1} = f'(x^f)\delta_n \tag{2.3.5}$$

The result can now be used to define the linear stability.

Definition 8. *A fixed point x^f is linearly stable, if infinitesimal perturbations decay in their absolute value with time.*

$$\frac{|\delta_{n+1}|}{|\delta_n|} = \left|f'(x^f)\right| < 1 \tag{2.3.6}$$

If $\left|f'(x^f)\right| = 1$, then x^f is metastable. For $\left|f'(x^f)\right| > 1$, the perturbations grow and the fixed point is called unstable [33].

Linear stability ascertains, that small perturbations of stable (unstable)fixed points decay (grow) exponentially. Consequently, for an unstable fixed point the trajectories move away from x^f. On the other hand, in the marginal case $f'(x^f) = 0$ one has to fall back to a more refined notion of stability, like Lyapunov stability, to make mathematical statements.

The same idea can be applied to the analysis of the stability for periodic orbits. We just use the p-times iterated map f^p instead of f and we evaluate it at a periodic point x^p of the periodic orbit instead of at x^f. All other definitions are the same. It is more complicated to analyse the stability for invariant subsets, that contain fractal sets or whole intervals. One needs definitions from the theory of topology, which we will not discuss in this work [5].

Generally, stable invariant subsets are called attractors or sinks. On the other side, unstable sets are called repellers or sources. The most popular attractor is the Lorenz attractor, which rises in the investigation of Rayleigh-Bénard convection. It is classified to be a chaotic attractor. We will briefly discuss the notion of 'chaotic' now.

Definition 9. *An invariant set is called chaotic, if trajectories on the invariant set are aperiodic and have sensitive dependence on initial conditions (cf. [33]). If the set is also a attractor, it is called a chaotic attractor.*

[4] We always assume, that the typical size of the attractor is of order 1. Therefore, $\delta_n \ll 1$ refers to an infinitesimal perturbation.

[5] One way to determine the stability is to use bonds of the Lyapunov spectrum.

The sensitive dependence on initial conditions is determined by the behaviour of neighboured trajectories.

Definition 10. *Let x_0 and $y_0 = x_0 + \delta_0$ be two initial conditions on the attractor, where $\delta_0 \ll 1$ and let $\delta_n := y_n - x_n$. If for almost all initial conditions x_0, y_0 the perturbation δ_0 grows exponentially with time*

$$\frac{|\delta_n|}{|\delta_0|} \sim \exp(\lambda n) \qquad \lambda > 0 \tag{2.3.7}$$

we say that the attractor has sensitive dependence on initial conditions (cf. figure 2.2, [33]).

Note, that the difference δ_n has to be smaller than the typical diameter of the attractor for all n.

This property leads to the unpredictability of trajectories on chaotic attractors. Both in experiments and in simulations[6], we can not define the initial condition with arbitrary precision. These small inaccuracies grow exponentially with time. This fact is known from every days life. Weather forecasts are very precise for the next day. But the forecast turns to guessing, when we would like to know the weather a few weeks in advance. This is due to the fact, that the weather system has sensitive dependence on initial conditions.

We will now discuss the stability of higher dimensional systems. Those systems are more realistic, but we have to do some more analysis.

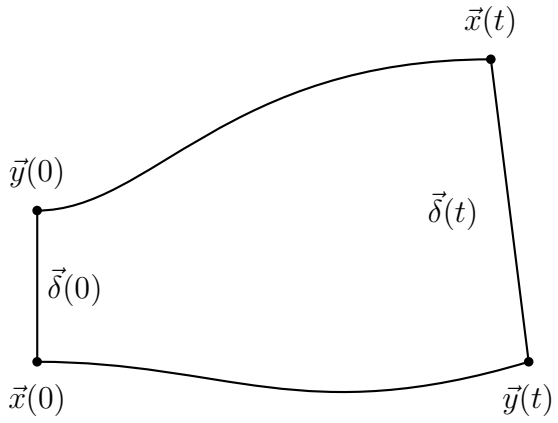

Figure 2.2: For the definition of sensitive dependence on initial conditions.

[6]For some cases, the initial conditions in computer simulations can be determined to an arbitrary precision by using symplectic integrators.

2.3.2 Higher Dimension

The idea behind the linear stability analysis is the same as in the case of one dimensional systems. But we have to interpret the results from a different perspective.

Again, we will do the analysis for fixed points only. The generalisation is the same as in the one dimensional case and will not be discussed.

We will now investigate the stability of a fixed point $\vec{x}^f$ under the system

$$\vec{x}_{n+1} = \vec{M}(\vec{x}_n) \tag{2.3.8}$$

Again, we can express a perturbated trajectory by[7]

$$\vec{x}_n^s = \vec{x}^f + \vec{\delta}_n \qquad \text{with } \left|\vec{\delta}_n\right| \ll 1 \tag{2.3.9}$$

It is worth mentioning, that in this high-dimensional case, the perturbation has a direction. As mentioned below, this is a crucial property of the perturbation with a great impact on the dynamics of the system. The perturbation can be expanded in a Taylor series

$$\begin{aligned} \vec{x}^s_{n+1} = \vec{M}(\vec{x}^f + \vec{\delta}_n) &= \vec{M}(\vec{x}^f) + \mathrm{D}\vec{M}(\vec{x}^f)\cdot\vec{\delta}_n + O(\vec{\delta}_n^2) && (2.3.10)\\ &= \vec{x}^f + \mathrm{D}\vec{M}(\vec{x}^f)\cdot\vec{\delta}_n + O(\vec{\delta}_n^2) && (2.3.11)\end{aligned}$$

where $\mathrm{D}\vec{M}(\vec{x}^f)$ is the Jacobian of $\vec{M}$, evaluated at the fixed point $\vec{x}^f$. For an N-dimensional system it takes the form

$$\mathrm{D}\vec{M} := \begin{pmatrix} \frac{\partial M_1}{\partial x_1} & \cdots & \frac{\partial M_1}{\partial x_N} \\ \vdots & \ddots & \vdots \\ \frac{\partial M_N}{\partial x_1} & \cdots & \frac{\partial M_N}{\partial x_N} \end{pmatrix} \tag{2.3.12}$$

With this expansion, we can determine the evolution of the perturbation $\vec{\delta}_n$ to be

$$\vec{\delta}_{n+1} = \mathrm{D}\vec{M}(\vec{x}^f)\cdot\vec{\delta}_n \tag{2.3.13}$$

The stability of the fixed point is now determined by the eigenvalues λ_i and eigenvectors of $\mathrm{D}\vec{M}(\vec{x}^f)$ (cf. [19]).

Definition 11.

- *if all λ_i have a negative real part, then $\vec{x}^f$ is stable, since every perturbation decays $\left(\left|\vec{\delta}_n\right| \to 0\right)$.*
- *if there is at least one eigenvalue λ_j with positive real part, then $\vec{x}^f$ is unstable, since there is at least one direction $\vec{e}_j$, where a perturbation grows.*
- *if all λ_i have a vanishing real part and it exists a complex-conjugated pair with non-vanishing imaginary part, then the solution oscillates and we have a periodic perturbation, which is not growing*[8]*.*

[7] cf. footnote 4

[8] It is also possible to have only one pair of complex-conjugated λ. If all other eigenvalies have negative real part, then th solution is only oscilating in a plane, while all other directions are stable.

It is clear, that the variety of possible perturbation is much larger than in the one dimensional case.

In higher dimensions, we have a direction, related to the perturbation. It is possible, that a fixed point has only stable directions but one, which is unstable. These points are therefore called saddle, since they have the form of a saddle in the high dimensional phase space. An invariant subset, which has stable as well as unstable directions and shows sensitive dependence on initial conditions is called a chaotic saddle.

The definition of stability leads straight to the concept of Lyapunov exponents.

2.4 Lyapunov Exponents

This section will introduce the concept of Lyapunov exponents and vectors, which are named after the Russian mathematician and physicist Aleksandr Lyapunov. Lyapunov exponents are a widespread technique to characterize stability and chaos. The Lyapunov exponents are the exponents of the exponential growth of perturbations (cf. [33]).

In equation (2.3.6), we have introduced the definition of the stability of a fixed point via the growth of infinitesimal perturbations.

$$\frac{|\delta_{n+1}|}{|\delta_n|} = \left|f'(x^f)\right| < 1 \tag{2.4.1}$$

This gives us the growth in one iteration step. It can be generalized to the growth for m iterations

$$\frac{|\delta_{n+m}|}{|\delta_n|} = \left|f'(x^f)\right|^m = \exp(\lambda m) \qquad \text{where } \lambda := \ln\left(\left|f'(x^f)\right|\right) \tag{2.4.2}$$

The exponent λ is called the Lyapunov exponent and can be defined by

$$\lambda := \lim_{m\to\infty} \lim_{|\delta_n|\to 0} \frac{1}{m} \ln\left(\frac{|\delta_{n+m}|}{|\delta_n|}\right) \tag{2.4.3}$$

$\left|f'(x^f)\right| = \exp(\lambda)$ is often referred to as the Lyapunov number. The Lyapunov exponents can now be used to determine the linear stability of a fixed point

- $\lambda > 0$: unstable
- $\lambda = 0$: marginally stable
- $\lambda < 0$: stable

The advantage of using Lyapunov exponents is given by the fact, that they can be computed very easily. The knowledge of the underlying map f is not neccesary to calculate λ, since it is defined via the growth of perturbations. Another advantage becomes obvious in systems of higher dimension. Here, the Lyapunov exponents are the eigenvalues of the Jacobian, evaluated at the fixed point position. This makes the Lyapunov exponents to an essential tool in the analysis of the stability of invariant subsets.

In the next section we turn to bifurcation theory.

2.5 Bifurcations

A qualitative change of the dynamics of a system while varying a control parameter is known as a bifurcation. Bifurcations are analyzed in the mathematical field of bifurcation theory. We will inspect here only some basic bifurcation scenarios, which are important for the analysis of our model systems.

We will deal with bifurcations of one-dimensional, smooth functions f, which depend smoothly on a control parameter r. There are three generic bifurcation types for this class of functions [6,27,33], which can be found in nearly every one-dimensional dynamical system. They regard the generation of fixed points and the change of stability of fixed points.

2.5.1 Tangent Bifurcation

The first bifurcation type will be introduced by an example. We note, that the fixed points of a one-dimensional map are determined by the intersection points of the map f with the diagonal line $f(x) = x$. We will now study the dynamics of $f(x) = r\exp(x)$ [6]. This map is visualized in figure 2.3. For control parameters $r > \frac{1}{e} = r_c$ (panel a), there is no intersection. Therefore, the map has no fixed points. If we decrease r to the value r_c, we can check easily that we get one intersection at $x = 1$. For the special control parameter $r = r_c$, the map f is tangent to the diagonal line. A further decrease of r to values $r < r_c$ creates two fixed points, as can be seen in panel c). One is stable and the other one is unstable. After all, the slope of the left fixed point has to be smaller and the one to the right larger one in order to have $f(x)$ cross from above the diagonal to lower values and vice versa. The value r_c, where the bifurcation takes place is called the critical parameter or bifurcation parameter.

During a change of r through the critical value r_c, we create two fixed points from void, while f is tangent to the diagonal for $r = r_c$. This bifurcation type is therefore called a tangent bifurcation or saddle-node bifurcation, when dealing with systems of higher dimension.

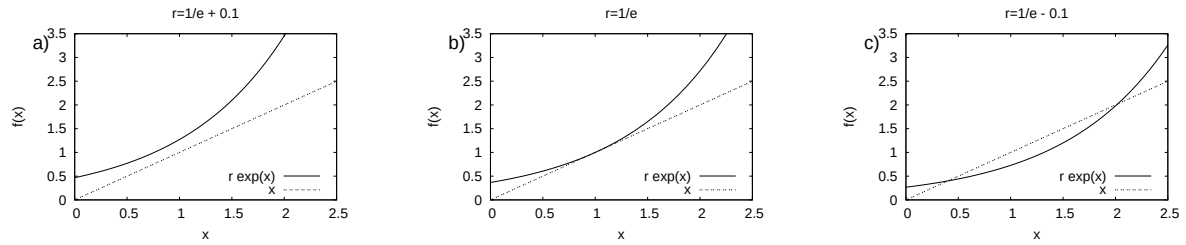

Figure 2.3: Bifurcation scenario for $f(x) = r\exp(x)$, which has a critical point at $r_c = \frac{1}{e}$. (a) The control parameter is larger than the bifurcation parameter. $f(x)$ has no intersections with the diagonal. (b) at the critical value $r = r_c$, $f(x)$ is tangent to the diagonal. For $r < r_c$, we get two fixed points, as can be seen in panel (c). The left fixed point is stable, while the other one is unstable.

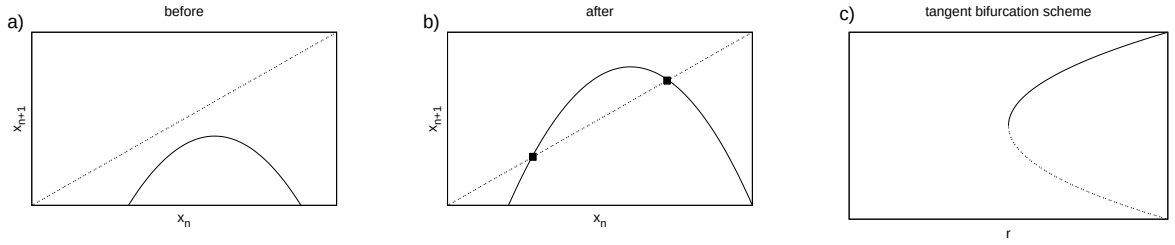

Figure 2.4: Tangent bifurcation scheme. Panel a) is before the bifurcation. We do not have any fixed points. b) After the bifurcation, two fixed points emerge. One is stable, the other one is unstable. c) The scheme of the bifurcation. Straight lines are stable fixed points, dotted lines are unstable.

The scheme of the tangent bifurcation is very general. The best way to remember it is to use figure 2.4 as the basic scheme.

2.5.2 Period Doubling Bifurcation

We will now come the the second bifurcation type. For this scenario, we will have a look at the well-known logistic map [33]

$$f(x) = rx(1-x) \qquad r > 0 \tag{2.5.1}$$

This map has a stable fixed point at

$$x^f = 1 - \frac{1}{r} \qquad \text{for } 1 < r < 3 \tag{2.5.2}$$

This fixed point is getting unstable at $r = 3 =: r_c$, because the magnitude of the slope reaches one in absolute value (cf. definition 8)

$$\left|f'(x^f)\right| = \left|r(1-2x^f)\right| = |2-r| = 1 \qquad \text{for } r = 3 \tag{2.5.3}$$

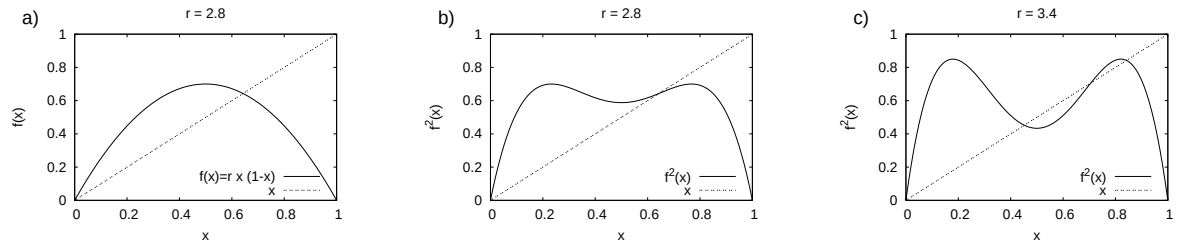

Figure 2.5: Period Doubling Bifurcation. In a) we see the logistic map for $r = 2.8$. There is one stable fixed point. b) shows the two-times iterated map. We have only one fixed point, which is the same as the fixed point in the normal map. For $r = 3 =: r_c$, the fixed point becomes unstable. Panel c) shows, that for $r > r_c$ the two-times iterated function has two more fixed points. These new fixed points are stable and form a period two orbit.

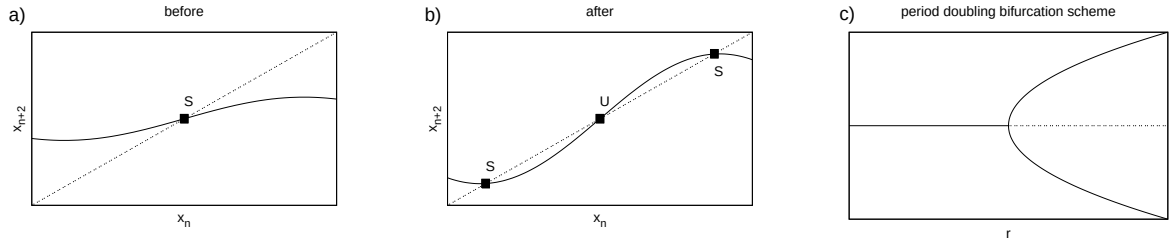

Figure 2.6: Schematic overview of a period doubling bifurcation. Panels a) and b) show the two-times iterated map before and after the bifurcation. The stable fixed point loses its stability in the bifurcation and gives rise to a stable period two orbit. c) shows the motif for such a bifurcation.

The fixed point is therefore unstable for $r > r_c$. But this is not the end of the story. We first note, that there is no additional fixed point created in this bifurcation, which can be verified from figure 2.5, panel a). But we can have a look at the two-times iterated map. For $r < r_c$, it has only one fixed point, namely the fixed point x^f. If we increase r through r_c, we see, that there are two new fixed points created in the two-times iterated map. These are stable and form a period two orbit.

The basic properties of this kind of bifurcation are compiled in figure 2.6.

A bifurcation, where a stable fixed point loses its stability and gives rise to a stable period two orbit is called a period doubling or pitch fork bifurcation. The name pitch fork bifurcation comes from the visualisation in panel c) of figure 2.6.

2.5.3 Inverse Period Doubling Bifurcation

The last bifurcation is very similar to the period doubling bifurcation and will be mentioned only briefly. It occurs when an unstable fixed point becomes stable and thereby creates an unstable period two orbit. This process is called an inverse period doubling bifurcation. We will only give the basic scheme of this bifurcation type in figure 2.7.

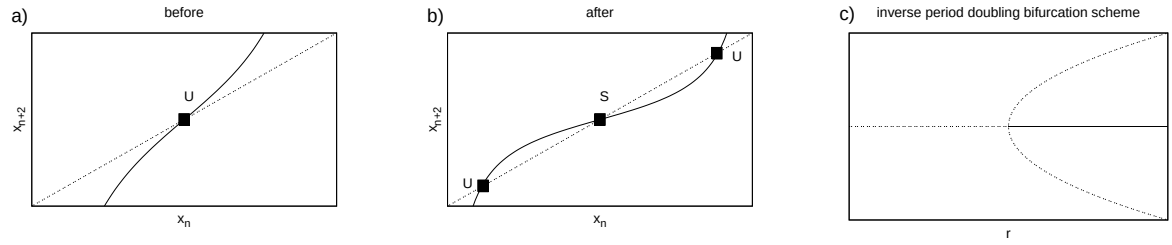

Figure 2.7: Schematic overview of an inverse period doubling bifurcation. For $r < r_c$, we have one unstable fixed point. This fixed point gains stability in the bifurcation and gives rise to an unstable period two orbit (panel b). Panel c) is the schematic motif.

All the generic bifurcations we can encounter in one dimension have now been defined. All these bifurcations can happen in the other direction as well. This depends on the explicit definition of the control parameter. The schematic description is obtained by folowing the schemes in the c) panels of figure 2.4, 2.6 and 2.7 from the right to the left.

2.5.4 Bifurcation Diagrams

Another useful tool to visualize bifurcation scenarios is to use bifurcation diagrams. In bifurcation diagrams, we plot the stable orbits of the system against the control parameter. Sometimes, additional unstable fixed points are included in those diagrams. But in order to have a clearly arranged plot, one skips this unstable fixed points most of the time.

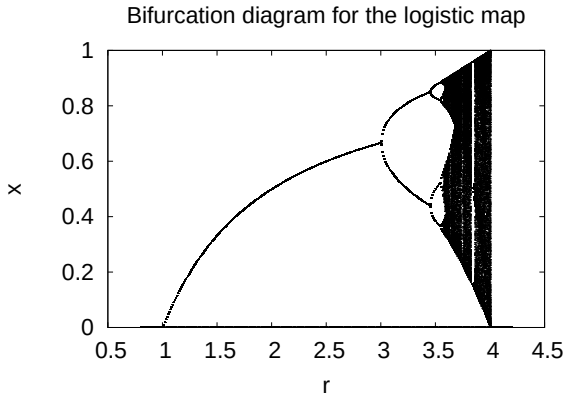

Figure 2.8: Bifurcation diagram for the logistic map. We can see the period doubling route to chaos and the boundary crisis at $r = 4$.

One can inspect in bifurcation diagrams, how the dynamics of a system evolves from a stable fixed point to a chaotic behaviour. The most famous mechanism for that is the period doubling cascade, known from the logistic map. This route to chaos is happening via successive period doubling bifurcations. After n bifurcations, we encounter a periodic orbit of period 2^n. $n \to \infty$ for $r \to r_\infty$ and we have a fully developed chaotic dynamics for $r \approx 3.57 = r_\infty$. The exact point r_∞ after infite period doublings has been determined by FEIGENBAUM [9]. The scenario is known as the period doubling route to chaos [33].

There are much more types of bifurcations for higher dimensional systems. The analysis and classification is much more involved, so that only a rough sketch can be given. An exposition on this topic has been given by ARNOL'D [2].

2.6 Transient Behaviour

This section will give a short introduction to the field of transients, which are related to bifurcation theory. Transient behaviour can be interepreted as the opposite of permanent behaviour. A dynamical system on an invariant subset will never leave this subset. This can be described as permanent behaviour. When talking of transient motion, we

are dealing with a dynamical systems, that has not approached an invariant subset and therefore can make a transition between several regions of the phase space. One example is the transition from a chaotic saddle to a stable fixed point, which is observed in turbulent pipe flow. A trajectory, which is making such a transition is called a transient. There are many kinds of transients, describing different kinds of dynamical behaviour. Some of them, which are important for our analysis, will be explained in this section.

The first phenomenon we will discuss is intermittency. We take as granted, that there is a critical parameter a_c in the system. For $a < a_c$, there exists a stable periodic orbit, which will be destroyed or get unstable for $a > a_c$. An example is studied by Pomeau and Manneville in [36] for the Lorenz system. For $a < a_c$, we can see a periodic signal in figure 2.9, panel a. As a is slightly above a_c, the signal looks very similar to the signal for $a < a_c$, but is sometimes intermitted with bursts, that are not periodic and show a chaotic motion. If we increase a further, such that it becomes significantly larger than a_c, the periodic patches in the signal get less and then dissappear. The system is now in a true chaotic state. It is not possible to investigate the behaviour of every single trajectory. But we can calculate some statistical features, that give us some insight into the mechanism of this behaviour.

One possibility is to measure the average time T between two subsequent chaotic bursts. This quantity tends to infinity, when approaching a_c from above.

$$\lim_{a \to a_c^+} T(a) \to \infty \tag{2.6.1}$$

This means, that the periodic behaviour is restored for parameters values a near the critical value a_c.

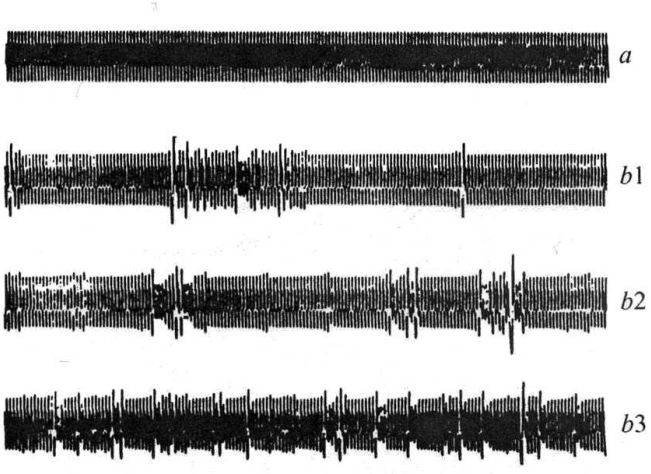

Figure 2.9: A signal of the Lorenz system. In a), we see a periodic signal. Due to intermittency, we get bursts in b1), which are becoming more frequent for b2). In b3), there is no more periodicity and the system has reached a chaotic state. Reprinted from [33].

We have taken $T(a)$ as an interesting measure to characterize the behaviour. This is a typical quantity to look at, when dealing with transients.

One is often interested in the scaling law of a characteristic time in dependence on the system parameter, or on the distance to a critical value. For the common case of a saddle-node bifurcation (cf. figure 2.4) at a_c, one observes a scaling law (cf. [33])

$$T(a) \sim (a - a_c)^{-1/2} \tag{2.6.2}$$

After all, for a value $a < a_c$, we have one stable and one unstable fixed point of our map f. These two fixed points merge and dissappear in the saddle-node bifurcation.

This leaves a very narrow tunnel behind, which can be seen in figure 2.10. The method of graphical iteration is used in figure 2.10. The next state can always be determined by subsequently going from the actual point to the diagonal and then to the function $f(x)$ again. A trajectory, which is injected into the tunnel needs a very long time to cross it.

This time can be calculated, if we approximate the function to quadratic order,

$$f(x_n) = x_{n+1} = x_n^2 + x_n + \epsilon \qquad \text{where} \quad \epsilon \sim (a - a_c) \tag{2.6.3}$$

If we are near the critical parameter, we obtain $\epsilon \ll 1$. This means, that a step in the tunnel is very small. Therefore, we can approximate x as a continuous function of n and rewrite equation (2.6.3) as

$$\frac{\mathrm{d}x}{\mathrm{d}n} = x^2 + \epsilon \tag{2.6.4}$$

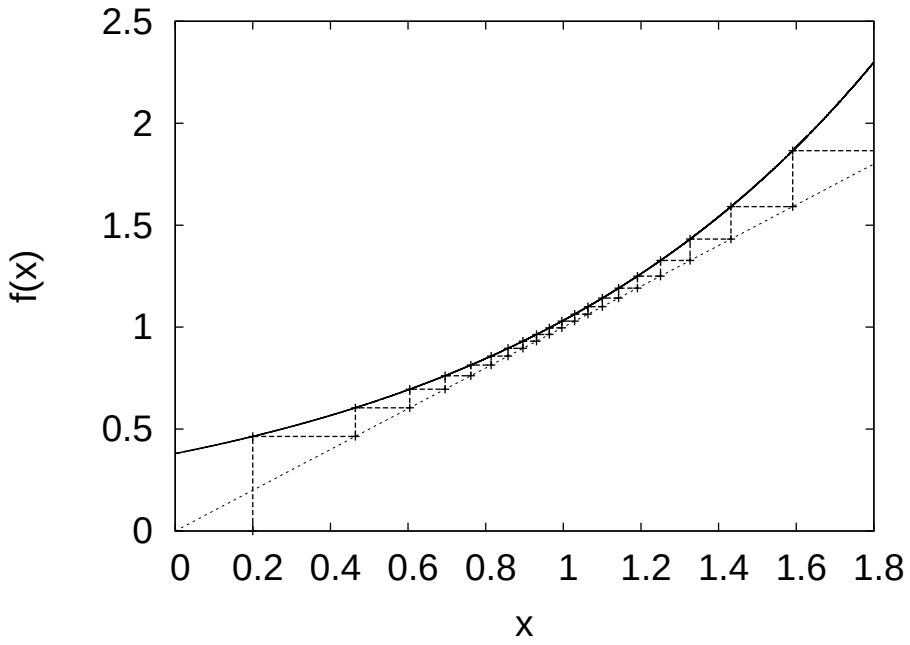

Figure 2.10: For control parameters near the critical value, a trajectory needs many iterations to cross the tunnel. Shown here is the example of the exponential map $f(x) = r\exp(x)$ near the tangent bifurcation at $r = 1/e$.

If we inject the trajectory at x_0, the time to cross the tunnel is given by

$$\int_0^T \mathrm{d}n = \int_{x_0}^{\infty} \frac{\mathrm{d}x}{x^2+\epsilon} \sim \epsilon^{-1/2} \tag{2.6.5}$$

Even with this coarse approximation, we see that this mechanism reveals the correct results.

After crossing the tunnel, the trajectory obeys a chaotic dynamics and will be reinjected into the tunnel. This leads to the characteristic time scale for periodic behaviour in between the chaotic bursts. We note, that the average time scales with the distance to the critical parameter a_c of the saddle-node bifurcation. This behaviour is known as intermittency and is a quite common scheme for transient behaviour.

The next part of this section will discuss the transition from a chaotic behaviour into an absorbing state, i.e. a stable fixed point. This behaviour is typical for a boundary crises, where an attractor hits its basin boundary. We will study this type of transition with the example of the logistic map (2.2.2).

$$f(x) = rx(1-x) \tag{2.6.6}$$

For $r = 4 =: r_c$, we have a chaotic invariant subset $I = [0, 1]$. When r is increased above r_c, I is no longer invariant under the evolution of f. In every iteration, some mass of I is mapped outside of it and we get the Cantor set I_f, which has been described in section 2.2. I is no longer invariant and we can calculate the average lifetime of a trajectory starting in I, i.e. the number of iterations until the trajectory leaves I.

Since we lose a constant fraction of our mass at each iteration, we expect an exponential distribution

$$P(t) \sim \exp(-t/\tau) \tag{2.6.7}$$

for the lifetime, which is also known from radioactive decay processes. τ is the average lifetime and $P(t)$ is the probability for a trajectory to have a larger lifetime than t. As in the intermittency example above, one is interesting in the scaling law of the average lifetime τ with the control parameter r. The probability to escape I is constant for each iteration, since the middle part of I is mapped outside I and the remaining part is mapped to the complete I again (cf. figure 2.1, panel b). Since the invariant measure at the critical point is smooth on I, the escape probability is proportional to the length of the hole L

$$\rho \simeq cL \tag{2.6.8}$$

with a constant c. The probability, that a trajectory is still in I after n timesteps amounts to

$$(1-\rho)^n \simeq (1-cL)^n = \exp(n \cdot \ln(1-cL)) \tag{2.6.9}$$

Comparison to equation (2.6.7) yields

$$\tau = -\frac{1}{\ln(1-cL)} \simeq \frac{1}{cL} = \frac{1}{c}\left(\frac{r-r_c}{r}\right)^{-1/2} \approx \frac{2}{c} \cdot (r-r_c)^{-1/2} \tag{2.6.10}$$

Here, we used (2.2.11) for the length of the hole. Hence, this boundary crisis leads to an average lifetime τ, that scales with the control parameter like

$$\tau \sim (r - r_c)^{-\gamma}, \qquad \gamma = \frac{1}{2} \tag{2.6.11}$$

This scaling law is quite general and also encountered in many boundary crises setups (cf. [13]). Even where the invariant measure prior to the crisis is a fractal measure, it still applies, even though with a different exponent γ. On the other hand, the argument is restricted to boundary crises, where the basin boundary is smooth. It fails for a fractal basin boundary. Since, in that case, it is not correct assume a constant escape probability. The holes in the attractor, which are created in the boundary crisis, are generally very small for a fractal basin boundary such that their size will not scale algebraically like $(r - r_c)^{\gamma}$. Since thus holes are very narrow, one rather obtains a scaling law like

$$\tau \sim \exp\left[C(r - r_c)^{-\gamma}\right] \tag{2.6.12}$$

with a constant C and exponent γ. One observes in this scaling law, that the average lifetime depends crucially on $r - r_c$. Due to the very strong divergence of the average lifetime τ for $r \to r_c$, one calles these transients super-long transients.

As shown by Grebogi, Ott and Yorke in [12], super-long transients can be created, for example, by an unstable-unstable pair bifurcation.

The scenario is compiled in figure (2.11). We can see two unstable fixed points. The one on the basin boundary is unstable in the transversal as well as in the longitudinal direction, compared to the boundary. The point on the chaotic attractor is a saddle, which is stable in the transversal direction and unstable in the longitudinal one. At the boundary crisis, these two points merge and create a very narrow tunnel in phase space, which can be seen in panel b. Trajectories on the prior attractor can now escape from the chaotic region and cross the boundary to leave the vicinity and move off to another region, maybe a stable fixed point.

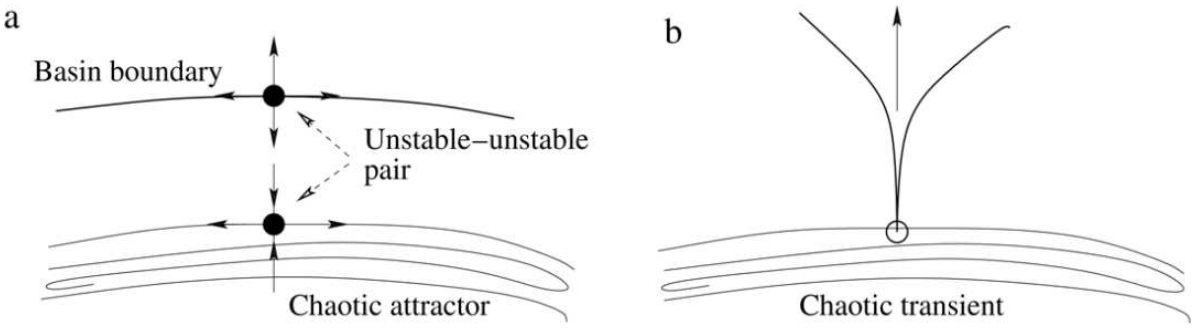

Figure 2.11: This figure shows the mechanism of an unstable-unstable pair bifurcation. (a) Before the merging crisis, we have an unstable pair which undergoes a saddle-node bifurcation in one direction. (b) After the crisis, the unstable pair has vanished leaving a narrow tunnel in phase space where trajectories can escape. The chaotic attractor has morphed into a chaotic transient. Reprint from [45].

Due to the scaling law (2.6.12,) the transients can have a very long lifetime. As a consequence, it is nearly impossible to distinguish between the motion on a chaotic attractor or the motion of a super-long transient. The trajectories look pretty much the same for an exceedingly large number of iterations. This problem is also encountered in turbulent pipe flow, where the question, if turbulent flow is permanent or transient with a super-long lifetime, is not completely answered yet [16].

We have now introduced the most common types of transient behaviour. In the next chapter, we will investigate a model system, which encounters an unstable-unstable pair bifurcation. The occurence of a fractal basin boundary, lifetime distributions and the scaling law (2.6.12) will be verified. Another system with much higher dimension will be introduced in chapter 4.

Chapter 3

A Mean-Field Model for Super-Long Transients

Beside experiments, numerical simulations of the Navier-Stokes equations and analytical solutions to the Navier-Stokes equations, there is another way to tackle the problem. It could be possible to build a simple, low-dimensional dynamical model system [47], which let us investigate some, but not all, aspects of turbulent puffs. With such a simple model we are able to achieve some analytical results really easily. Another advantage is, that simulations of such a model could be carried out really fast on present-day computers.

This chapter will introduce such a model system in order to gain some insight into the nature of super-long transients.

3.1 The Idea

In this warm-up problem, we would like to understand where the super-long lifetime of chaotic transients comes from. We recall some results from [45] and apply them to our new model system for pipe flow. Our aim is to work out the analogy between fluid dynamics and dynamical systems vocabulary. At this point we also clarify the things we will need in the next chapter.

The laminar state of pipe flow is a steady state, that is stable against small perturbations at least for Reynolds numbers up to 10^7. This fact let us model the laminar state as a stable fixed point of our dynamical model system. The next thing we will consider is the super-long lifetime of turbulent puffs. It has been shown by Ott, Grebogi and Yorke [12] that super-long transients are expected to emerge from an unstable-unstable pair bifurcation. In this process, an chaotic attractor collides with its fractal basin boundary, which leads to a boundary crisis and a hole in phase space is left, where trajectories can escape. Due to the fractal nature of the boundary, these holes are very small, and the trajectories needs a long time to find them. This mechanism can be used to model super-long transients. The third aspect is that the model system should be simple enough. Simple means easy to evaluate on a computer. This is an important point if we want to do simulations faster than a complete simulation of the Navier-Stokes equations. The last point is rather technical. We expect to do measurements of the pipe

turbulence in discrete time steps. This gives us the possibility to use a discrete time model, namely a mapping.

These points are now summarized

1. existence of a laminar, stable state for all Re
2. unstable-unstable pair bifurcation gives rise to the transition from turbulence to the laminar state with super-long transients
3. system as simple as possible to achieve fast simulations
4. time-discrete system

It is obvious, that such a simple model can neither give us the whole variety of turbulent structures nor can it be applied to real systems without limitations. But we can learn some basic concepts the nature of super-long transients. The simplicity of the model is seen as a feature, not as a lack of applicability. If we accept these constrains, we can learn much about the physics of transients, which occur in several fields of physics and nature.

This model is introduced and discussed in the next section.

3.2 The Model

This model is supposed to be a mean-field model. There is no spatial extension and the state of the system is defined by only two dynamical variables x and y. We can think of x as the energy stored in the turbulence and of y as the configuration of this energy (i.e. a point on an energy shell, cf. [47]). Since we are dealing with a mean-field model, we can only tell if the system is turbulent or not. There is no way to see a transition from convective to absolute instability or the moving of a puff through a pipe.

First, we will discuss the single dynamics for x and y seperatly and then introduce the coupling between them.

3.2.1 Uncoupled Dynamics

We will first focus on the x-dynamics, which is the coordinate that determines the turbulence. The simplest non-linear mapping would be a quadratic function $x_{n+1} = x_n^2$, where $n \in \mathbb{N}_0$ is the discrete time of the system. In order to influence the x-dynamics, we introduce a control parameter a, which shifts the map like $x_{n+1} = x_n^2 + a$. This gives us the opportunity to investigate some bifurcations of the system. In addition to that, we need a stable fixed point to model the laminar state. This laminar state is arbitrarily chosen to be at $x = -2$.

Collectively, we get the mapping (cf. figure 3.1)

$$x_{n+1} = f(a, x_n) = \begin{cases} -x_n^2 + a & , x \geq x_* \\ -2 & , x < x_* \end{cases} \tag{3.2.1}$$

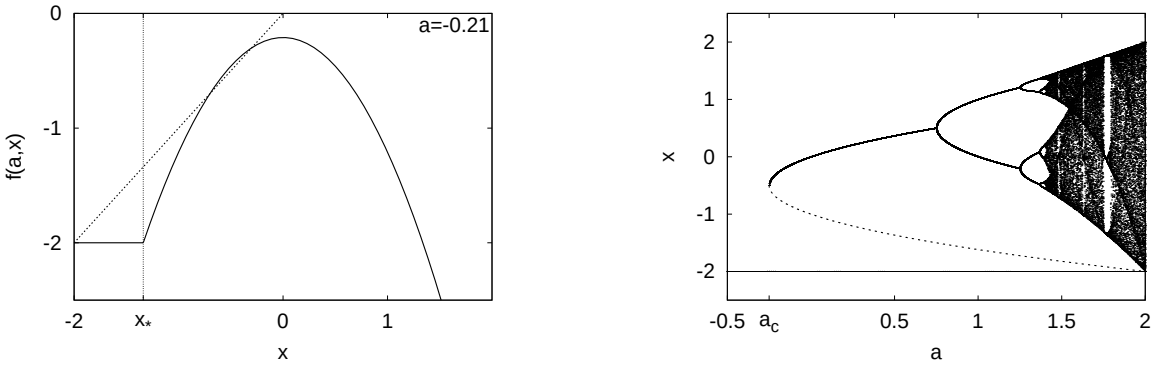

Figure 3.1: The left image shows the x-dynamics for $a = -0.21$. The bifurcation diagram is shown on the right side. Dots are the simulated points, the dashed line is the computed position of the unstable fixed point, escaping from the saddle-node bifurcation.

where x_* is the intersection of the two branches of f with the value $x_* = -\sqrt{2+a}$ (cf. figure 3.1). This means that for values $x < x_*$ the system goes directly to the laminar fixed point while we have a non-trivial dynamics for $x > x_*$.

We will now have a closer look on the fixed points of f. The fixed point equation (2.2.3) gives us up to three different fixed points

$$x_0^f = -2, \qquad x_{1/2}^f = -0.5 \pm \sqrt{0.25 + a} \tag{3.2.2}$$

Here, the critical value is $a_c = -0.25$. For $a < a_c$ we have only one real fixed point, namly x_0^f. In this case x_0^f is a global attractor, since x is bounded by $\max(f)$ to the top and values $x < x_*$ are mapped to x_0^f. Two new fixed points occur in a tangent bifurcation as a crosses a_c from below and x_0^f is no longer a global attractor. This can be understood by analyzing the stability of the fixed points. Therefore, we calculate the first derivative of our map f.

$$f'(a, x_n) = \begin{cases} -2x_n & , x \geq x_* \\ 0 & , x < x_* \end{cases} \tag{3.2.3}$$

We already know from section 2, that a fixed point is stable, if $|f'| \leq 1$. This gives us the result, that x_0^f is stable regardless of a. We also get that x_1^f is unstable for $a > a_c$. At creation at $a = a_c$, the fixed point x_2^f is stable. It loses its stability at $a = 0.75$, where $\left|f'(x_2^f)\right|$ crosses 1. The loss of stability of x_2^f gives rise to a period doubling bifurcation, as it is well known from the logistic map [9].

Another interesting point is the basin of attraction of these fixed points in the parameter region $a \in [a_c, 0.75]$. The basin of attraction for x_2^f is given by $I_2 := [x_1^f, -x_1^f]$. Note that $x_1^f < 0$. Since there are only two stable fixed points in this parameter range, the basin of attraction for x_0^f is $I_0 := \mathbb{R} \setminus I_2$. For $a > 0.75$ the fixed point x_2^f undergoes a period doubling cascade to chaos. At $a = 2$ we can compute that the condition $x_* = x_1^f = -2$ is fulfilled. This is the indicator for a non-generic boundary crisis, where the attractor in I_2 loses its stability. For $a > 2$ the dynamics are no longer well defined, since $x_* < -2$

and -2 is no longer a fixed point, which means that we lose the laminar state and our model makes no sense any more.

This results can be compiled into a bifurcation diagram. This diagram can be computed by a little computer algorithm, which is described in the following

1. choose a control parameter a
2. take N random initial condition $x_i,\ i \in \{1, \ldots, N\}$
3. iterate the x_i with the map f for n_0 timesteps
4. iterate each trajectory for another n_1 timesteps and output the values
5. go back to 1) for another a

It is important to note that our algorithm can only determine the stable orbits[1]. The bifurcation diagram for f is illustrated in figure 3.1.

We would like to trigger an unstable-unstable pair bifurcation according to the mechanism in [45]. Therefore, we are only interested in parameter values near a_c. We have analyzed the most important aspects of the x-dynamics and can now turn our focus on the second direction.

The y-dynamics is responsible for the chaotic dynamics, which we need for the boundary crisis in the unstable-unstable pair bifurcation. It is advantageous to take a periodic map. This keeps the interesting phase space bounded and one can therefore do faster simulations. So we propose a map $g(y) = g(y + Y)$ with some period Y. The obvious choice would be a simple sine $g(y) = \sin(y)$. But there is a problem with this mapping, because it is impossible to solve the fixed point equation $x = \sin(x)$ analytically. In order to avoid this technical problem, we use a 'linear version' of the sine function, which is defined as (cf. figure 3.2,left)

$$g(b, y_n) = \begin{cases} by_n & , -0.5 < y_n \leq 0.5 \\ b(1 - y_n) & , 0.5 < y_n \leq 1.5 \\ \text{etc.} & \end{cases} \tag{3.2.4}$$

Another advantage is the symmetry of this function, which further simplifies the task to compute fixed points, their stability and bifurcation diagrams. We have chosen the slope b to be the control parameter for this dynamics. The period of the function is set to $Y = 2$.

From the fixed point equation, we see that g has also up to three fixed points,

$$y_0^f = 0, \qquad y_{1/2}^f = \pm\frac{b}{b+1} \tag{3.2.5}$$

For this special choice of g it is quite easy to compute the stability of the fixed points, because we have $|g'| = b$, irrespective of the point we are interested in. For $b < 1$, we

[1] Unstable fixed points can be computed by applying backward iteration, since they are stable of inversed time flow.

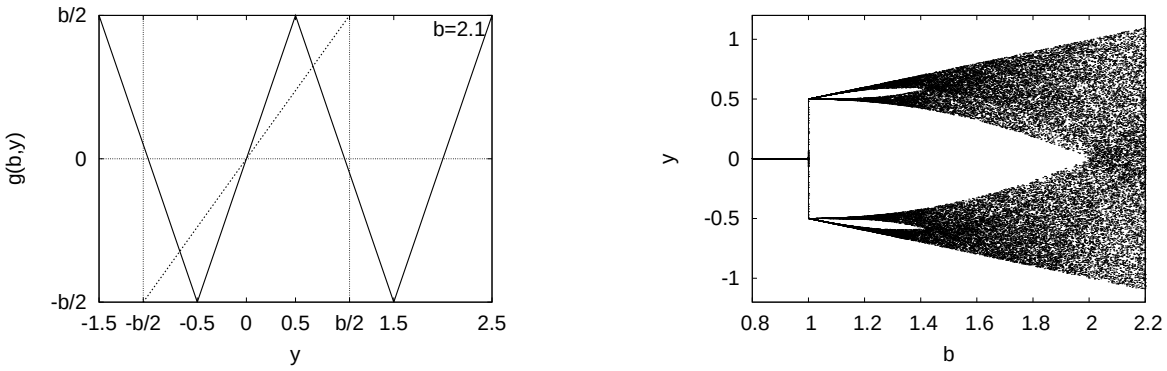

Figure 3.2: The left image shows the y-dynamics for $b = 2.1$. There are three fixed points of the map. The bifurcation diagram is shown on the right side. A merging of the two bands is happening at $b = 2$, where we expect chaotic behaviour.

have only one fixed point at y_0^f. This fixed point is stable and a global attractor, since g is bounded. A non-generic bifurcation is encountered at $b = 1$. At this parameter, we have infinitely many fixed point, which are all marginally stable. But at $b = 1 + \epsilon$ for an arbitrary small $\epsilon > 0$, we get the three fixed points given in (3.2.5), which are clearly all unstable. For values $1 < b < 2$ there is a decoupling of the two branches. Initial conditions starting with $y_i > 0$ stay in the positive region, while trajectories with $y_i < 0$ stay in the negative region. We are effectively dealing with two independent tent maps, which have the same dynamics with inversed sign. Since the tent map is topologically conjugated to the logistic map, we get the same bifurcation behaviour like the logistic map. g is exhibiting a period doubling route to chaos. The two independent bands are becoming chaotic and merge at $b = 2$. The two independent branches start to communicate again and we have a chaotic dynamics on the whole domain. This fact is supported by the investigation of the bifurcation diagram displayed in the right panel of figure 3.2. Our aim was to trigger an unstable-unstable pair bifurcation. The y-dynamics has the job to contribute with a chaotic dynamics. For this case, we choose the system parameter to be $b = 2.1$ for the rest of this section.

We have now a good understanding of the x and y-dynamics seperately. But super-long transients need at least two dimensions (cf. [45]), since we need a fractal basin boundary for the small holes in phase space. This rises the question for a sufficient coupling between this two directions. That problem is tackled in the next section.

3.2.2 Coupling

As already mentioned, the unstable-unstable pair bifurcation should be triggered by the coupling. The lifetime of the transients is then depending on the coupling strength ϵ. This coupling strength is meant to be the only parameter of the system and is related to the Reynolds number. In order to take ϵ as the only system parameter, we need to fix a and b to sensible values. As mentioned above, the y dynamics should be chaotic on the whole domain. Therefore, we set $b = 2.1$ as a value slightly above the band merging

point $b = 2$. In x direction, we choose a parameter $a = a_* := -0.21$ as a starting point. Since $a_* > a_c$, we are above the bifurcation point, where a chaotic attractor is coexisting with the fixed point at x_0^f. The idea for the coupling is, that we can introduce it in a way, that the y dynamics can trigger the bifurcation. This means that a strong coupling strength ϵ can destroy the chaotic attractor in I_2. Therefore, we introduce the coupling in a way to shift the control parameter a through the bifurcation point.

$$a = a_* - \epsilon |y_n| \qquad \epsilon > 0 \tag{3.2.6}$$

The absolute value of y prevents the coupling to shift a in the wrong direction. The strength of the coupling can be adjusted by ϵ. The maximum shift is given by

$$\max(\epsilon |y|) = \frac{\epsilon b}{2} = 1.05\epsilon \tag{3.2.7}$$

The definition (3.2.6) leads to a critical coupling strength, which is defined as the coupling strength, where we encounter the unstable-unstable pair bifurcation, namely at $a = a_c$. After rearranging (3.2.6), we get

$$\epsilon_c = \frac{a_* - a_c}{\frac{b}{2}} \approx 0.047 \tag{3.2.8}$$

for $a_* = -0.21, a_c = -0.25$ and $b = 2.1$.

With this coupling definition, we have a global attractor at $x = -2$ for $\epsilon > \epsilon_c$. We will mention that the word attractor only refers to the x direction. The dynamics in y-direction is always chaotic and we are always using the x dynamics to classify the behaviour of the system. Is is worth noting that the y dynamics is not influenced by x. Therefore, it can be iterated independently. In the case where $\epsilon < \epsilon_c$ there exists two fixed points in x, namely $x_{1/2}^f$. This leads to an attractor in the interval $I_A := [x_1^f, -x_1^f]$. Here we have to keep in mind, that x_1^f depends on a and eventually depens on y. We will denote I_A as the attractor region.

There is another point to make on the definition of ϵ. When we compare it to the control parameter of turbulent pipe flow, we can try the obvious relation $\epsilon \sim \mathrm{Re}^{-1}$. The value of ϵ decides, which lifetime the transient will have. The larger ϵ is, the shorter is the average lifetime.

The evolution equations can now be summarized as

$$x_{n+1} = f(a_* - \epsilon |y_n|, x_n) \tag{3.2.9a}$$
$$y_{n+1} = g(b, y_n) \tag{3.2.9b}$$

This system can be simulated in order to check, if it shows the expected behaviour. The first step is to analyze the lifetime for different initial conditions. We mark a trajectory as 'dead' if it is at the stable fixed point $x = -2$. The algorithm we will now introduce is called the phase space algorithm from now on and is defined by some simple steps

1. create a grid with mesh size α in the interesting phase space region
2. take the nodes of the grid as the initial conditions for the simulation

3. iterate each initial condition with the equations (3.2.9)
4. associate to each node the number of iteration needed to reach the dead state
5. plot the lifetime as a color-coded plot in phase space

The computational effort of this algorithm scales quadratically with the mesh size α, such that it is very hard to reach very high resolutions.

The phase space plots for two values of ϵ are shown in figure (3.3). The attractor appears as a green region. For $\epsilon < \epsilon_c$, the white region is the basin of attraction for the attractor in I_A and the coulored region is the basin of attraction of x_0^f, where these two regions are separated by the basin boundary. For $\epsilon > \epsilon_c$, the attractor is destroyed in an unstable-unstable pair bifurcation. Beyond this bifurcation, the white region denotes the region where a trajectory first stays in the region of the prior attractor before moving off to the laminar fixed point. The coulored region then stand for those initial condition, which immediatly move to x_0^f whithout spending time in I_A. The boundary is now called the edge of chaos, which is sperating trajectories with this different behaviour.

In addition to the color-coded lifetime, we have plotted a single trajectory of the system starting in I_A for 10^{10} iterations. The spiky basin boundary attracts the attention while looking at the phase space plots. This suggests a fractal basin boundary, which is a condition for the unstable-unstable pair bifurcation and the super-long transients. This fractal behaviour stems from the chaotic y dynamics. Another striking aspect is the symmetry in the plots. This comes from the symmetry of g and the coupling via the absolute value $|y|$.

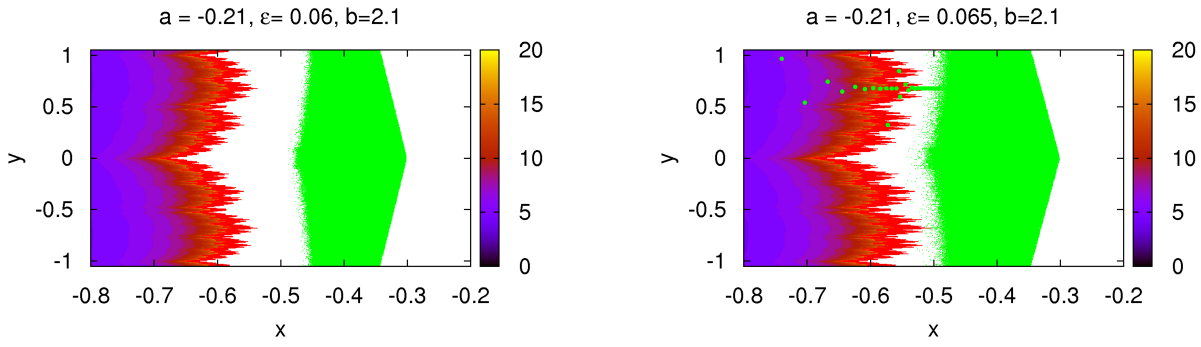

Figure 3.3: We see a phase space plot of the system. The color codes the number of iteration needed to reach the laminar point at $x = -2$. Green dots indicate a single trajectory starting at a random initial point in the region around x_2^f. The left panel shows a plot for $\epsilon = 0.06$, where we do not see an escaping trajectory. The right panel is for a slightly larger coupling $\epsilon = 0.065$, where an escaping trajectory is encountered close to $(x, y) = (-0.5, 0.7)$. The last dots of the trajectory have been plotted in larger size to improve their visibility.

We do not see any points at the edge of chaos for $\epsilon = 0.06$. It seems that all iterations of the trajectory stay in the region I_A, although $0.06 > \epsilon_c$. This fact is investigated further in section 3.4. For $\epsilon = 0.065$ we can see that after about $1.3 \cdot 10^{10}$ iterations the trajectory approaches the edge of chaos, crosses it and moves off to the laminar point.

In the next two subsections, we will determine the shape of the edge of chaos with a very high accuracy then analyse and the distribution of the average lifetimes of the transients.

3.3 Computing the Edge of Chaos

The edge of chaos seperates states of fundamentally different behaviour [47]. States on the laminar side move directly to the laminar fixed point, while states on the chaotic side move to the chaotic region first and seem to follow the trajcetory of the prior chaotic attractor before they eventually find a hole in the boundary and escape to the laminar point. Since the holes are very small for a fractal basin boundary near the critical value, the trajectories nearly never notice escape channels and therefore evolve like trajectories on an attractor. In practice, it is often very hard to decide whether an observed trajectory moves on an attractor or if it is just a transient to another region in phase space.

The phase space algorithm described above is quite good for scanning the phase space for the lifetime at several points, but its high requirements on computer time, severely hinders a high resultion of the edge, i.e. a small mesh size. Therefore, we implemented another algorithm which is specialized to find the edge with high accuracy. It will be denoted as the 'edge tracking algorithm'.

We first need to point out, that a fixed point, which is stable, is unstable if we inverse the time flow. In forward direction, points very close to the edge at the laminar side move to the laminar fixed point. The idea is to take an initial point near the laminar fixed point and compute the preimages of that point, which rapidly generates a highly accurate approximation to the edge of chaos.

Each backward iteration yields several preimages. Since the y dynamics is decoupled from x, it is useful to start the backward iteration process with y. As seen in figure 3.2, y_{n+1} has up to three preimages y_n, depending on its value. Therefore, we need to find the value $g(b, b/2)$, which gives us the lower bond for where y_{n+1} has three preimages. This can be easily calculated to be

$$g(b, b/2) = -b(b/2 - 1) = -0.105, \qquad \text{for} \quad b = 2.1 \tag{3.3.1}$$

Due to the symmetry of g, we found, that for $y_{n+1} \in [-0.105, 0.105]$, we have three preimages. Otherwise we get only two. Once we found the preimages of y_{n+1}, we are able to calculate those for x_{n+1}. The quadratic part of f gives us two preimages. The coupling depends on y and therefore we get four to six preimages for a given state (x_{n+1}, y_{n+1}). But these preimages do not all lie on the boundary. We can see from the plots, that only negative x values build the boundary. Therefore, we do not need to take the positive x values into account. We also do not need them in the further application

of the algorithm, because positive x values have no preimages, since $\max(f) < 0$ for the values of a and ϵ we are interested in.

Now we can think of a little estimate for the resolution quality of the edge tracking algorithm. As mentioned above, we get two to three interesting preimages. We apply the preimage computation to a depth of 20 levels, by applying the algorithm to each preimage, we got in the first step, again and again. This gives us at least 2^{20} interesting preimages of a point near the laminar fixed point. We suppose that these points are all lying on the edge of chaos, since the phase space algorithm suggests, that 20 steps are enough to reach the laminar point, if we have crossed the boundary. The length of interest in y direction is $\Delta y = 2.1$ as can be seen from the phase space plots. That yields a resolution of $2.1/2^{20} \approx 2 \cdot 10^{-6}$ for the edge tracking algorithm. This can be compared to the mesh size of the phase space algorithm, which is $\alpha = 0.001$. So we see, that the edge tracking algorithm is much more efficient for determining the boundary than the more general phase space algorithm.

A comparison of the two algorithm shows, that the boundary is the same in both cases, but with higher resolution in the edge tracking algorithm. The high resolution results support the assumption of a fractal boundary. Although this is not a mathematical proof, we can check if the lifetime scales like we expect it from the mechanism proposed in [12] for fractal basin boundaries. Rather, a fractal basin boundary is also expected, since $\lambda_y > \lambda_x$ for the Lyapunov exponents in x- and y-direction, respectively (cf. [47]).

3.4 Lifetime Plots

We will now come to the question of how the average lifetime of the transients behaves with varying coupling strength. In order to calculate the lifetime, we randomly selected $N_0 = 2000$ initial condition for each coupling strength in the chaotic region and let them evolve until the trajectory is dead. The number of iterations is taken to be the lifetime τ_i for this initial condition. Then we take the average lifetime as

$$\tau = \frac{1}{N_0} \sum_{i=1}^{N_0} \tau_i \tag{3.4.1}$$

where τ_i is the lifetime of the i-th random initial condition.

Another possibility we have tried is the following. Since we are dealing with a decay process, we expect that the number of initial conditions that are still alive after a time t scales like

$$N(t) = N_0 \exp(-t/\tau) \tag{3.4.2}$$

With a log-normal plot we can compute τ via a linear fit to the data. Both methods of computing τ yields the same results within the numerical accuracy.

After having defined the computational methods, the task is now to determine the dependence of the lifetime τ on the distance to the critical point $(\epsilon - \epsilon_c)$. The first thing we notice in the phase space plots is, that even at values quite above ϵ_c, i.e. at $\epsilon = 0.06$, we do not encounter any escaping trajectories from the chaotic region. In order to analyze this issue, we compute the average lifetime for different values of $\epsilon > \epsilon_c$, larger

than $\epsilon = 0.06$. This gives us simulation data for $\tau(\epsilon - \epsilon_c)$. We fitted this data with the scaling law suggested by [12, 45].

$$\tau \sim \exp(C(\epsilon - \epsilon_c)^\chi) \tag{3.4.3}$$

The plot is shown in figure 3.4. As we can see from the fit, the expected scaling law is found in the simulation data. We are now convinced, that we are dealing with super-long transients. The meaning of 'super-long' is well demonstrated by calculating τ for different coupling strength with our fitted function.

For $\epsilon = 0.65$ we get $\tau = 1.3 \cdot 10^7$ out of the fit, which is in very good agreement with the data. 10^7 iterations can easily be done on our computers[2], even with quite some computing time. We can now calculate the average lifetime for a slightly lower value, where we have not seen any escaping trajectories, namely for $\epsilon = 0.06$. The fit tells us, that we should expect a value like $\tau \approx 10^{28}$. This is the explanation why we were not able to resolve any transients in this case. The computing time for 10^{28} iterations is far out of reach of computers.

This results shows, that we are dealing with super-long transients escaping from an unstable-unstable pair bifurcation. The edge of chaos is fractal and supports a superexponential scaling law for the average lifetime. We see that the average lifetime is very strongly diverging, which is due to the fact that $\chi = -4.49$. This scaling law assumption is only valid for $\epsilon > \epsilon_c$ and the average lifetime goes to infinity for $\epsilon \to \epsilon_c$. This can be

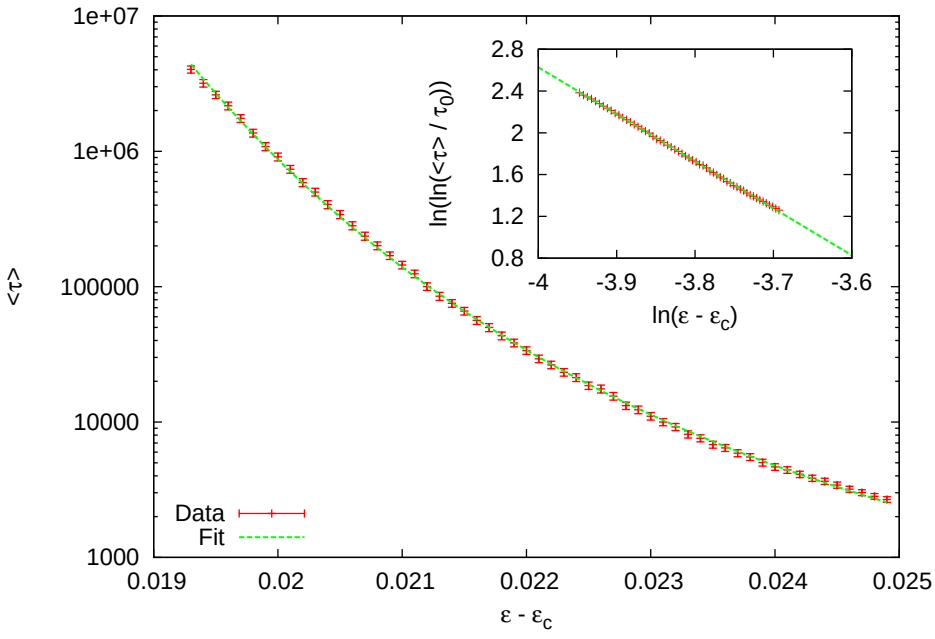

Figure 3.4: The average lifetime for different values of ϵ. The fitted data is given by the scaling law $\tau = \tau_0 \exp(C(\epsilon - \epsilon_c)^\chi)$, where $\tau_0 = 79.04$, $C = 2.1e - 7$ and $\chi = -4.49$. The inset shows a double log-log plot in order to verify (3.4.3). The straight line supports the expected scaling.

[2]We used a computer with an Intel Core 2 Duo 3GHz CPU and 3GB RAM

compared to our introductory question of the average lifetime of turbulent puffs. For $\mathrm{Re} < \mathrm{Re}_c$, we have an exponential scaling of the average lifetime of turbulent puffs, where for $\mathrm{Re} > \mathrm{Re}_c$ the lifetime is infinity, which means that a turbulent puff is never decaying.

3.5 Summary

After motivating the idea for the model, we presented our implementation of the dynamics. The x-dynamics is responsible for the tangent bifurcation while the y-dynamics give rise to the unstable-unstable pair via the chaotic dynamics. The coupling has been introduced in a way that it triggers the interesting bifurcation by only one parameter, which is the coupling strength ϵ. Lifetime plots were given for different ϵ in which we could see, that the computationally resolvable lifetime is encountered for coupling strengths far beyond the critical value ϵ_c. This is verified a posteriori with the fitted curve of average lifetime to the simulation data, which assures the exponential scaling law of super-long transients and gives us the possibility to calculate the lifetimes for values of the coupling strength really near to ϵ_c.

We also investigated the basin boundary between the laminar and the chaotic region with a very high accuracy. This supports the suggestion that we are dealing with a fractal basin boundary. This fact is also supported by the average lifetime scaling law, since the lifetime is expected to be super-long only for a fractal basin boundary. Our edge tracking algorithm is presented in a short paragraph to show how good the accuracy is compared to the phase space algorithm.

Summing up, we have found a model system, which shows super-long transient behaviour. The model shows, that super-long transients are not exotic objects with no physical meaning. The quite simple mechanism of an unstable-unstable pair bifurcation is used as a stereotype of a bifurcation, which creates super-long transients. These transients do not show a power-law scaling like at a crisis in a syste with one unstable direction and a smooth basin boundary. Hence, this analysis demonstrates, that super-long transients can be modelled by simple models.

The underlying dynamics has been tested and they build the basis for further analysis of a slightly more complicated model, namely a unidirectional coupled map lattice, which is investigated in the next chapter.

Chapter 4

An Unidirectional Coupled Map Lattice (uCML) for Pipe Turbulence

Hof et al. [16,17] have shown, that turbulent puffs have a super-exponential scaling law with the Reynolds number

$$\tau \sim \exp(C\mathrm{Re}^{\gamma}) \tag{4.0.1}$$

and may hence be viewed as an instance of a dynamical system with super-long transients. Additionally, very accurate measurements [34] and computer simulations [30] on the Navier-Stokes equations have shown linear stability of the laminar pipe flow profile up to Reynolds numbers of 10^7. This leads to the well accepted fact, that the laminar state is a stable fixed point and a turbulent puff a trajectory on a high-dimensional chaotic saddle with several unstable directions [4,7,8,23,24]. Since turbulent puffs have a finite length, while travelling through the pipe, they are identified to be a convective instability. They flow downstream without any significant change of width.

At a larger Reynolds number Re_{Sl} the convective instability turns into an absoulte instability. The turbulence spreads throughout the pipe and finally fills it completely. This state is known as a turbulent slug [32,51]. A slug can not be characterised by its

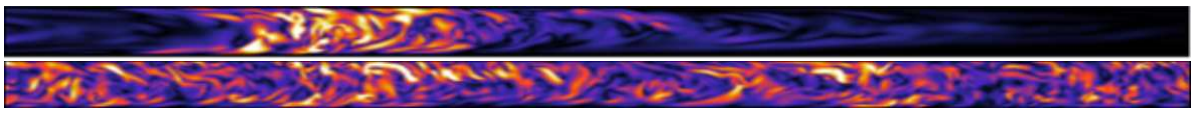

Figure 4.1: Top: simulation of a turbulent puff for Re = 2250. The size of the turbulent structure stays finite and therefore is identified as a convective instability. Bottom: turbulent slug for Re = 2800. The perturbation increases in size and eventually fills the whole pipe. This is known as an absolute instability. Reprint from [32].

lifetime, since this is infinite per definition. The important quantity to look at is the average growth, which can be measured in dependence on Reynolds number.

In order to gain qualitative insight into the scaling of lifetime of convective instabilities in quasi one-dimensional systems, i.e. for puffs, and the transition to absolute instability flows, i.e. from puffs to slugs, we construct and analyse a spatially extended,

one-dimensional system. In this chapter, which shows these transitions. Because of the simplicity of the system one can do very fast computer simulations and study the transition mechanisms analytically. This gives us the opportunity to gain insight into the fundamental aspects of these transitions from a dynamical systems point of view and helps to improve the understanding of turbulent structures in pipe flow.

Thus, this model shall give us insight into the behaviour of turbulent puffs and slugs, just like the model from chapter 3 gave us some knowledge about the nature of super-long transients.

Since we are not using the Navier-Stokes equations in our simulations, no statements on real values like critical Reynolds numbers, can be made. But there are useful analogies between real parameters and our system parameters. Rather than the Navier-Stokes equations, a coupled map lattice will be studied, as discussed in the following section.

4.1 Why CML?

A spatially extended system is needed in order to provide travelling structures, like puffs in a pipe. After all, turbulent puffs are observed in very long pipes.

In experimental setups, the length L of a pipe is typically three orders of magnitude larger than its diameter D. Studies on coherent structures in pipe flow have shown that those structures can be described by the analysis of several cross-sections along the axis [42].

All these assumptions can be interpreted as a lattice in one dimension, i.e. a chain, which has a dynamics that is updated at fixed time steps (cf. figure 4.2).

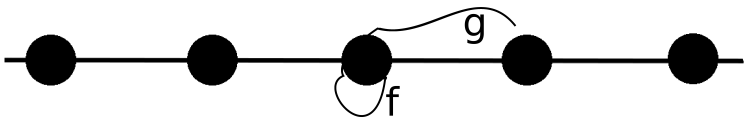

Figure 4.2: Visualisation of a one-dimensional lattice. The state variables are updated at discrete time steps. f is the on-site dynamics and g the coupling function.

Each site of the chain describes a slice of the pipe. In addition to that, a quantity to describe the level of turbulence is needed. This quantity can be taken to be the average energy or vorticity of a slice of the pipe. This is a value $x_t^i \in \mathbb{R}$, which can be determined for each time t and each space i. The quantity x_t^i is influenced by a local dynamics, i.e. it is strongly affected by the Reynolds number. Its on-site dynamics will be described by the one-dimensional mapping

$$f : \mathbb{R} \to \mathbb{R}, \qquad x_{t+1}^i = f(x_t^i) \tag{4.1.1}$$

In order to get an interaction between sites, a coupling g is neccesary. It is generally defined as

$$g : \mathbb{R}^m \to \mathbb{R}, \qquad g(x_t^1, \ldots, x_t^m) = x_{t+1}^i \tag{4.1.2}$$

Since we want to model turbulent puffs, which travel downstream, we choose a undirectional forward coupling. This means, the coupling only depends on the next upstream neighbour.

All these conditions define a system, which is referred to as a coupled map lattice in textbooks [3].

Definition 12. *A Coupled Map Lattice (CML) is a discrete-space, discrete-time lattice with on-site dynamics $f : \mathbb{R} \to \mathbb{R}$ and coupling $g : \mathbb{R}^m \to \mathbb{R}$, which obeys the evolution equation*

$$x_{t+1}^i = \alpha g(x_t^1, \ldots, x_t^m) + f(x_t^i) \qquad \forall i \in \{1, \ldots, m\} \tag{4.1.3}$$

x_t^i is the state variable at time t and site i. α is denoted as the coupling strength.

For a nearest-neighbour forward coupling $x_{t+1}^i = \alpha g(x_t^{i-1}) + f(x_t^i)$, such a system is called a unidirectional CML (uCML).

This completes the basic definitions of the model system.

This section should have made clear, why a unidirectional CML is a good model to study, when dealing with turbulent puffs. This model will give us the opportunity to simulate structures similar to turbulent puffs and slugs. The great advantage is, that the simplicity of the uCML enables us to analyse some features analytically. The choice of mappings is also very good, when it comes to computer simulations. Simulations are very fast, because we only have to compute the evolution of the state variables for discrete time and space.

In order to study the space-time behaviour of the uCML, the on-site dynamics f and the coupling function g have to be defined first. Then we can investigate, how the system parameters change the space-time behaviour and have a look at some space-time plots. This will be done in the next section.

4.2 Model and Space Time Behaviour

The definition of the general model of a uCML will be completed by the concrete on-site dynamics and coupling. In doing so we try to keep the system as simple as possible. We will first introduce the on-site dynamics.

A turbulent puff can be seen as a trajectory on a chaotic saddle. Therefore, we need a leaky chaotic region in our local dynamics, where trajectories can escape. The simplest map with those properties is the tent map. It has the advantage to be piecewise linear. This makes analytical calculations very easy to handle. Additionally, it is topologically conjugate to the logistic map. Therefore, we already know the fixed points and bifurcation behaviour from our model in chapter 3. An additional benefit is that no windows with stable periodic orbits exist. The height h of the tent is chosen to be the control parameter for the local dynamics. The second fact is, that the laminar state should be stable for all Reynolds numbers of interest. Therefore, the local dynamics should have a stable fixed point for every value of h. This setup allows a transition from the

chaotic saddle to the stable fixed point, which mimics the relaminarisation scenario for turbulent puffs. These conditions can be used to define the on-site dynamics as

$$f(x) = \begin{cases} h(x-\delta) & \delta \leq x < 1+\delta \\ -h(x-2-\delta) & 1+\delta \leq x \\ 0 & x < \delta \end{cases} \tag{4.2.1}$$

δ is a free parameter of the system, seen as a shift in the dynamics (cf. figure 4.3). The distance $\delta > 0$ seperates the stable fixed point from the chaotic region. We will keep $\delta = 0.1$ fixed throughout the whole work. The parameter dependence of the uCML on δ will not be investigated. This leaves the height h as the only control parameter, which also determines the slope

$$f'(x) = \begin{cases} h & \delta \leq x < 1+\delta \\ -h & 1+\delta \leq x \\ 0 & x < \delta \end{cases} \tag{4.2.2}$$

and therefore, defines the stability of fixed points. f has up to three fixed points

$$x_0^f = 0\ , \qquad x_1^f = \frac{h\delta}{h-1}\ , \qquad x_2^f = \frac{h(2+\delta)}{1+h} \tag{4.2.3}$$

x_0^f is always stable and mimics the laminar state of the pipe. The stability of x_1^f and x_2^f is controlled by h.

In order to obtain an escaping, chaotic dynamics, we use values $h \geq 2$. For $h_c := 2$, the system exhibits a boundary crisis in which trajectories can escape from the chaotic region. This can be seen from the bifurcation diagram in figure 4.3, but can also be computed analytically.

The chaotic region is defined as the region between x_1^f and $p := (2+\delta) - (x_1^f - \delta)$ (cf. figure 4.4).

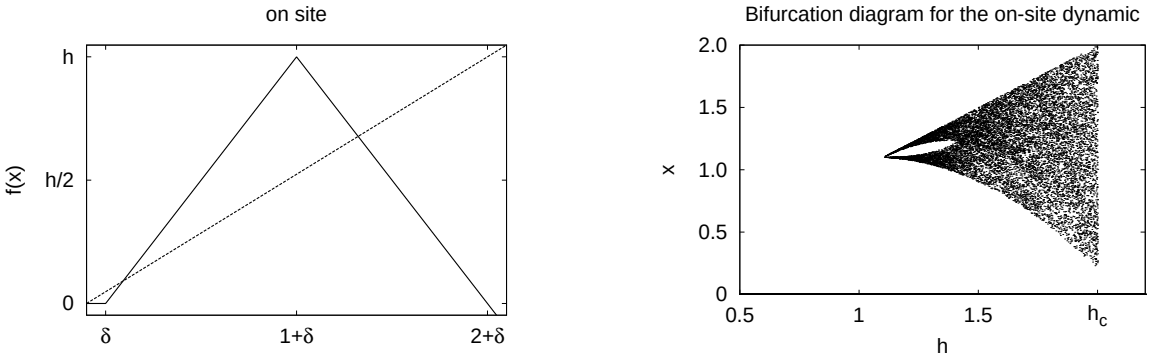

Figure 4.3: Left: plot of the on-site dynamics f. We have a stable fixed point at $x_0^f = 0$ and two more fixed points in the adjacent region. Right: bifurcation diagram for the tent map. For $h = h_c$, there is a boundary crisis.

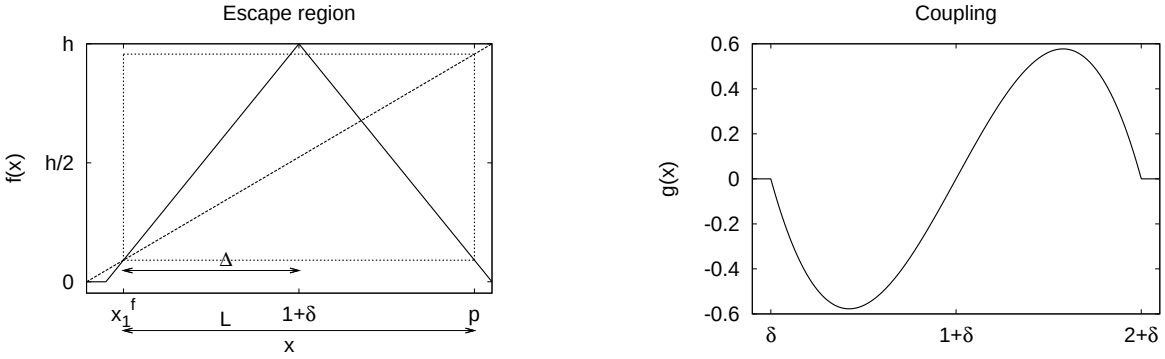

Figure 4.4: Left: values near $x \approx 1 + \delta$ are mapped to larger values than p for $h > h_c$. This denotes a non-vanishing escape probability. Right: the coupling of the uCML. g has a fixed point at $x = 0$.

This can be understand, by taking values of x into account, that are mapped beyond p. These values will eventually move to the laminar fixed point x_0^f, since they are mapped to the left of x_1^f, which is unstable for $h > 1$. The marginal condition for an escape from that region is therefore given as

$$f(1 + \delta) = p \tag{4.2.4}$$

since $1+\delta$ is the point, where f has its maximum, namely $f(1+\delta) = h$. Using equation (4.2.3), we can express p in term of δ and h

$$p = 2 + 2\delta + \frac{h\delta}{1 - h} \tag{4.2.5}$$

The condition (4.2.4) can now be written as an equation that defines the critical height h_c in terms of δ

$$h_c = 2 + 2\delta + \frac{h_c\delta}{1 - h_c} \tag{4.2.6}$$

This equation has two solutions, $h_c = 1 + \delta$ and

$$h_c = 2 \tag{4.2.7}$$

The solution $h_c = 1 + \delta$ marks the point, where the tent hits the diagonal line for the first time. This determines the beginning of the bifurcation scenario, where $x_1^f = p$. This is an uninteresting point for the simulations of turbulent puffs. Therefore, we concentrate on $h_c = 2$. This is the point of the boundary crisis (cf. bifurcation diagram 4.3, right panel). Since, we are interested in turbulent puffs, we will only investigate the dynamical behaviour for values $h > h_c$. This implies, that the fixed points x_1^f and x_2^f are always unstable, the Lyapunov number is larger than 1 (cf. (4.2.2)). The only stable fixed point is x_0^f. We can see in the bifurcation diagram, that f follows the same route to chaos as a branch of the piecewise linear sine map from chapter 3. For $h = h_c$, we have a boundary crisis, which gives us the opportunity to see transient behaviour.

After having defined the local dynamics f and identified important parameter values we will now come to investigate the coupling g. The coupling should have a special form to support travelling structures, like turbulent puffs. This will be done by a forward

coupling. If a site is in the laminar state, it can not spread turbulence to its downstream neighbour. This fixes g at the fixed point $x_0^f = 0$ to

$$g(0) = 0 \tag{4.2.8}$$

In addition to that, we only want to trigger turbulence, if the upstream neighbour is in the turbulent region. This yields

$$g(x) = 0 \qquad x < \delta \tag{4.2.9}$$

We now choose the coupling in a way, that

$$g(x) > 0 \qquad 1 + \delta \leq x < 2 + \delta \tag{4.2.10a}$$
$$g(x) < 0 \qquad \delta \leq x < 1 + \delta \tag{4.2.10b}$$

This leads to the behaviour, that a turbulent site in $1 + \delta \leq x < 2 + \delta$ can kick the downstream laminar neighbour into the chaotic state via a positive coupling. The negative part of g can reduce the turbulence at the downstream site or can even pull it back to the laminar state. This can be interpreted, that a puff can take energy from a turbulent downstream region. In conclusion, the coupling is defined as

$$g(x) = \begin{cases} -1.5(x-\delta)(x-1-\delta)(x-2-\delta) & \delta \leq x < 2+\delta \\ 0 & \text{else} \end{cases} \tag{4.2.11}$$

Note, that g has no free parameters, since δ is fixed. A dependence on α will be explained seperately section (cf. section 4.6).

Further, $g(x)$ has only one fixed point at 0. This fixed point is stable (cf. figure 4.4, right panel) and a linear perturbation does not apply a positive coupling, so that the laminar state is still stable. After having defined th local dynamics as well as the coupling function g, we address the question of the correct boundary and intial conditions.

A general problem in pipe experiments is the finite length of the pipes. This problem can be overcome in simulations, where the number of sites can be increased, within the limits of computational power. A better possibility is to use period boundary conditions. This keeps the phase space small and one needs less memory than storing large lattices, in which most cells are in the uninteresting, laminar state. Since the coupling reaches only one site downstream, one can therefore implement very efficient algorithms to simulate the model. But one has to keep an eye on the length of the structures. If the structure extends through the whole pipe, one would get feedback effects due to periodic boundary conditions. Those trajectories would have no relevance to real systems and therefore have to be avoided.

Since we want to study turbulent puffs, we start with a system that is in a laminar state. That means, that each site is initially at the laminar fixed point x_0^f, corresponding to laminar pipe flow. A puff is experimentally created by blowing a small amount of water into the laminar pipe. This perturbation then travels through the pipe. We will perturb the first site of our uCML and investigate the space-time behaviour of the system. For

initial perturbation $< \delta$, it is immediately decaying and the systems remains laminar. This is due to the fact, that the laminar state is linearly stable. For perturbations in $[\delta, 2+\delta]$, the on-site dynamics as well as the coupling is non-vanishing. This can produce travelling structures along the lattice, just like puffs in a pipe. Therefore, we take a value in $[\delta, 2+\delta]$ as initial condition for the first site.

We have now everything we need in order to simulate the system. The space-time behaviour is shown in figure 4.5 for several parameter values.

A great variety in the evolution of the states can be seen in the plots. The abscissa describes the time of the system, while the ordinate denotes the site number of our lattice. The colour is coding the state variable x at each site. The range is chosen to run from $[0, 2+\delta]$. Therefore, black sites are in the laminar state, while coulored sites have a different degree of turbulence.

In panel a), we can see that for $h = 2.1$ and non-vanishing $\alpha = 0.2$ no structures travel through the lattice. For larger values, at $\alpha = 0.5$, there are structures that run through the lattice (panel b) and the lifetime of these structure is significantly larger for coupling strengths, e.g. $\alpha = 0.8$ in panel c). For $\alpha = 2.8$ the front is travelling much faster than the back. This behaviour will be interpreted as a turbulent slug. Slugs disappear again in our model for larger coupling strengths $\alpha > 4.0$ (panel e). Panel f) shows, that even for a small coupling strength of $\alpha = 0.5$, the lifetime is very long, if we decrease the height h to values closer to h_c. These space-time plots give a first hint about the different behaviour of the system for varying control parameters α and h. To arive at a more comprehensive description, we consider now lifetimes and velocity distributions, obtained by averaging over many trajectories.

We will study the dynamics of the uCML for different parameters combinations in the next sections. The physical analogies with pipe flow will explicitly be investigated. The limits of the model will also be discussed. In doing so, we will highlight solutions, that can also be determined analytically, since they are the best points to learn fundamental things. In those cases, we make some predictions from theoretical considerations and check our assumptions with the simulations of the system. The lifetime of turbulent puffs, as the most prominent quantity, will be discussed first.

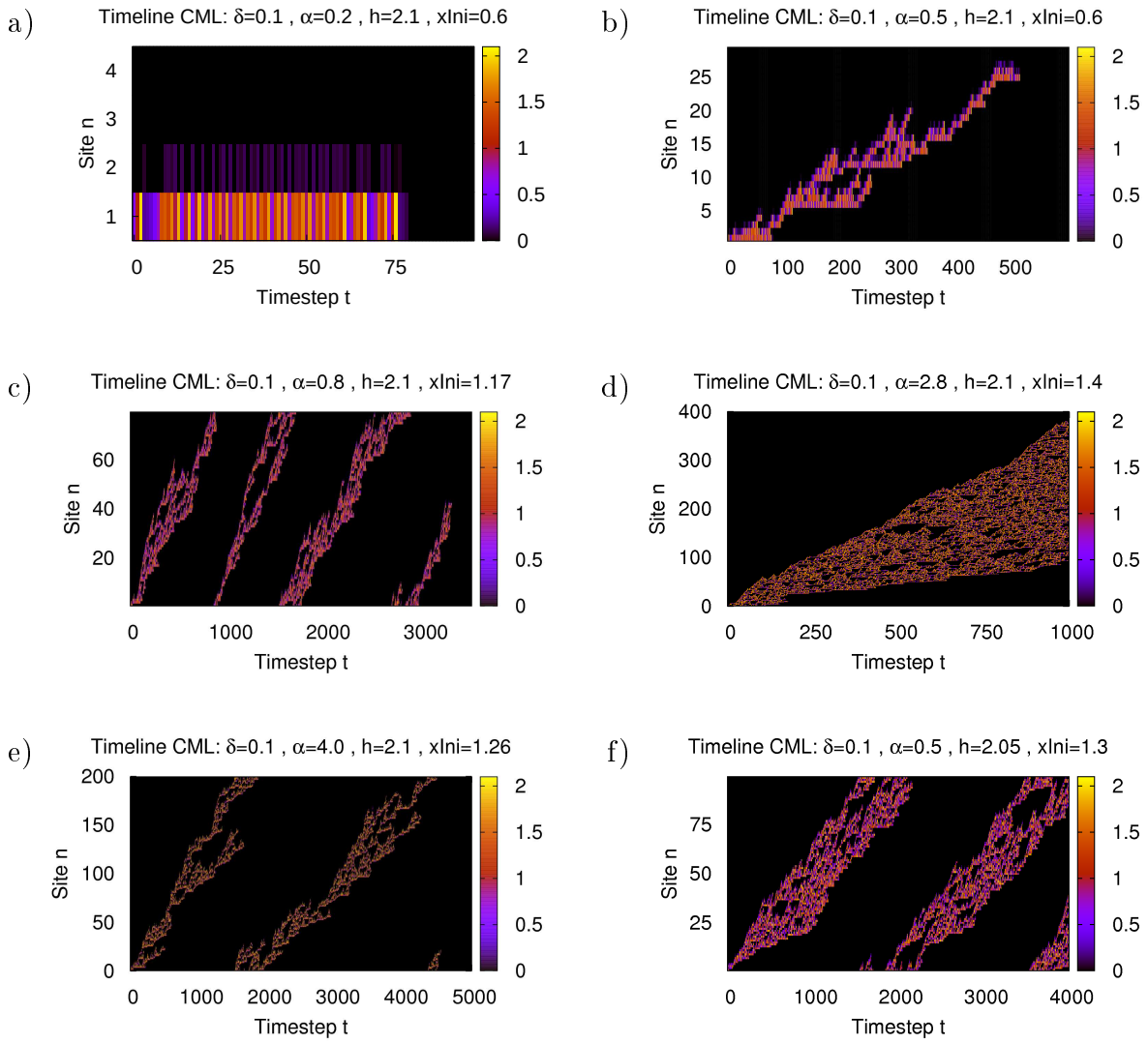

Figure 4.5: Space time behaviour of the uCML for different α and h. Panel a) shows the system behaviour for small coupling α. Since, the coupling is too weak, the perturbation never spreads to distant sites. For $\alpha = 0.5$, there are some structures starting to travel through the pipe (cf. panel b). These structures have an increased lifetime for stronger coupling $\alpha = 0.8$ (cf. panel c).This is what we call a turbulent puff. Another transition can be determined around $\alpha = 2.8$, where the lifetime goes to infinity. This is the turbulent slug regime. Here, the growth is highly increased. For even larger coupling in e), the system goes back to finite-size structures. This is a special feature of our system, which is discussed in chapter 5.1. Panel f) shows, that for smaller h, long lifetimes can be expected for very small α.

4.3 Lifetime Distributions

The finite pipe length is always a limiting factor, when one is interested in lifetime scaling laws for high Reynolds numbers. We will now measure the lifetime of turbulent puffs in the system described in section 4.2.

Turbulent puffs in experiments relaminarise without a known cause. This decay seems to be independent of the age of a turbulent puff, i.e. how far it has travelled from its origin. This leads to a lifetime distribution

$$P(t) \sim \exp(-t/\tau) \tag{4.3.1}$$

with a characteristic or average lifetime τ. This lifetime distribution is also expected in our simulations. If we first limit our considerations to the uncoupled case $\alpha = 0$, then the decay is determined by the on-site dynamics f only. f, on the other hand, is controlled by the height h. Here, like in the example in chapter 3, we always delete a certain fraction of our invariant subset in each timestep. This leads to a distribution (4.3.1), (cf. derivation in chapter 2). For the coupled case, the local decay rate is still governed by the on-site dynamics f, but is influenced by the coupling g. This leads to a distribution (4.3.1), but with significantly larger τ.

To determine τ we consider $N_0 = 30.000$ initial conditions, i.e. perturbations to the first site of our laminar system. These initial condition are chosen with a constant step size of $\Delta = 10^{-4}$ starting from $x = 0$. Then, we iterate the system for each inital condition until it relaminarises. This time is taken as the lifetime for this particular inital condition.

After sorting the data according to the lifetime and numbering each row, we get the quantity $N(t)$, which describes, how many trajectories have still survived until time t. This quantity is proportional to the lifetime distribution, when scaled with the number of initial condition N_0. Therefore, we expect a law like

$$N(t) \sim \exp(-t/\tau) \tag{4.3.2}$$

One would expect a straight line for $N(t)$ on a logarithmic scale, if the assumption of a decay, independent on age, is correct. The plots are given in figures 4.6 and 4.7.

In the large part of the plot, we see that the data for $\alpha = 0$ and $h = 2.1$ resemble a straight line. This is exactly, what we have expected from (4.3.1). The abrupt decrease for $t = 0$ comes from initial conditions, that are $< \delta$ or $> 2 + \delta$, respectively. These initial conditions decay immediatly, as can be seen from the definition of f and g. Therefore, we get a steep decrease for $t = 0$. Although we effectively lose some of the initial conditions, we can determine a linear decrease in the logarithmic plot about three orders of magnitude. Another interesting aspect is shown in figure 4.7. It shows the lifetime distribution for non-zero coupling $\alpha = 0.8$. In that case, there still is an exponential distribution, but with a significantly larger τ (beware the different x axis scales). We have therefore verified the assumption, that the lifetime of the chaotic structures have an exponential distribution

$$P(t) \sim \exp(-t/\tau) \tag{4.3.3}$$

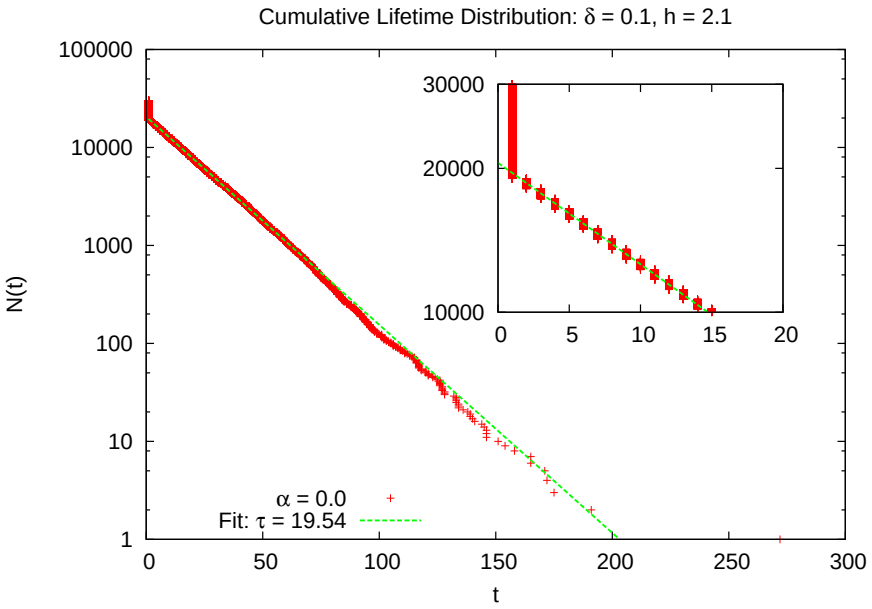

Figure 4.6: Lifetime distribution. The number of surviving trajectories at time t have been plotted against t. The large panel shows the cumulative distribution of lifetimes for zero coupling. This resembles the single site lifetime determined by (2.6.7). The inset shows a magnification at small t. A fast approach to the asymptotic scaling is observed. The fit parameters for the asymptotic scaling is given as $\tau(\alpha = 0.0, h = 2.1) = 19.54$.

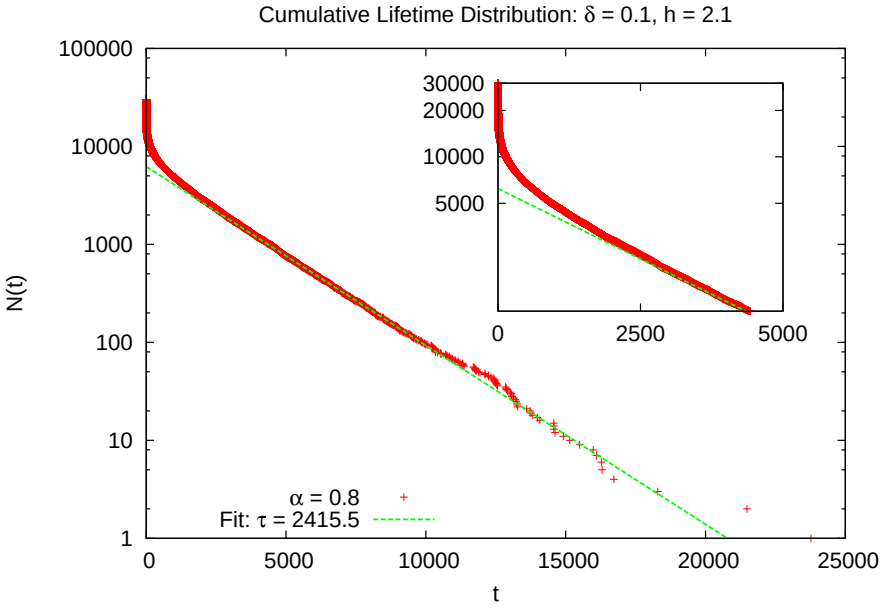

Figure 4.7: Lifetime distribution for $\alpha = 0.8$. We can see, that the lifetime distribution is also given by (4.3.1). The inset shows, that much more time is needed to reach the asymptotic. This is due to the creation of travelling structures for the coupled case. The fit parameters is $\tau(\alpha = 0.8, h = 2.1) = 2415.5$.

We will explore in the rest of this section, how the average lifetime τ scales with the system parameters, i.e. the coupling strength α and the height h.

As mentioned above, we can compute the average lifetime τ from the slope of the logrithmic plot of the distribution. This gives us τ in dependence on α and h, i.e. $\tau(\alpha, h)$. First, we check the dependence of τ on h for a fixed α. This analysis will be done for the uncoupled case $\alpha = 0$ first and then for arbitrary α. For $\alpha = 0$, $\tau(h)$ can be derived from the on-site dynamics f only. In order to analyse it, we have a look at the survival probability for one time step.

We denote the length from x_1^f to p as L. The length from x_1^f to the intersection of f with p will be denoted as Δ (cf. figure 4.4 for definitions). The probability to stay in the chaotic region for one time step is then given as

$$\rho_1 = \frac{2\Delta}{L} = \frac{2\Delta}{p - x_1^f} \tag{4.3.4}$$

This be expressed via the slope of the tent map and is therefore determined by h,

$$f'(x) = h = \frac{p - x_1^f}{\Delta} \qquad \forall\ x \in [x_1^f, 1 + \delta) \tag{4.3.5}$$

This yields

$$\rho_1 = \frac{2}{h} \tag{4.3.6}$$

Since the rest of the interval is strechted to the whole length again, and since the invariant density is constant on the interval for a linear map, the survival probability after t timesteps is

$$\rho_1^t = \left(\frac{2}{h}\right)^t \tag{4.3.7}$$

A comparison with the distribution (4.3.1) then gives

$$\rho_1^t = \exp\left(-\frac{t}{\tau}\right) \qquad \Rightarrow \qquad \tau = \left(\ln\frac{h}{2}\right)^{-1} \tag{4.3.8}$$

This expectation can now be compared to the data. Figure 4.8 shows the simulation data. We will first restrict our considerations to the uncoupled data for $\alpha = 0$. The data points are the green points, which form the lower curve. The solid red curve is the scaling law (4.3.8), which has been fitted to the simulation data. The expected scaling law fits the simulation data perfectly. But there is another specialty that need to be highlighted. On top of the data points for the uncoupled case lie the points for a small coupling $\alpha = 0.1$. These points are more or less the same as for no coupling. We will study this quite astonishing behaviour extensively in the next section.

If we now have a look at the data for larger coupling, we see that these curves are very different than those for zero coupling. The mechanism, that gives us the correct scaling law, is not as trivial as in the uncoupled case. Obviously, the divergence for $h \to h_c$ is much stronger than for $\alpha = 0$. One can think of a scenario of an unstable-unstable pair bifurcation as an explanation. The chaotic saddle is determined by the local dynamics

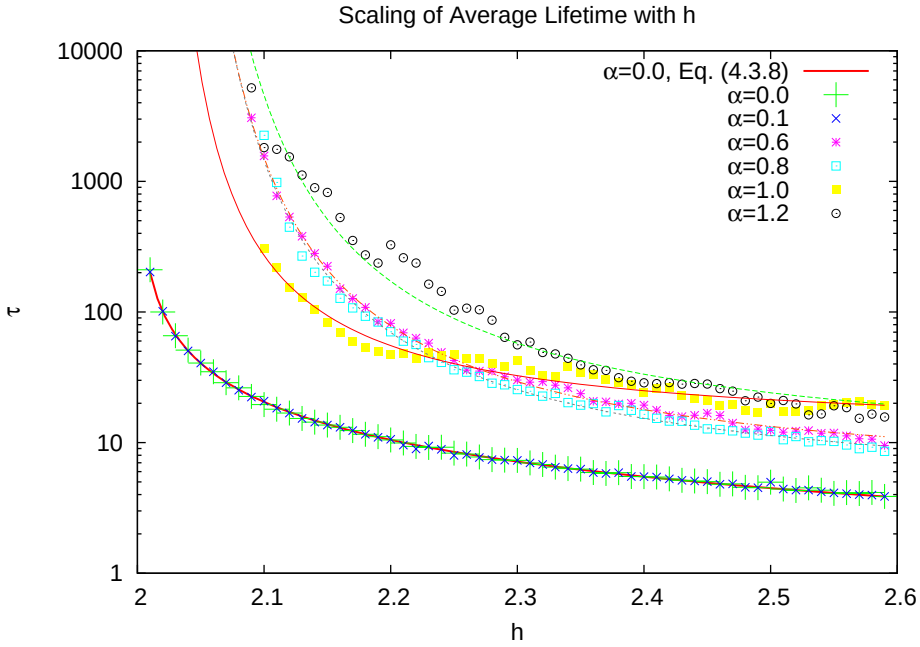

Figure 4.8: The scaling of the average lifetime with the height h of the on-site dynamics. We have plotted simulation data for zero coupling and $\alpha = 0.1$. These data points are perfectly described by the analytical solution in (4.3.8). For larger couplings $\alpha > 0.3$. we have a different scaling law. The data points can be fitted by the super-long transients scaling law (2.6.12).

f for $h > 2$. The second unstable direction can be related to the coupling of g to the next neighbour. If this mechanism would be a good description, then we would expect a scaling law like (2.6.12). Indeed, in figure 4.8 we show data for larger couplings of $\alpha = 0.6, 0.8, 1.0$ and 1.2, which are fruitfully fitted by lines of the form

$$\tau = B \exp\left(C\,(h - h_c)^{-1}\right) \tag{4.3.9}$$

according to the scaling law (2.6.12). One can see, that the fits describe the data points within a good accuracy. The interesting fit parameter $C(\alpha)$ is shown in figure 4.9.

The wiggling of the data points around the fit can be described by the way, the data point were obtained. In order to get one data point, one has to fit the distribution with a linear fit. The main interest lies in quite large lifetimes. Therefore, that fit has to be good for lifetime larger than a threshold. This threshold has to be changed for each α and h, since for $\alpha = 0$ lifetime of 100 are large, while for $\alpha = 0.8$ a threshold of about 1000 is needed to obtain good results from the fit. This is the problem with determining the asymptotics of lifetime distributions spanning several orders of magnitude. Due to this fact, the data points are not as accuracte as the data for $\alpha = 0$. Another thing to mention is the behaviour of the prefactors B and C with varying α. The curves $B(\alpha)$ and $C(\alpha)$ do not show a simple dependence on α. This can also be seen in the fact, that curves are not properly arranged according to their α values (cf. figure 4.8). Since, we have verified the scaling law (2.6.12) for quite large couplings, it is clear that we are indeed dealing with super-long transients. This is a great step forward in the simulation of turbulent puffs, which are expected to have a super-long lifetime scaling law.

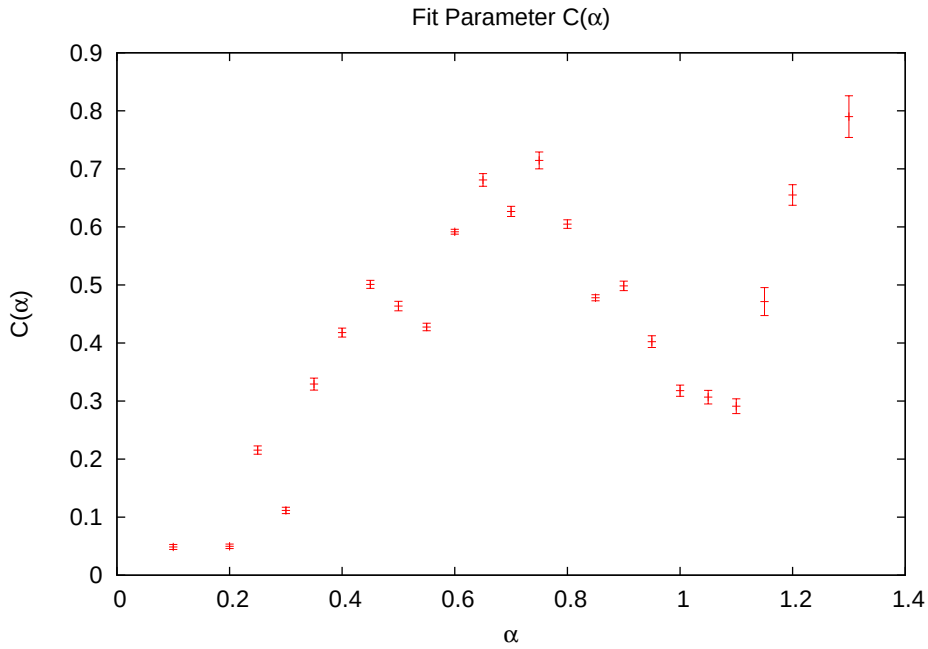

Figure 4.9: Fit parameter $C(\alpha)$ for lines in figure 4.8 and (4.3.9)

Since, the scaling law $\tau(h)$ is understood, we will now have a look at the dependence of τ on α. Therefore we fix $h = 2.1$. The scaling law is given in figure 4.10.

The first thing, that attracts the attention, is the heavily fluctuating lifetime around $\alpha = 0.7$. It decreases again for $\alpha = 0.8$ and rises again for $\alpha = 1.2$, but this time, the increase is very steep.

The inset shows a magnification for small α. In agreement with the findings of figure 4.8, there is no increase in average lifetime until a critical parameter α_{cr} is reached. The whole structure of $\tau(\alpha)$ is really complex and will not be investagited in detail. Rather we focus on the origin and the positions of the sharp increase in the lifetime close to α_{cr}, $\alpha \approx 0.6$ and $\alpha \approx 0.8$.

To clearly trace the transitions, we show the complete parameter dependence in a two-dimensional parameter plot (figure 4.11), where the average lifetime is shown as colour, enconding the average lifetime on a logarithmic scale, normalised to the single site lifetime $\tau(\alpha = 0)$[1]. The complex structure of the parameter space becomes visible in this plot. Particularly, the large peak shown in figure 4.10 for $h = 2.1$ and varying α can be clearly seen in the plot. For larger h, the peak at $\alpha = 0.8$ seems to vanish faster than that at $\alpha = 1.3$. Moreover, there seems to be a clear line for the lifetime increase at $\alpha = 0.25$, i.e. the value $\alpha_{cr} = 0.25$ appears to depend at best very weakly on h. in the next section, we will focus on the sharp increase of the average lifetimes near α_{cr}, which marks the onset of turbulence.

[1]The logarithmic scale is useful, since the average lifetime ranges about many orders of magnitude (cf. figure 4.10). Therefore, yellow points have a 10 times larger lifetime than red points.

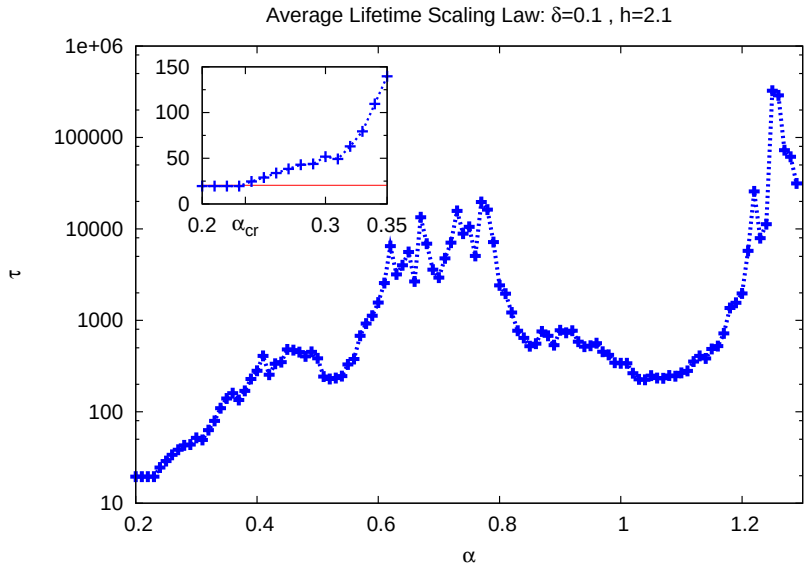

Figure 4.10: Scaling of the average lifetime with coupling strength α for fixed height h. The scaling law is not as smooth as $\tau(h)$ for fixed α. We see several spiky regions, that are intermitted with quite smooth behaviour. The lifetime is very high for $\alpha \approx 0.7$, falls again one order of magnitude and increases for $\alpha > 1.0$. Due to the coupling, the lifetime can increase by 3 orders of magnitude beyon the value $\tau \approx 20$ for the single cell dynamics.

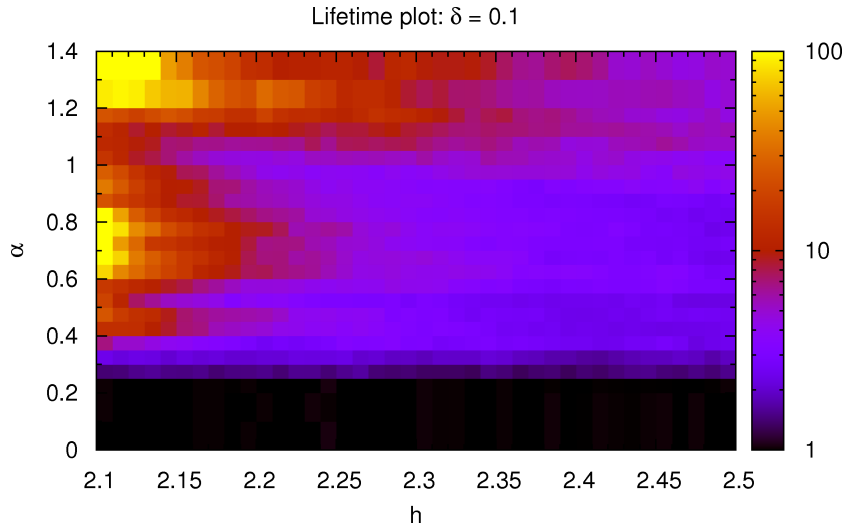

Figure 4.11: The complete parameter space of the system. The colour is coding the average lifetime of the system, normalised by the zero coupling lifetime defined in (4.3.8). We can see, that the structure is quite complex. The boundary between very long and short lifetime is not smooth but rather spiky. Additionally, we can see a sharp boundary between longer lifetimes and no incrase at all for values $\alpha = 0.25$. This boundary seems to independent on h. See section 4.3 for details.

4.4 Onset of Turbulence

A non-vanishing coupling does not necessarily have to lead to an increased lifetime, as seen in the last section. Additionally, the critical value α_{cr} seems to be vastly independent of h, as can be seen in the parameter plot 4.11. Simulations for different, fixed h and varying α near α_{cr} will now be presented in order to inspect more closely the onset behaviour.

To thate end, the same lifetime algorithm as in section 4.3 is used, but with a higher resolution of α. The data are plotted in figure 4.12.

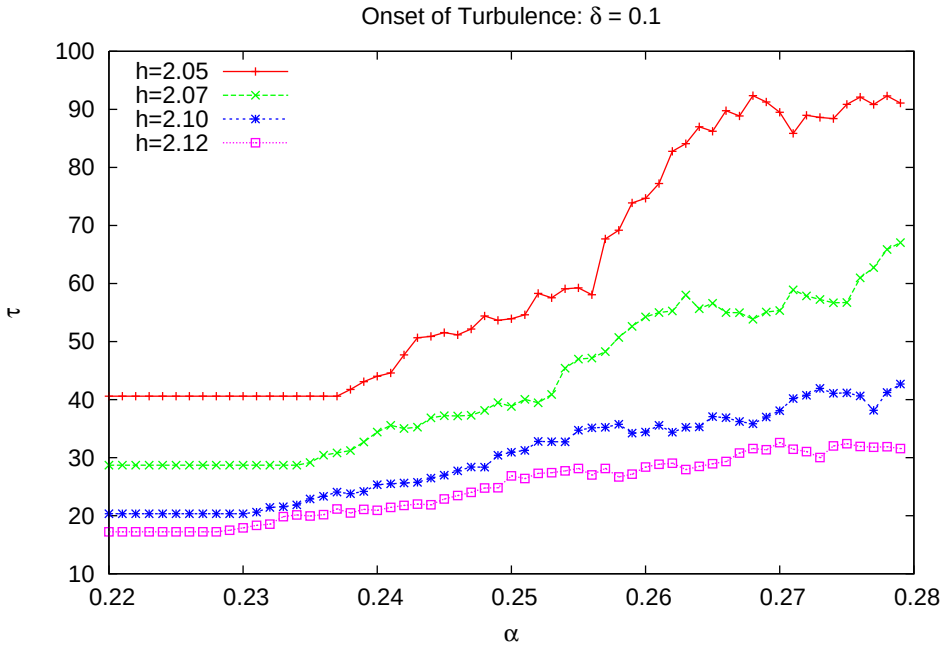

Figure 4.12: Lifetime scaling law at the onset of turbulence. Different curves belong to different values of h. With this enhanced resolution one observes that the critical coupling α_{cr}, where a first increase in the average lifetime can be determined, decreases slightly when h is increased (see text).

These data show, that α_{cr} is decreasing for increasing h. We will now answer the question, why a lifetime increase can only be seen for coupling strength substantially above zero.

The space-time plot for $\alpha = 0.2$ and $h = 2.1$ in figure 4.5 reveals, that only the first site is in a turbulent state for $\alpha < \alpha_{cr}$. The coupling is not sufficient to bring the neighbour into the chaotic region. This gives rise to the fact, that the average lifetime for $0 < \alpha < \alpha_{cr}$ is the same as the typical lifetime for a single site ($\alpha = 0$).

A necessary condition for a turbulent puff is hence a sufficiently strong positive coupling to bring the downstream neighbour into the chaotic state. To that end, a value $x \in [1+\delta, 2+\delta]$ is needed at the upstream neighbour site. Since the downstream neighbour is in the laminar state at the beginning, its dynamics is only determined by the coupling $\alpha g(x)$ from the first site.

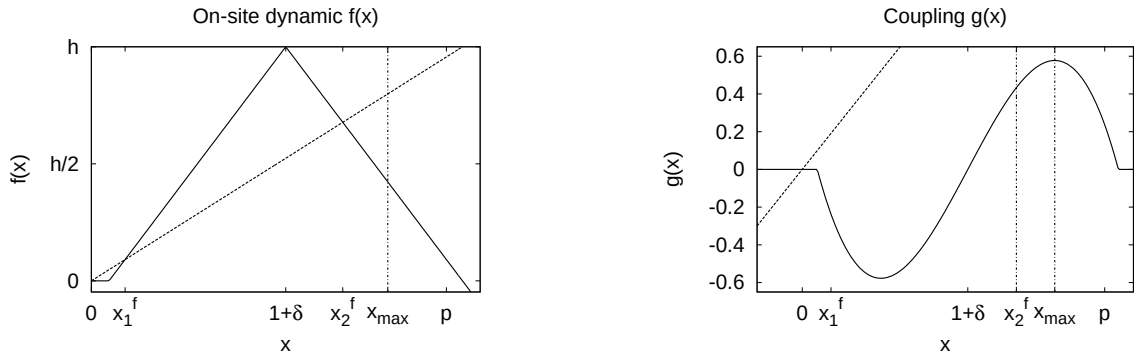

Figure 4.13: On-site dynamics f and coupling function g. See the text for the definition of interesting values.

For $\alpha < \alpha_{cr}$, the coupling is still not strong enough to kick the neighbour into the chaotic state. The lower bound on α for a transition in one step is determined by

$$\alpha g(x_{max}) = x_1^f \tag{4.4.1}$$

where x_{max} is the maximum of g (cf. figure 4.13). This yields a coupling strength of

$$\alpha = \frac{x_1^f}{g(x_{max})} \approx 0.33 \tag{4.4.2}$$

Comparing with the data in figure 4.12, these values are to large to determine α_{cr} correctly.

Therefore, a multi-step transition is needed in order to trigger a turbulent puff for small α. Since the laminar fixed point is stable, a finite kick is needed to get a memory into the system. Therefore, a kick has to be at least larger than δ, otherwise the local dynamics maps the perturbation to zero. This gives the condition

$$\alpha g(x) > \delta \tag{4.4.3}$$

But the multi-step mechanism depends crucially on the chosen x. If we choose $x \in [1+\delta, 2+\delta]$, it is likely to be mapped to values $x < 1+\delta$, where a negative coupling destroys the kick memory. The most efficient coupling is obtained for $x = x_2^f$. Although this fixed point is unstable, a trajectory starting near x_2^f will remain in the region of positiv coupling for quite some time.

These considerations can be expressed in a conjecture for the behaviour of α_{cr}

$$\alpha_{cr} g(x_2^f) = \delta \tag{4.4.4}$$

Note, that g depends on h via x_2^f. The results from the simulation are given in figure 4.14. Errorbars express the accuracy in the α grid. The theoretical expectation from (4.4.4) is given as the green curve. That the curve is not a fit. It is the complete analytical result without free parameters.

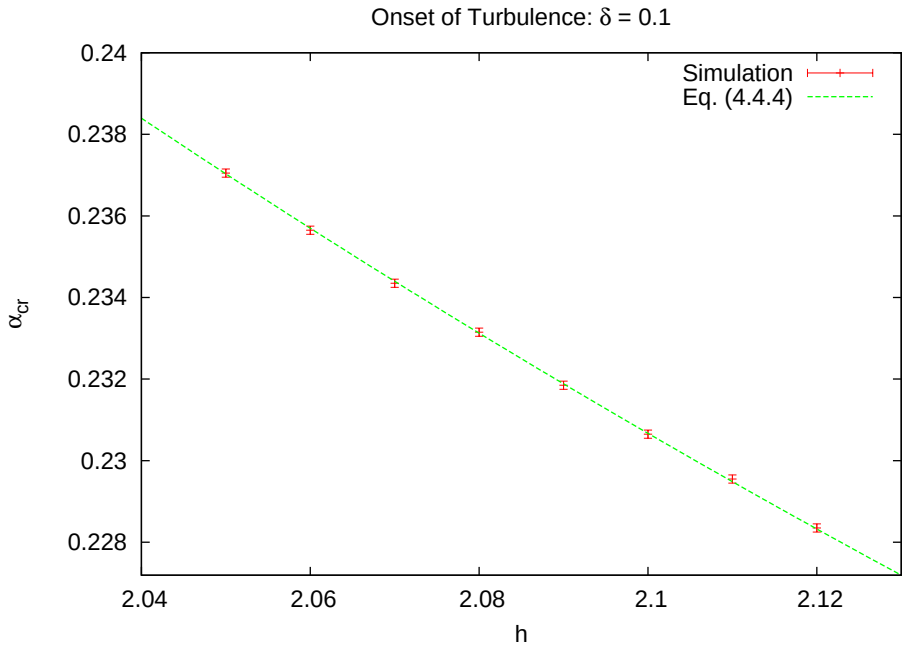

Figure 4.14: Simulation data for the onset of turbulence. The critical coupling strength α_{cr} is determined from data as shown in figure 4.12. The theory curve is the analytical prediction (4.4.4), without adjustable parameters!

The simulation data is seen to be in perfect agreement with the theoretical predicted curve. The transition to turbulence is therefore understood in our model system[2].

We further notice, that a spreading process can not be achieved by a memory-less system. Much larger coupling strength are needed in order to obtain travelling structures without memory.

This is one very fundamental result. It gives us much insight into the dynamics of our system. Since the threshold at α_{cr} is now understand, we will come to the range and velocity distributions of puffs in the next section.

4.5 Velocity Distributions and Travelled Distance

We will now turn to the investigation of the range of a turbulent puff, i.e. the overall distance travelled from nucleation to decay. Therefore, the range is zero for an immediately decaying structure. This is a first step in order to analyse velocities of the turbulent puffs. The same algorithm is used for the range computations as for the lifetime simulations. Instead of the lifetime of a puff, the covered distance until its decay is measured.

[2]The presented mechanism is not limited to our model. It seems to be a general mechanism for unidirectinal coupled systems with a super-stable fixed point. The shift δ can be denoted as a threshold for memory in the system. It is a common scheme in excitable system. This behaviour can be seen in nerve pulses, which show the same threshold behaviour before a neuron is firing and the impulse travels along the axon. In particular, the mechanism does not depend on the concrete definitions of f and g.

The same considerations as in the computation of the lifetime suggest an exponential range distribution

$$P(s) \sim \exp\left(-s/\sigma\right) \tag{4.5.1}$$

where σ is the average range for a given α and h. Again, a logarithmic plot can be used in order to determine σ (cf. figure 4.15). Simulations for fixed $h = 2.1$ and varying α

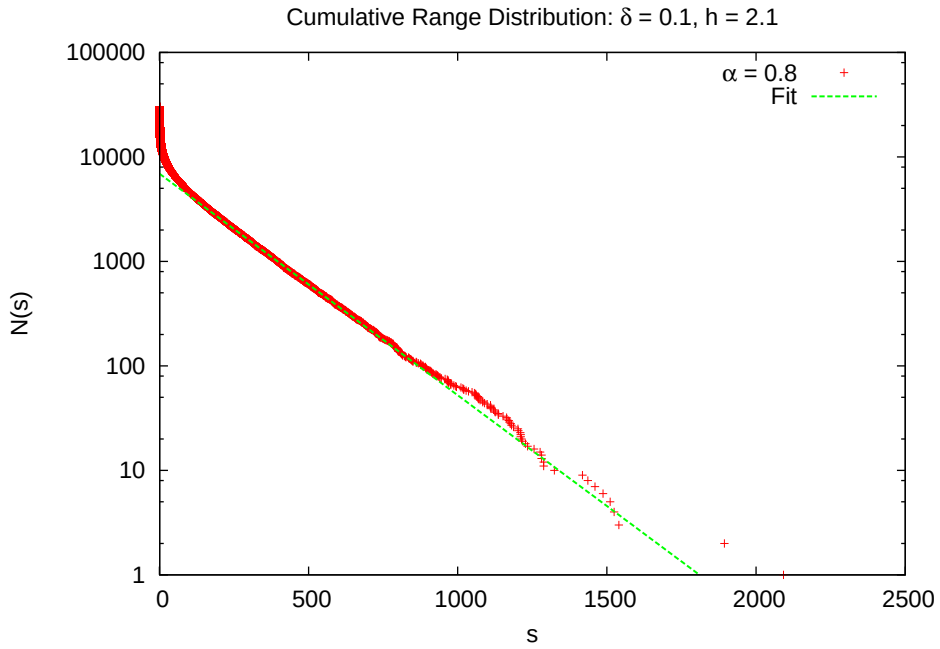

Figure 4.15: Range distribution of the uCML for coupling strength $\alpha = 0.8$.

can be used to study the scaling law $\sigma(\alpha)$. The α-dependence of τ and σ is plotted in figure 4.16.

$\sigma(\alpha)$ has the same complex structure as $\tau(\alpha)$. A remarkable aspect is the similarity between the two curves. Both scaling laws basically show the same behaviour. The onset of increased range is suitable to determine the onset of turbulence, like in the case of the average lifetime. Although, both curves look essentially the same, the two scaling laws are not simply proportional to each other. We have to take into account, that the plot is given on a log-scale. In order to show this, we plotted the ratio σ/τ in figure 4.17. The increase in the ratio supports the fact, that the scaling laws are not propotional, otherwise it should stay constant. Instead, it is increasing over the whole domain, with an intermittent regime around $\alpha \approx 0.7$. This can be explained by the spiky part of the distributions for that coupling strength.

A more interesting quantity than the range is the velocity of a puff. It can be defined by the lifetime t and range s of a turbulent puff as

$$v = \frac{s}{t} \tag{4.5.2}$$

As usually, we are not interested in velocities of single trajectories, but in the average velocity for given parameter values. It is worth mentioning, that the average lifetime τ

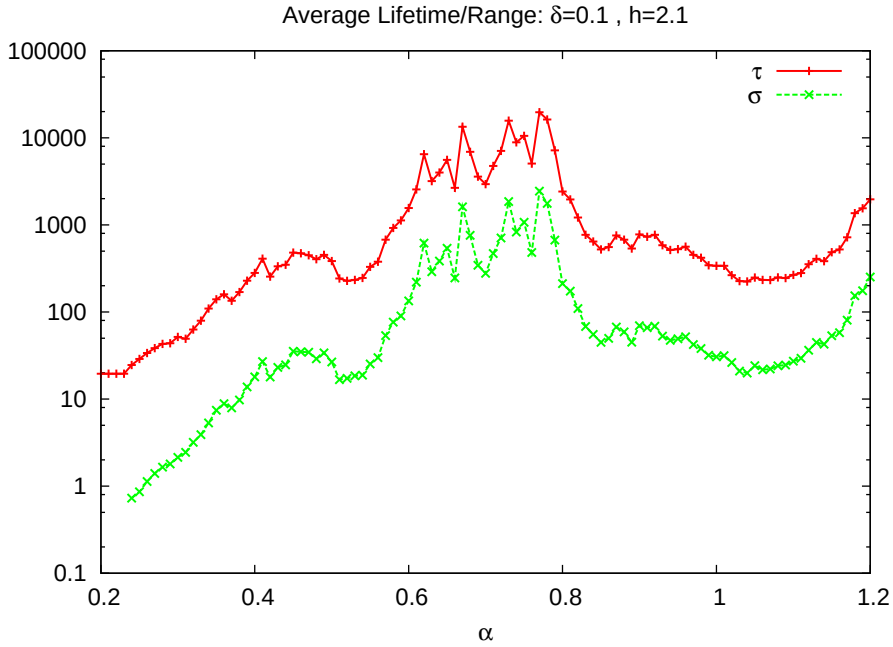

Figure 4.16: The average lifetime $\tau(\alpha)$ and range $\sigma(\alpha)$ for $h = 2.1$. For τ, the number of iteration until the decay is plotted. For σ, the values refer to the distance, a puff has travelled until its decay. Note, that the curves are very similar.

and range σ can not be used to compute the average velocity $\langle v \rangle$, since the velocity is correlated with the lifetime.

Furthermore, it is not possible to compute the average lifetime for large coupling strengths $\alpha > 1.4$ and $h = 2.1$. The lifetime is very long for those α and a simulation of a puff until its decay would take too much time. Despite this problem, one can determine the velocity of a trajectory quite easily. This is done by simulating the system for a fixed time t and measuring the largest site s, which is in a turbulent state. The ratio gives a measure for the velocity v of this puff. Actually, it measures the front velocity of the puff. Since a puff is eventually decaying, this front velocity can be used as the mean puff velocity, if the simulation time is long enough. Note, that the velocities in this section are computed for coupling strength clearly larger than $\alpha = 1.4$. In this region, the lifetime and range are so large, that they can not be computed seperately. This is already clear from figure 4.11.

In contrast to the distribution of the lifetime and the range, the distribution for the velocity is not a simple exponential function. The lifetime and range algorithm for a fixed simulation time is used to determine the velocity of a trajectory. We only took trajectories into account, which travelled at least two sites. This excludes immediatly decaying trajectories, which can not be identified as a turbulent puff.

The cumulative distribution functions for $h = 2.1$ and $\alpha = 2.5$ and 3.1, respectively, are shown in figure 4.18. It looks similar to a cdf for a Gaussian distribution. A closer look reveals however, that the cdf reaches the limiting value 1 too late, as compared to

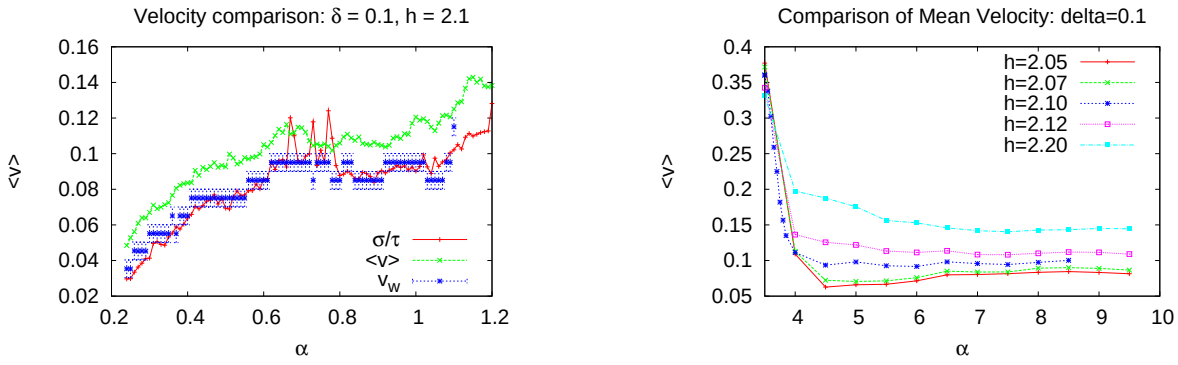

Figure 4.17: $\langle v \rangle (\alpha)$. Left: small coupling near the onset of turbulence. $\langle v \rangle$ is clearly larger than the value determined by the ratio σ/τ. The ratio rather amounts to the maximum of the velocity distribution. Right: large coupling values $\alpha > 4$. $\langle v \rangle$ is plotted for different h. In all cases, a limiting value is approached quite fast. See text for more details.

a Gaussian. A cdf for a Gaussian is given by

$$G_{\text{cdf}}(x) = \frac{1}{2}\left[1 + \text{erf}\left(\frac{x-\mu}{\sqrt{2\sigma^2}}\right)\right] \tag{4.5.3}$$

with the mean μ and the variance σ^2 (cf. [5]). A possible fit to the simulated cdf is shown in the figure. It is clearly seen, that a Gaussian approaches 1 for much smaller values of v. This suggests, that we are dealing with a heavy-tailed function.

In addition to the cdf, we computed a histogram of the velocities.

As compared to a Gaussian, the histogram has a higher probability at large velocities, when compared to a Gaussian. This states for the notation as a heavy-tailed distribution.

The average velocity can not be computed as in the lifetime and range cases above, since v has not an exponential distribution. Therefore, we take the mean value

$$\langle v \rangle = \frac{1}{N}\sum_{i=1}^{N} v_i \tag{4.5.4}$$

as an estimator for the average. A first step is to analyse the computed $\langle v \rangle$ by comparing it with the ratio σ/τ. The plot is given in figure 4.17

In addition to that, we have plotted the most probable velocity v_w, which is defined as the maximum of the distribution (cf. figure 4.19).

The average $\langle v \rangle$ is very different from σ/τ. This is what we expected from the consideration, that v is correlated with t. Another interesting aspect is that the curve for the most probable v is very similar to the ratio curve.

The great advantage in studying the velocity is, that simulations can be done even for values of the coupling strength, which are not accessable for lifetime simulations due to the very long lifetime. Figure 4.20 shows the dependence of the velocity on the coupling strength. After a slow increase for $\alpha < 1$, the average velocity stagnates at $\langle v \rangle \approx 0.1$

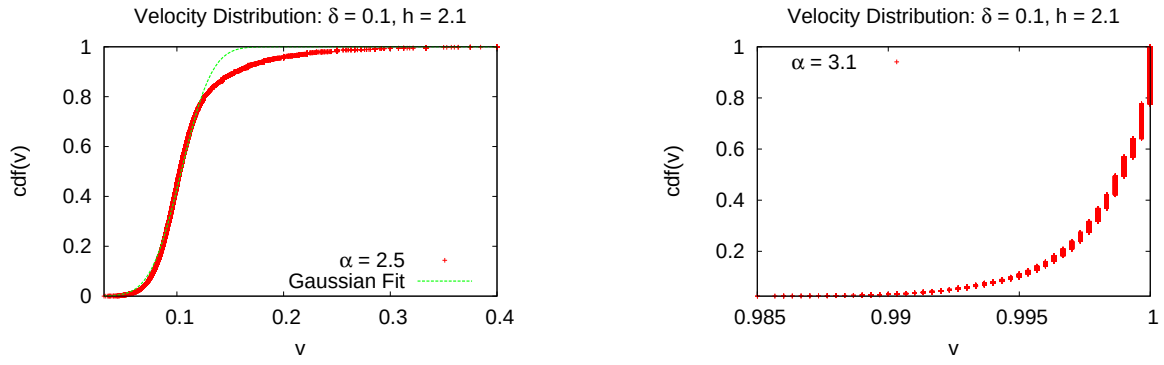

Figure 4.18: Cumulative distribution functions for the velocity for $\alpha = 2.5$ and 3.1, respectively. For $\alpha = 2.5$, the cdf has a heavy-tailed distribution as compared to a Gaussian. The fit is determined by (4.5.3) with parameters $\mu = 0.104$ and $\sigma = 0.023$. For $\alpha = 3.1$ the distribution has a steep increase at the maximal velocity of 1.

for a long range. A sharp rise is examined at $\alpha \approx 2.8$, where the front velocity nearly reaches its maximum of $\langle v \rangle = 1.0$. For further increased $\alpha > 4.0$, it falls and eventually reaches 0.1 again.

We will first check the behaviour of $\langle v \rangle$ for large α. Therefore, curves for different h are plotted in figure 4.17.

It is seen, that the average velocity reaches a finite value, which seems to be dependent on h. This behaviour is well understood by the following considerations. For large α, the coupling is so huge, that the neighbouring site is pushed beyond the chaotic region. Therefore, it decays immediately in the next step and no travelling structures can be created. The lifetime and velocity, is then determined by the lifetime of the first site. This leads to the dependence on h. The intuitive image, that for large α the coupling is more dominant than the on-site dynamics and therefore the limit of $\langle v \rangle$ would yield the same value for all h is wrong. The parameter range of $\alpha > 4$ is an unphysical range. Such a behaviour is not observed in pipe flow experiments. It is a limit of our model, that will not be investigated any further.

The most striking region is seen to be around $\alpha \approx 2.8$, where the average velocity has a very steep increase to nearly 1. This suggests a fundamental change in the dynamics of the system. A look at space-time plots reveals, that we can find a transition from a turbulent puff to a turbulent slug in this region. But for slugs, the interesting quantity is not the average velocity, but the growth. This transition will be studied in the next section.

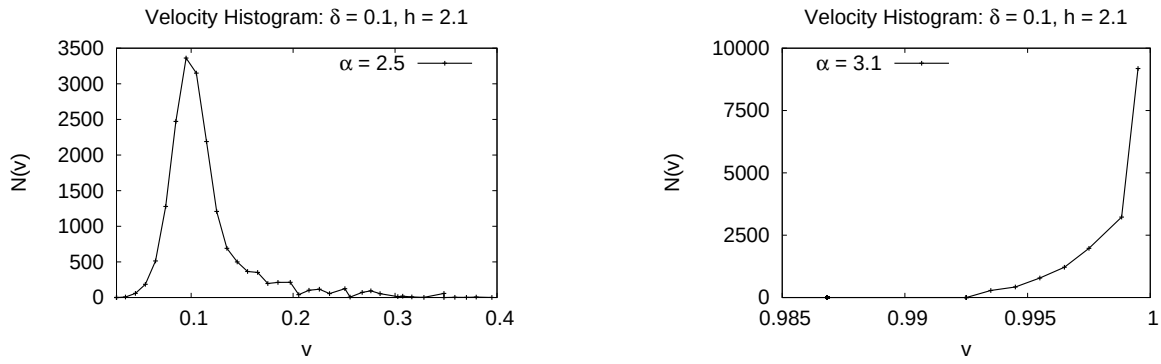

Figure 4.19: Histogram for the velocities for different coupling strengths. For $\alpha = 2.5$, the histogram has a clear maximum. The distribution has higher probability at larger values of v as compared to a Gaussian and is therefore identified as heavy-tailed. For $\alpha = 3.1$, the distribution is nearly completely centered at $v = 1$, as expected from figure 4.18.

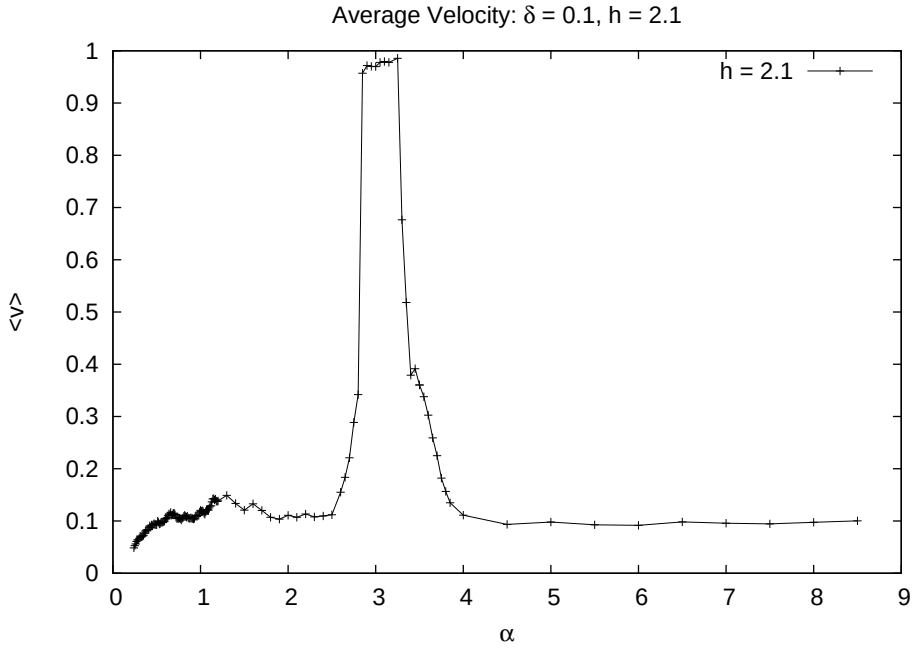

Figure 4.20: $\langle v \rangle (\alpha)$. After a slow increase to $\langle v \rangle \approx 0.1$, the ratio sharply rises to almost 1 for $2.5 \leq \alpha \leq 4$. For larger α, $\langle v \rangle$ tends again to a limiting value $\langle v \rangle \approx 0.1$.

4.6 Transition from Convective to Absolute Instability

We have already mentioned in the introduction, that a turbulent puff is a convective instability, while a slug is an absolute one. Since slugs have an infinite lifetime, it makes no sense to do simulations on average lifetimes and ranges, like we did in the case of turbulent puffs. The average front velocity is not an interesting quantity for a slug, either. Rather we concentrate on the average growth of a slug to characterise its behaviour. We will now study the dependence of the slug growth on α in our uCML model.

The growth G for a trajectory is defined as the time derivative of the width w of the turbulent region

$$G := \frac{\mathrm{d}w}{\mathrm{d}t} = v - b \tag{4.6.1}$$

It can also be calculated by the difference between front v and back velocity b, since the width is given as $w = r_f - r_b$, where r denotes the front and back site, respectively. Further, we assume, that G is constant after a transient time. A simulation of constant time can be done. G is determined by the width at the end of the simulation. The simulation time has been chosen to be 1000 time steps, while $N = 22.000$ initial perturbations where taken into account. The distribution from the simulations are shown in figure 4.21 for different α. The distribution has a non-trivial form for $\alpha < 2.8$. Therefore, the average can only be determined by

$$\langle G \rangle = \frac{1}{N} \sum_{i=1}^{N} G_i \tag{4.6.2}$$

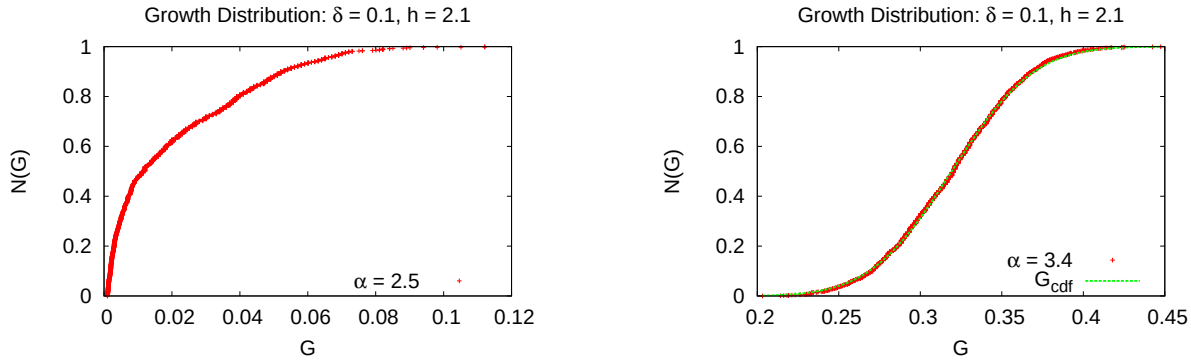

Figure 4.21: Cumulative distribution functions for the growth. For $\alpha = 2.5$, the distribution is not a simple exponential or Gaussian shape. But for $\alpha = 3.4$ the behaviour changes dramatically and the distribution can be described by a Gaussian with $\mu = 0.319$ and $\sigma = 0.039$.

The cdf changes dramatically in shape for $\alpha \approx 2.8$. This distribution can be identified with a Gaussian distribution. The fit in 4.21 is the function (4.5.3) for the cdf of a Gaussian. This fundamental change in shape has to be related to a special parameter value, which has to be determined by some change in the dynamics of the system. First, we will have a look at the scaling law $\langle G \rangle (\alpha)$. It is plotted in figure 4.22.

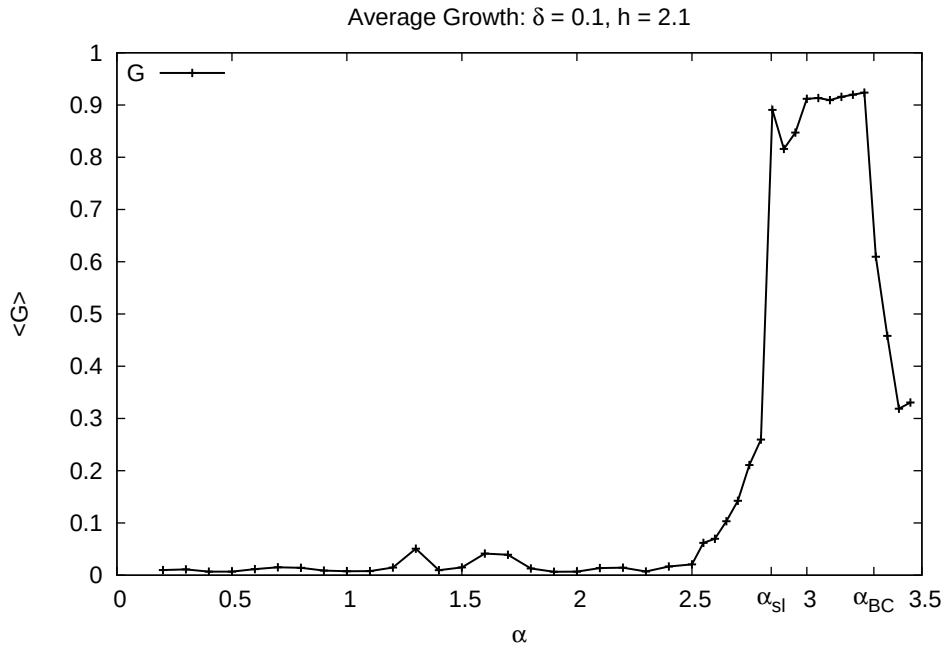

Figure 4.22: The average growth of the turbulent region. A strong increase is seen to be at α_{sl}, where the slug regime sets in. A decrease at $\alpha \approx 3.3$ determines the end of the slug regime. See the text for further explanations.

Within the error margins the growth is zero as long as $\alpha \lesssim 2.5$. This is quite obvious from the space-time plots, since we are in the turbulent puff regime. Puffs are eventually decaying and therefore have a growth of zero. The strong increase in growth for $\alpha = 2.8$ is what we had expected from the study of the average velocity from the last section. The qualitative change in shape of the distributions is at this special parameter value, too. Before analysing the mechanism for the large increase in growth, we will shortly have a look at the velocity of the back.

Since $\langle G \rangle$ and $\langle v \rangle$ are known, the α-dependence for the propagating back $\langle b \rangle$ can be computed. According to (4.6.1), it is given by

$$\langle b \rangle = \langle v \rangle - \langle G \rangle \tag{4.6.3}$$

The plot is given in figure 4.23. The back is not always propagating with the same average velocity, as could be expected. Therefore, there seems to be some correlation between the coupling strength and the lifetime of the back. The back velocity is not a very interesting quantity in experiments. Since puffs are structures of constant size, the back and front velocity are the same. Therefore, the growth is zero. This has also been observed in the simulations (cf. figure 4.22). But it is also seen in the plot, that the back velocity is not changing very much at the slug transition, while the front velocity is greatly increased (cf. figure 4.20).

The strong growth at α_{sl} is pointing to a very effective coupling. If a value x_* is mapped by the coupling to the same value x_* at the next site, which has been laminar before, a ballistic spreading is observed. This leads to the condition

$$\alpha_{sl} g(x) = x \tag{4.6.4}$$

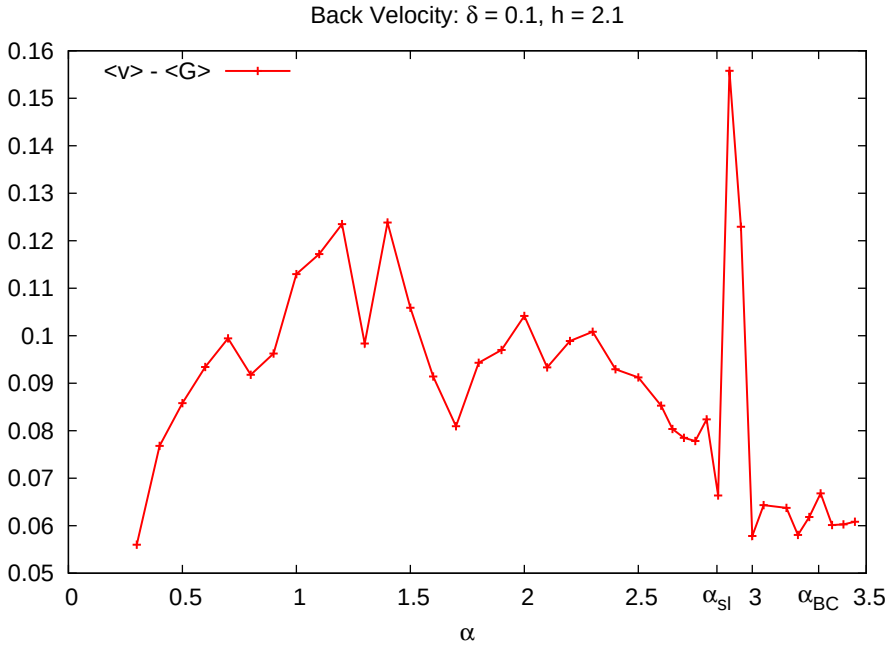

Figure 4.23: Average back velocity for $h = 2.1$. The curve is determined by (4.6.3).

for the slug transition at α_{sl}. Equation (4.6.4) can be identified as a fixed point equation for the coupling. Therefore, we will now analyse the bifurcation diagram for αg (cf. figure 4.24).

As we can see in this figure, the bifurcation diagram is qualitatively the same as that of the logistic map in (2.2.2). The first parameter value, where a fixed point occurs, is determined to be $\alpha = 2.845$. This is exactly the parameter value, where the growth reaches its maximum. Another interesting aspect is the boundary crisis at $\alpha \approx 3.3 =: \alpha_{BC}$. This, again, is exactly the point, where the average growth has a strong decrease. The range of large growth is therefore completely understood via the bifurcation scenario of αg.

If our presented mechanism is correct, we would expect, that the strong increase at α_{sl} and the decrease at α_{BC} is independent of h. Simulations for different values of h have been performed (cf. figure 4.25) and they indeed reveal, that those critical values do not depend on h up to the numerical accuracy.

The transition from the puff to the slug regime is now completely understood from the point of our model.

This noticable result will finish this chapter. A discussion on some results of our model system will now be discussed in the next chapter.

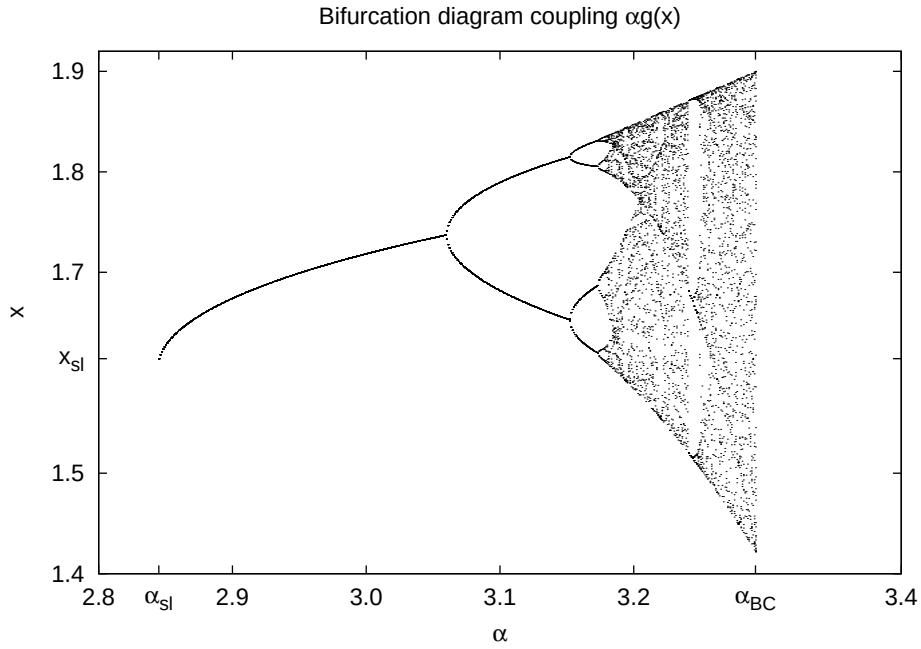

Figure 4.24: Bifurcation diagram for the coupling αg. The coupling strength is used as the bifurcation parameter. A saddle-node bifurcation is happening at $\alpha_{sl} \simeq 2.845$ and $x_{sl} \simeq 1.614$.

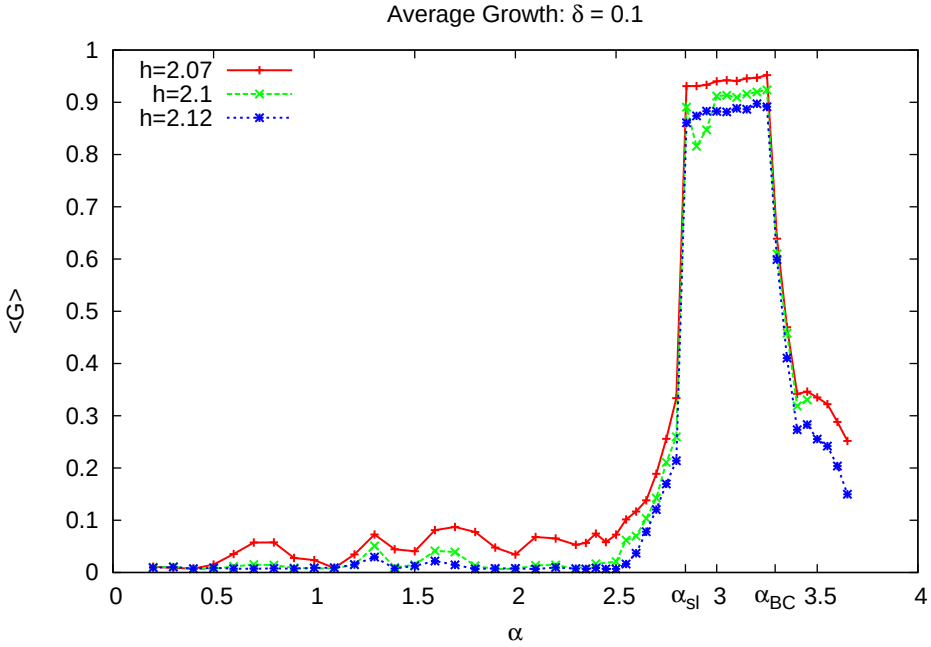

Figure 4.25: Comparison of the average growth for different h. As expected from the theory, the onset α_{sl} is independend of h.

Chapter 5

Conclusion

We will now come to the conclusion of this work. Most aspects of the system have also been described in the corresponding chapters. Here, we will give a little discussion on the relevance of the results for real pipe flow and an oulook for future work afterwards.

5.1 Discussion

The results will now be interpreted with regard to real experiments. First, there is one obvious difference to real pipes. In incompressible pipe flow, the only control parameter is the Reynolds number. Instead, the presented model has three parameters. These are the coupling strength α, the height h of the tent map and δ, which has been fixed for this work. This is an advantage of our system, since we have many knobs to tune. The stability of the laminar fixed point is controlled by δ. The spatial coupling can be tuned by α and the local instability is determined by h. Therefore, it is possible to separate effects that stem from different properties of the system. This is a great advantage comparing to pipe experiments, where e.g. the stability of the laminar flow can not be influenced independently of the local stability.

We will now focus on several aspects and highlight them in relation to real pipe flow.

5.1.1 Edge of Chaos

One important results of this work is related to the onset of turbulence. It has been shown, that the critical value α_{cr} can be defined by simple arguments (cf. section 4.4) as

$$\alpha_{cr} := \frac{\delta}{g(x_2^f)} \tag{5.1.1}$$

The verification has been demonstrated in figure 4.14.

No fit parameters are left in this condition, such that the simulation data is exactly lying on the theoretical predicted curve. The understanding of α_{cr} is a crucial point in the analysis of the system. It determines the boundary between the laminar and turbulent region. There are no more open questions about that transition point from

the modelling point of view. Here, δ is a measure for the stability of the laminar fixed point, while x_2^f has been verified as an optimal coupling state.

This observation is called the double-treshold of turbulent flow [31]. A large Reynolds number is not sufficient in order to trigger turbulence, if the perturbation amplitude is too small. On the other hand, a large perturbation will also not lead to turbulence, if the Reynolds number is not high enough. This threshold mechanism is also observed in our model. For couplings smaller than α_{cr}, no perturbation will lead to turbulence. Even for $\alpha > \alpha_{cr}$ not every perturbation will lead to a turbulent flow. One needs at least a perturbation of size δ in order to trigger turbulence. This is a nice relation to the double-treshold, observed in real experiments [14].

In real experiments, the boundary between the laminar and the turbulent region is called the edge of chaos. It separates states that decay immediately from those which become turbulent. The idea is to identify states on the edge, which are both entrance and exit into or from the turbulent region, respectively. This is fundamentally different in the model. The entrance state is determined to be x_2^f. But this special state has nothing to do with the escape from the turbulent region. Completely different states can occur at the decaying state of a turbulent puff in the model. This is one difference to real experiments.

5.1.2 Heavy-Tailed Velocity Distributions

The distributions for the lifetime and the range have been predicted from simple arguments. This is not possible for velocitiy distributions. The velocity $v = \frac{s}{t}$ is a ratio of two non-independent random variables. It is not even simple to determine the average $\langle v \rangle$ from a special point of the distributions. It is not clear, if s is independent of $1/t$. Additionally, $\langle 1/t \rangle$ is not existing, if t has an exponential distribution. This can also be seen in figure 4.17, where $\langle v \rangle$ is obviously different from σ/τ. Further, the distributions for the velocities are heavy-tailed, possibly due to a correlation between the average lifetime and range. There is a higher probability to find faster puffs, relative to a normal distribution. This fact can also be verified in the histograms of the velocity in figure 4.19. From those plots, the most probable velocity v_w can be determined as the maximum of the distribution. Interestingly, these values are fitting the ratio σ/τ very well. This is clear, since τ is the expected lifetime and σ the expacted range, which yields a most probable v_w. That σ/τ does not describe $\langle v \rangle$ is due to the heavy-tailed nature of the distributions. If v would be a normal distributed random variable, $\langle v \rangle$ and v_w would describe the same value. The velocity distributions for turbulent puffs are very narrow in real experiments. Most of the triggered puffs travel more or less with the same speed. The arise of heavy-tailed distributions near the transition to slugs can be a guide to experiments to check this prediction of the model. By understanding the heavy-tailed nature of the distributions, one could gain more information about the transition mechanism from puffs to slugs.

5.2 Summary

As a little reminder, we will shortly sum up the results from our studies.

5.2.1 Mean-Field Model

We have introduced a 2d model system with a fractal basin boundary and a boundary crisis. The crictical parameter for the boundary crisis has been computed analytically. Several simulation runs verified the super-exponential scaling law of the average lifetime of transients. Additionally, an algorithm for tracking the edge of chaos has been presented, which could track the edge of chaos with a very high spatial accuracy. These data suggests, that the edge of chaos is a fractal structure.

5.2.2 uCML

After introducing the model, we have given some space-time plots to get an idea about the trajectories of the system. A first look revealed the existence of convective and absolute instabilites. First, the exponential lifetime distributions have been verified and the average lifetime τ has been computed for several parameter values α and h. The scaling law $\tau(h)$ for $\alpha = 0$ has been theoretically predicted as a 1/log law, which has been verified by the simulations. Further, the superexponential scaling for $\alpha > \alpha_{cr}$ has also been verified by a fit. The complex structure of $\tau(\alpha)$ has been determined as well and a complete parameter space plot has been given as a false-color plot. A closer look revealed a α dependence of the onset of turbulence. The critical parameter α_{cr} at the onset has been predicted and verified by theory and simulation, respectively. The following investigation of range and velocity dsitributions revealed, that the range has no more information than the lifetime. Despite, the velocity shows a heavy-tailed distribution at the slug transition treshold. As a useful quantity for the slug characteristics, the average growth of slugs depending on α has been studied. The critical point for the slug transition, i.e. α_{sl}, has been predicted by theory as a point where a saddle-node bifurcation is happening. This has also been verified in the simulations. The investigation of the average back velocity showed, that it stays at rather small values for all α. Therefore, the slug transition has been identified to be crucially dependent on the front velocity.

5.3 Outlook

There are much more interesting questions, that can be answered by further studies of the model. We will present some of them in this section.

5.3.1 Scaling after α_{cr}

An increase of the average lifetime is not observed for $\alpha < \alpha_{cr}$. After studying the onset region in a high accuracy plot the onset mechanism has been presented. The threshold

has been predicted analytically. It obeys the law

$$\alpha_{cr} g(x_2^f) = \delta \tag{5.3.1}$$

This conjecture has been verified by the simulation data, which are in perfect agreement with the predicted values (cf. figure 4.14).

Although, the critical point α_{cr} has been understood, the scaling of τ with α after this point needs further investigation. By normalising the lifetime $\tau(\alpha - \alpha_{cr})$ with the single site lifetime τ_0, the corresponding double-logarithmic plot near the onset suggest a power law scaling (cf. figure 5.1). One possible line is given with a slope of 30. It is worth noticing, that the possible fit line is similar for different values of h, which states a universal scaling law. A detailed study on this scaling would help to understand the mechanism of lifetime increase and is therefore a good starting point for further investigation.

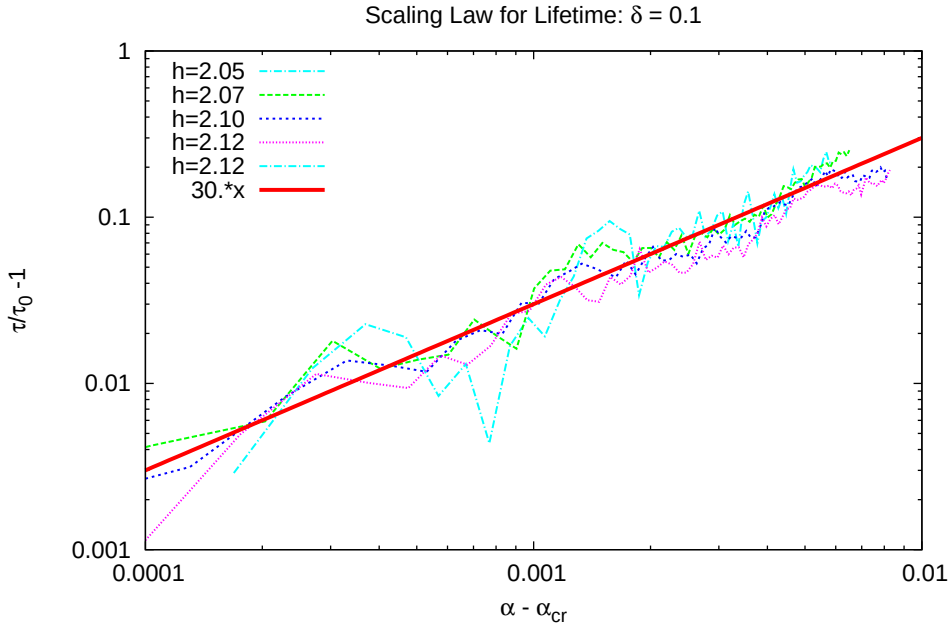

Figure 5.1: Log-Log plot of the scaling law of τ. Lifetime is normalised by the single site lifetime τ_0 and shifted by -1 to obtain a straight line through the origin.

5.3.2 Percolation Theory

A theoretical aspect, that needs further investigation, is to have a look at the puffs in a comoving frame of reference. A space-time plot is shown in figure 5.2.

The front velocity v has been used in order to define the comoving frame

$$s = s_0 - v \cdot t \tag{5.3.2}$$

This plot looks like a structure, that could be related to a problem of directed percolation (cf. [35]).

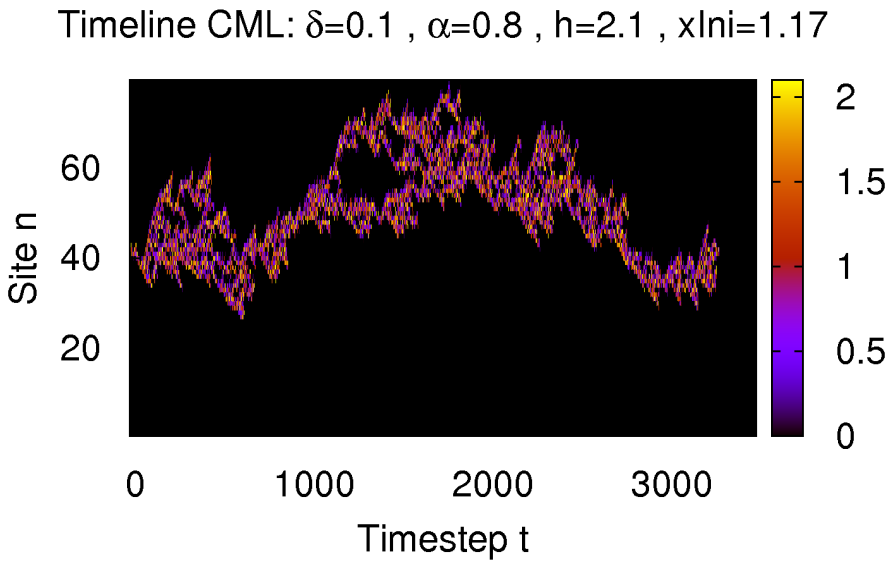

Figure 5.2: Comoving frame of a turbulent puff. The average front velocity has been used as the transformation velocity. Growth and splitting events can easily be detected in the comoving frame.

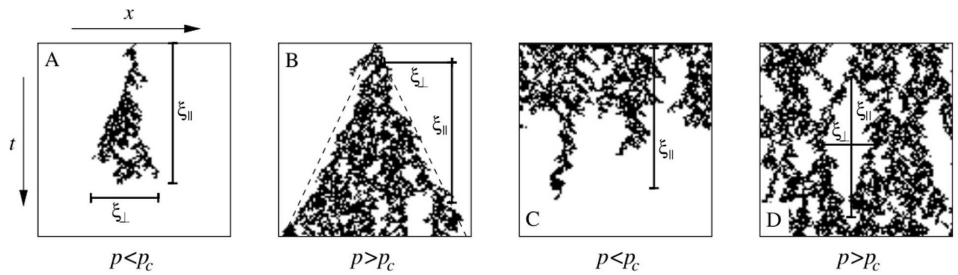

Figure 5.3: Directed percolation schemes. The left two images are for a single seed perturbation, while the right ones are for many perturbed sites. $\xi_\perp$ and $\xi_\parallel$ are the space and time correlation lengths, respectively. Reprint from [15].

Directed percolation makes a statement about the transition point from finite structures, i.e. puffs, to infinite, percolating structures, i.e. slugs. By analysing the simulation data with respect to this percolation threshold, one would be able to understand the puff-slug transition point from a different perspective.

Additionally, the growth of slugs could be predicted just above the percolation threshold. According to [15], the slopes of slugs (cf. figure 5.3) would have an algebraical scaling law near the percolation threshold. This has to be checked in simulations or experiments in the future.

Further, splitting events can maybe described by directed percolation processes. As seen in figure 5.2, a puff or slug is not completely turbulent over its whole width. It has some holes in it, arising, if a front is faster than the rest. The two pieces can then merge again or decay. This leads to characteristic sizes of the holes, which could have a useful scaling law, when one is near a transition point. Again, further studies are needed to check these predictions from percolation theory.

Puff splitting events have been studied by MOXEY and BARKLEY [32]. They simulated the incompressible Navier-Stokes equations and analysed the results in terms of directed percolation. They state, that the transition from puffs to slugs happens via spatio-temporal intermittency. This transition can lead to infinite lifetime, if it is identified with the percolation threshold. According to [32], the transition from puffs to slugs can not be solved by lifetime measurements. Since, lifetimes grow exponentially, they suggest to study the qualitative change in behaviour, like in the arise of spatio-temporal intermittency.

5.3.3 Intermittency Transition before α_{sl}

The growth has ben studied in order to characterise the slug regime. The transition from puffs to slugs is characterised by the huge increase in growth at $\alpha_{sl} = 2.845$. It has been shown, that the slug regime can completely be explained by the bifurcation scenario of the coupling αg. α_{sl} can be seen as a critical coupling strength. Turbulence is always persistent above α_{sl}. Even in real experiments, there is a Reynolds number Re_{sl}, above which only slugs can be observed. For $\alpha \lesssim \alpha_{sl}$ the growth starts to increase (cf. figure 4.22). This increase seems to be reminiscent to an intermittency scenario. Although, there is no fixed point of αg for $\alpha < \alpha_{sl}$, a narrow tunnel in phase space is existing just before the saddle-node bifurcation. Therefore, the system can stay most of the time in a region of effective coupling. This leads to time periods, where the front is propagating ballistically, which are intermittent with periods of slow velocity v_0. The probability to be in the ballistic state is then related to the coupling strength α.

Therefore, it will be possible to determine the increase of growth with α from the model. This increase can be another theoretical prediction, which is not depending on any fit parameters. Additionally, the hypothesis of an intermittency transition can be checked in experiments. The theoretical and experimental understanding can therefore shed new light on the transition from puffs to slugs.

5.3.4 Re Quenching

The control of turbulence in pipe flow is very important in engineering problems. By lowering the Reynolds number in the turbulent regime, it is possible to recover laminar flow. This state could remain stable, even after increasing Re again. That could be a possibility to effectively reduce turbulence in pipe flow and is known as Re quenching. Therefore, another way to study the system is to vary the parameters α and h, while a simulation is running. This has also been done in [32] and can reveal parameter values, where a turbulent state goes back to laminar flow. A good point to start is in studying lifetimes and decay modes for continuously varying parameters. Interesting questions are for example:

- Is the lifetime of puffs influenced by lowering α for a short period of time ?
- Which decay scenarios arise near the threshold α_{cr} ?
- Are there special modes, that are more likely to decay ?
- Are there structures, that, once obtained, keep their long lifetime even for smaller α due to self-preserving effects ?

As it is obviously seen in this list, there is still a lot of work to do. But some questions have been answered in this thesis, both theoretically and numerically. Beyond the insight in turbulent pipe flow, uCMLs also have considerable interest from a dynamical systems point of view. Coupled map lattices have been studied for quite some time. But most of the obtained results are limited to the case of diffusively coupled lattices [10, 22, 37] or a global coupling [21]. Unidirectioal coupled map lattices have been investigated in [40, 41, 49]. But this is the first time, were a unidirectional coupling has been used in order to study turbulent puffs and the transition from convective to absolute instabilities. To our knowledge, this is also the first time, where such a model has been studied to this extent. It is remarkable, that so many theoretical predictions can be made. It is worth noticing, that most of the results have been determined without containing any free parameters.

The author is confident, that future studies on these coupled map lattices will reveal further insight.

Appendix

This appendix will give more technical questions for readers, who want to work with this model themselves.

As mentioned above, it is not clear, where the spiky region around $\alpha = 0.7$ and $h = 2.1$ in the lifetime scaling law comes from. This also seems to be related to a special dynamic in the system, since the 'hump' is vanishing for larger h (cf. figure 5.5).

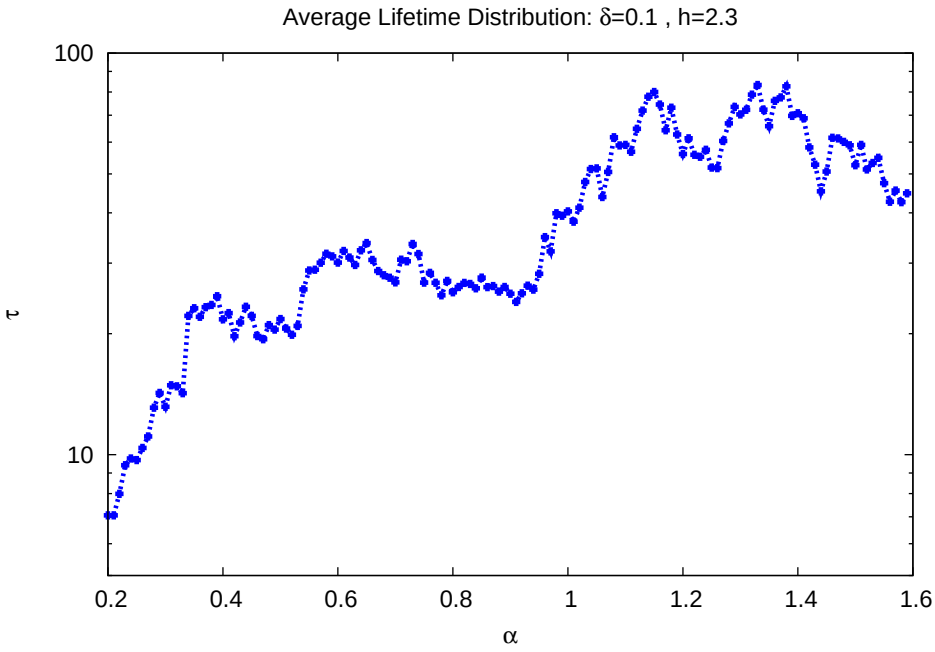

Figure 5.4: Scaling law $\tau(\alpha)$ for $h = 2.3$. The hump around $\alpha \approx 0.7$ has vanished. This has been expected from the parameter space plot 4.11.

In addition, the parameter plot shows, that the hump at $\alpha = 0.7$ is vanishing for large h, while the one at $\alpha = 1.3$ is still present at least up to $h = 2.5$. This behaviour is a good starting point in order to get further insight into the dynamics of the system.

Further, it has not been studied, how the shape of the perturbation influences the evolution of turbulent puffs. Instead of perturbing one site, one could imagine to trigger turbulence in many adjacent sites. These investigations could be done with the existing algorithm without much effort. That point has been skipped, because a great change in the behaviour is not expected. Turbulent puffs reach several sites very fast. This leads to

a rapid deletion of the memory of the intial conditions. This assumption demonstrates in the consideration, that the lifetime of a turbulent puff is independent of its age.

Another interesting point is the distribution of states x_n^i. The analysis can be done very easily by storing these values and applying the histogram algorithm also used to determine the velocity histograms.

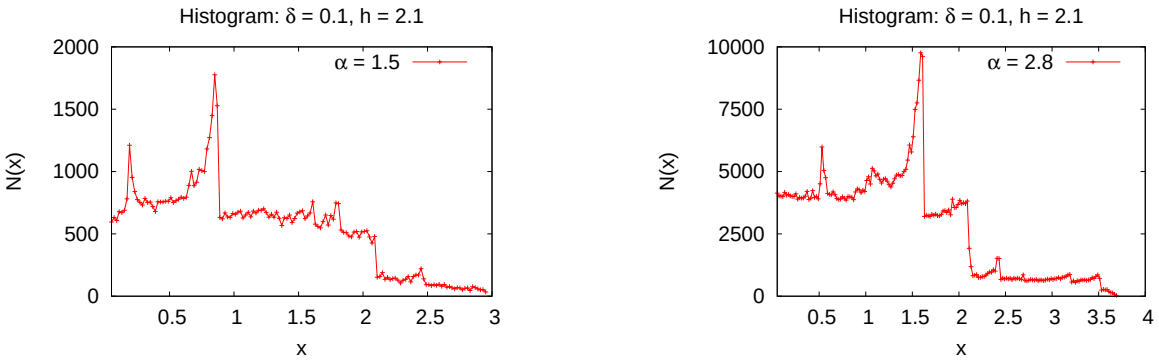

Figure 5.5: Histograms for the distribution of state variables. A characteristic value is observed as a peak in the histogram. It shifts to the right for larger coupling strength α. Even the width is increased, since the coupling αg can add a larger value to the next site.

This gives us some insight in the occurence of special values x_n^i and could be a good starting point in order to understand the spiky part of the lifetime scaling law and typical behaviour of the system. A related quantity is the distribution of the values x_n^i at the front, where the downstream neighbour is still laminar. These plots could show how turbulence sets in. If it is triggered over a wide range of values or if it is basically spread by only several state values x_n^i of the upstream neighbour.

A further possibility to analyse the system is the use of return maps. In return maps, states x_{n+1} are plotted against x_n. One return map is shown in figure 5.6.

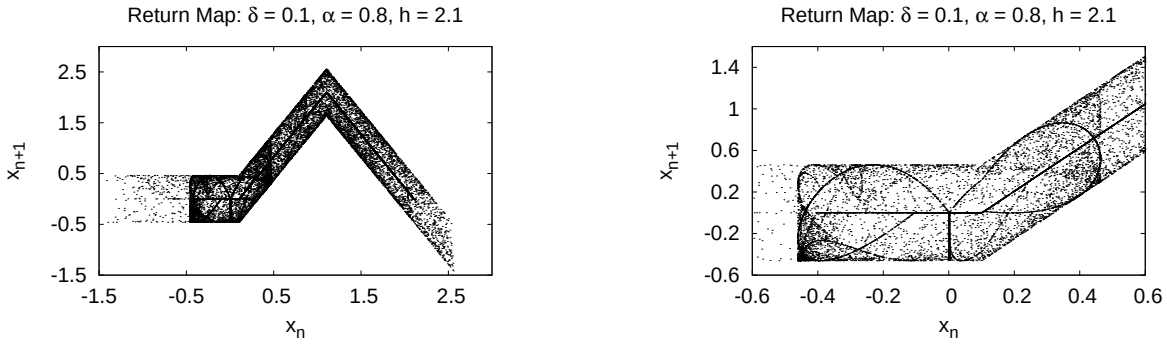

Figure 5.6: Left: Return map for the uCML for $\alpha = 0.8$ and $h = 2.1$. Right: Magnification of the region near $x = 0$. Note the dark regions, which must be related to caustics in the dynamics.

The tent shape of the local dynamic f is clearly visible in the plot. The coupling αg widens the structure, since more possible next states are available. In addition, a denser

region at the boundaries of the return maps is observed. This stems from the extremal values of g. The slope at those points is zero. Therefore, the probability to gain such a value is much higher than at the steepest parts. A magnification of the region for small x_n reveals an even more complex structure. The origin of these structures is not clear at this point, but it could be related to the evolution of fixed point or other invariant subsets. In any case, an understanding of these curves could give further insight in topological aspects of the model.

A small additional task would be to determine the invariant densities for f and αg for different parameter values. This quantity is known for the tent map with $h = 2$ (cf. [33]). But it would also be of interest to know it for the coupling αg, especially at the slug transition $\alpha = \alpha_{sl}$.

Bibliography

[1] D. J. Acheson. *Elementary Fluid Dynamics*. Oxford University Press, 1990.

[2] V.I. Arnold. *Catastrophe Theory*. Springer, 1992.

[3] J.-R. Chazottes and B. Fernandez. *Dynamics of coupled map lattices and of related spatially extended systems*. Springer, 2004.

[4] J. P. Crutchfield and K. Kaneko. Are attractors relevant to turbulence? *Phys. Rev. Lett.*, 60(26):2715–2718, 1988.

[5] H. Dehling and B. Haupt. *Einführung in die Wahrscheinlichkeitstheorie und Statistik*. Springer, 2004.

[6] R. L. Devaney. *An Introduction to Chaotic Dynamical Systems*. Westview Press, 2003.

[7] B. Eckhardt and A. Mersmann. Transition to turbulence in a shear flow. *Phys. Rev. E*, 60(1):509–517, 1999.

[8] H. Faisst and B. Eckhardt. Sensitive dependence on initial conditions in transition to turbulence in pipe flow. *Journal of Fluid Mechanics*, 504:343–352, 2004.

[9] M. J. Feigenbaum. Universal behaviour in nonlinear systems. *Los Alamos Science*, 1:4, 1984.

[10] F. Ginelli, P. Poggi, A. Turchi, H. Chaté, R. Livi, and A. Politi. Characterizing dynamics with covariant lyapunov vectors. *Phys. Rev. Lett.*, 99(13):130601, Sep 2007.

[11] N. Goldenfeld. Roughness-induced critical phenomena in a turbulent flow. *Phys. Rev. Lett.*, 96(4):044503, 2006.

[12] C. Grebogi, E. Ott, and J.A. Yorke. Fractal basin boundaries, long-lived chaotic transients and unstable-unstable pair bifurcation. *Phys. Rev. Lett.*, 50(13):935, 1983.

[13] C. Grebogi, E. Ott, and J.A. Yorke. Critical exponent of chaotic transients in nonlinear dynamical systems. *Phys. Rev. Lett.*, 57(11):1284, 1986.

[14] S. Grossmann. The onset of shear flow turbulence. *Rev. Mod. Phys.*, 72(2):603–618, 2000.

[15] H. Hinrichsen. Non-equilibrium critical phenomena and phase transitions into absorbing states. *Advances in Physics*, 49:815–958, 2000.

[16] B. Hof, A. de Lozar, D. J. Kuik, and J. Westerweel. Repeller or attractor? selecting the dynamical model for the onset of turbulence in pipe flow. *Phys. Rev. Lett.*, 101(21):214501, 2008.

[17] B. Hof, A. Juel, and T. Mullin. Scaling of the turbulence transition threshold in a pipe. *Phys. Rev. Lett.*, 91(24):244502, 2003.

[18] B. Hof, J. Westerweel, T. M. Schneider, and B. Eckhardt. Finite lifetime of turbulence in shear flows. *Nature*, 443, 2006.

[19] P. Holmes and E. T. Shea-Brown. Stability. *Scholarpedia*, 1(10):1838, 2006.

[20] Clay Mathematics Institute. `http://www.claymath.org/millennium/`. Website.

[21] W. Just. Bifurcations in globally coupled map lattices. *Journal of Statistical Physics*, 79(1-2):429–449, April 1995.

[22] E. Katzav and L. F. Cugliandolo. Coupled logistic maps and non-linear differential equations. *ArXiv Condensed Matter e-prints*, December 2005.

[23] R. R. Kerswell. Recent progress in understanding the transition to turbulence in a pipe. *Nonlinearity*, 18(6):R17, 2005.

[24] Y.-C. Lai and R. L. Winslow. Geometric properties of the chaotic saddle responsible for supertransients in spatiotemporal chaotic systems. *Phys. Rev. Lett.*, 74(26):5208–5211, Jun 1995.

[25] B. B. Mandelbrot. Fractal aspects of the iteration of $z \to \lambda(1-z)$ for complex λ and z. *Annals of the New York Academy of Sciences*, 357:249–59, 1980.

[26] B. B. Mandelbrot. The fractal geometry of nature. 1983.

[27] P. Manneville. *Dissipative Structures and Weak Turbulence*. Perspectives in Physics, 1990.

[28] Mohammad Mehrafarin and Nima Pourtolami. Intermittency and rough-pipe turbulence. *Phys. Rev. E*, 77(5):055304, 2008.

[29] A. Meseguer and F. Mellibovsky. On a solenoidal fourier-chebyshev spectral method for stability analysis of the hagen-poiseuille flow. *Applied Numerical Mathematics*, 57(8):920 – 938, 2007.

[30] A. Meseguer and L. N. Trefethen. Linearized pipe flow to reynolds number 10^7. *Journal of Computational Physics*, 186(1):178 – 197, 2003.

[31] J. Moehlis, H. Faisst, and B. Eckhardt. A low-dimensional model for turbulent shear flows. *New Journal of Physics*, 6(1):56, 2004.

[32] D. Moxey and D. Barkley. Distinct large-scale turbulent-laminar states in transitional pipe flow. *Proceedings of the National Academy of Sciences*, 107(18):8091–8096, 2010.

[33] E. Ott. *Chaos in Dynamical Systems*. Cambridge University Press, 2002.

[34] W. Pfenniger. *Transition in the inlet length of tubes at high Reynolds numbers. In Boundary layer and flow control*. NY Pergamon, 1961.

[35] Y. Pomeau. Front motion, metastability and subcritical bifurcations in hydrodynamics. *Physica D: Nonlinear Phenomena*, 23(1-3):3 – 11, 1986.

[36] Y. Pomeau and P. Manneville. Intermittent transition to turbulence in dissipative dynamical systems. *Commun. Math. Phys.*, 74:189, 1980.

[37] C. Primo, M.A. Rodriguez, J.M. Lopez, and I. Szendro. Dynamic Scaling of Bred Vectors in Chaotic Extended Systems. *ArXiv Nonlinear Sciences e-prints*, November 2003.

[38] Lord Rayleigh. On convection currents in a horizontal layer of fluid, when the higher temperature is on the under side. *Phil. Mag.*, 32:529–46, 1916.

[39] O. Reynolds. An experimental investigation of the circumstances which determine whether the motion of water shall be direct or sinuous, and of the law of resistance in parallel channels. *Phil. Trans. R. Soc. Lond.*, 174:935, 1883.

[40] O. Rudzick and A. Pikovsky. Unidirectionally coupled map lattice as a model for open flow systems. *Phys. Rev. E*, 54(5):5107–5115, Nov 1996.

[41] O. Rudzick, A. Pikovsky, C. Scheffczyk, and J. Kurths. Dynamics of chaos-order interface in coupled map lattices. *Physica D: Nonlinear Phenomena*, 103(1-4):330 – 347, 1997. Lattice Dynamics.

[42] T. M. Schneider, B. Eckhardt, and J. Vollmer. Statistical analysis of coherent structures in transitional pipe flow. *Phys. Rev. E*, 75(6):066313, 2007.

[43] J. T. Stuart. Taylor-vortex flow: A dynamical system. *SIAM Review*, 28(3):315–342, 1986.

[44] G. I. Taylor. Stability of a viscous liquid contained between two rotating cylinders. *Phil. Trans. R. Soc. Lond. A*, 223:289–343, 1923.

[45] T. Tél and Y.-C. Lai. Chaotic transients in spatially extended systems. *Physics Reports*, 460(6):245 – 275, 2008.

[46] M. van Dyke. *An Album of Fluid Motion*. The Parabolic Press, 1982.

[47] J. Vollmer, T. M. Schneider, and B. Eckhardt. Basin boundary, edge of chaos and edge state in a two-dimensional model. *New Journal of Physics*, 11(1):013040, 2009.

[48] Wikiquote. `http://en.wikiquote.org/wiki/Box,_George_E._P`. Website.

[49] F. H. Willeboordse and K. Kaneko. Pattern dynamics of a coupled map lattice for open flow. *Physica D: Nonlinear Phenomena*, 86(3):428 – 455, 1995.

[50] A. P. Willis and R. R. Kerswell. Critical behavior in the relaminarization of localized turbulence in pipe flow. *Phys. Rev. Lett.*, 98(1):014501, 2007.

[51] A. P. Willis and R. R. Kerswell. Turbulent dynamics of pipe flow captured in a reduced model: puff relaminarization and localized edge states. *Journal of Fluid Mechanics*, 619:213–233, 2009.

Danksagung

Traditionell ist der Abschluss einer großen Arbeit ein guter Zeitpunkt, einigen Leuten zu danken. Mit dieser Tradition will auch ich nicht brechen. Nachdem ich im Vorwort schon den Leuten gedankt habe, die mich wissenschaftlich bei meiner Arbeit unterstützt haben, möchte ich diese Danksagung an die Personen richten, die mir privat viel bedeuten.

Zu aller erst möchte ich hier meinen Eltern, Brigitte und Andreas, danken. Ihr habt mich auf meinem bisherigen Weg immer unterstützt und mir euer Vertrauen gegeben. Danke, dass ihr mir die Werte vermittelt habe, nach denen ich jetzt lebe.

Ebenso danke ich meinem Bruder David. Du bist wahrscheinlich die Person, mit der ich am meisten Zeit verbracht habe. Deine Begeisterung für Musik steht meiner für Physik in nichts nach. Somit zeigst du mir immer wieder aufs Neue, dass es auch andere Seiten im Leben gibt. Danke für die Zeit, die wir bis jetzt zusammen hatten.

Der nächste Dank geht an meine *alten* Schulfreunde. Ohne euch wäre ich mit Sicherheit nicht so geworden, wie ich jetzt bin. Zu nennen sind hier Benedikt und Christian Engelke, Fabian Garbs, Welf Gehrke, Arne Grimsel, Tobias Otto, Urs Vorlop, Anne Wagener und David Westfal. Danke für die schöne Zeit, die jetzt schon sechs Jahre her, aber längst noch nicht vergessen ist.

Außerdem möchte ich mich bei Fabian Garbs, Arne Grimsel, Ruth Hübner, Jana Kassebaum, Robert Schieweck und Constantin Spille für die Begleitung durchs Studium seit der ersten Stunde bedanken. Die Diskussionen über Physik, Mathematik und Philosophie waren immer sehr anregend. Aber am Wichtigsten war für mich, dass der Spaß im Vordergrund stand. Und das hat bei uns immer geklappt!

Nicht weniger wichtig sind natürlich die Leute, die ich erst im Laufe meines Studiums intensiver kennen gelernt habe. Vor allem Julia Bußе, Kathrin Deppe, Steffen Schubert und Constanze Thees. Euch allen wünsche ich auch viel Erfolg für eure Abschlussarbeit oder euren weiteren Berufsweg.

Für die gelungene Ablenkung am Mittwoch Nachmittag möchte ich mich bei meiner Uni-Liga Mannschaft 'TuS Abschuss' bedanken. Das Kicken war immer ein guter Kontrast zur Labor- oder Büroarbeit und hat meinen Kopf frei für neue Erkenntnisse gehalten. Die Zeit mit meinem Lieblingsverein werde ich nie vergessen.

Ein ganz spezieller Dank gilt meinem Physiklehrer Markus Dippel. Ohne seinen interessanten Unterricht und die vielen privaten Gespräche über physikalische Fragen hätte ich wohl nie mit dem Physikstudium begonnen. Ich hoffe, du kannst noch viele weitere Schüler für das spannende Fach Physik begeistern.

Zu guter Letzt möchte ich den wichtigsten Dank an meine Freundin Kathrin Beier

richten. Du trägst den Hauptanteil daran, dass diese Arbeit überhaupt in dieser Form möglich war. Wenn immer ich gestresst oder schlecht gelaunt war, hast du mich wieder aufgebaut und mich ermutigt weiter zu machen. So konnte ich auch die Phasen der Diplomarbeit überstehen, die ergebnislos oder sehr stressig waren. Danke für deine Liebe und dass du mich auch während der anstregenden Phasen ertragen hast.

Eidesstattliche Erklärung

Ich,
Christian Marschler
versichere hiermit, dass ich die vorliegende Diplomarbeit mit dem Titel

A Coupled Map Lattice
Mimicking Turbulent Puffs and Slugs

selbstständig verfasst und keine anderen als die angegebenen Quellen und Hilfsmittel benutzt habe.

Göttingen, den